Institut für Physikalische und Theoretische Chemie,
Lehrstuhl für Theoretische Chemie
der Technischen Universität München

Charge Transport in Single Molecule Junctions: Vibronic Effects and Conductance Switching

Claudia Benesch

Vollständiger Abdruck der von der Fakultät für Chemie der Technischen Universität München zur Erlangung des akademischen Grades eines

Doktors der Naturwissenschaften

genehmigten Dissertation.

Vorsitzender: Univ.-Prof. Dr. M. Groll

Prüfer der Dissertation:

1. Priv.-Doz. Dr. M. Thoss
2. Univ.-Prof. Dr. H. J. Neusser

Die Dissertation wurde am 8. 1. 2008 bei der Technischen Universität München eingereicht und durch die Fakultät für Chemie am 20. 2. 2008 angenommen.

Ich danke

- Meiner Familie für ihren unerschütterlichen Glauben an meine intellektuellen Fähigkeiten.

- Prof. Dr. Wolfgang Domcke dafür, dass er mir die Möglichkeit gegeben hat meine Doktorarbeit an seinem Lehrstuhl zu schreiben und für die kollegiale Art mit der er seine Mitarbeiter führt.

- PD Dr. Michael Thoss für die viele Mühe und Zeit, die er für meine wissenschaftliche Betreuung aufgebracht hat.

- Dr. Martin Čížek für zahlreiche Programme und Daten, die ich im Laufe meiner Arbeit verwenden konnte.

- Prof. Dr. Andrzej Sobolewski für die Anregung mich mit molekularen Schaltern zu beschäftigen.

Contents

Chapter 1

Introduction

'Molecular electronics' is an interdisciplinary field, reaching into chemistry, physics, and electrical engineering, with the ambitious goal to replace or complement silicon semiconductor electronics with devices based on single or few molecules. While there is a natural limit to the progressing miniaturization of semiconductor components (top-down approach), molecules of different size and functionality are synthesized on an atomic level (bottom-up approach). By means of organic synthesis it is possible to tailor molecules in such a way that specific electronic, mechanical, and optical properties are obtained. Based on nano-scale molecular electronic devices it could be possible to build smaller, faster, and cheaper computers. Besides possible practical applications, scientists are naturally interested in the fundamental quantum processes that govern electron transport on the molecular scale.

Historically, the hour of birth of molecular electronics devices was a theoretical paper [1] that appeared in 1974, in which the authors devised a rectifier based on a single organic molecule. This molecule consisted of two electronic π-systems, which played the role of donor and acceptor and were separated by an aliphatic bridge. Since then, a growing number of scientists has investigated the conductance properties of molecules using various theoretical techniques [2]. The first experimental single molecule junction was realized in 1997 [3].

From a chemist's point of view, 'molecular conductance' can be considered as the continuation of concepts well known from theoretical and experimental studies of charge transfer in donor-bridge-acceptor systems [4]. The major difference is the fact that in molecular junctions donor and acceptor states are no longer localized on some part of the molecule, but delocalized in metal electrodes, while the actual molecule forms the bridge. Therefore, in the context of molecular conductance, the term charge transport rather than charge transfer is used.

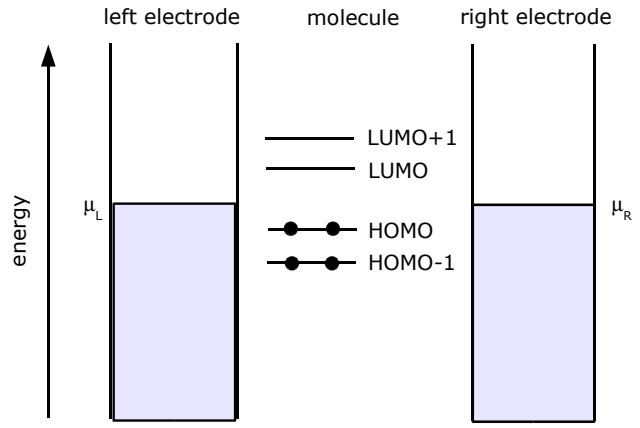

Figure 1.1: Energy level scheme of a molecular junction at equilibrium.

To discuss the basic mechanism of charge transport through single molecules, Fig. 1.1 shows the energy level scheme of a molecular junction. The left and right metal electrodes are characterized by their chemical potentials, μ_L and μ_R, and their Fermi distributions. The electrodes are chemically bound to a molecule, which is described by discrete electronic states that couple to the continuum of electronic states in the metallic electrodes. If no bias voltage is applied to the junction, the two electrodes are in equilibrium and their chemical potentials are equal to each other and to the Fermi energy ϵ_f. In this situation, the occupied molecular levels are located below the Fermi level, whereas the unoccupied molecular states are located above. Fig. 1.1 shows the situation at temperature T=0 K, where the Fermi distribution corresponds to a step function.

If a (direct) voltage U is applied, the chemical potentials of the electrodes are shifted to $\mu_L = \epsilon_f - eU/2$ and $\mu_R = \epsilon_f + eU/2$, where e is the electron charge ($1.6 \cdot 10^{-19}$ C), and where we assumed that the voltage drops symmetrically at both molecule-electrode interfaces. In principal, also the molecular states will be shifted by the applied bias voltage (Stark effect) and they could be manipulated by an additional gate electrode.

At low voltages, carrier transport is possible only through direct tunneling between left and right electrode. Because of its low current, this region is referred to as the conductance gap. Resonant carrier transport starts as soon as the chemical potential of one electrode equals the energy of the highest occupied molecular orbital (HOMO) (Fig. 1.2 left) or the lowest unoccupied molecular orbital (LUMO) (Fig. 1.2 right). While in the first case a hole tunnels from the left electrode via the HOMO of the molecule to the right electrode, in the second case an electron tunnels from the right electrode via

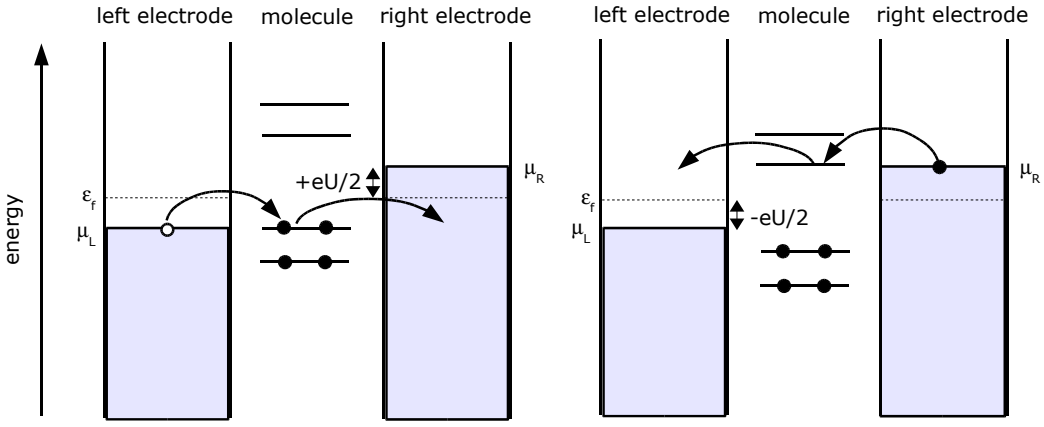

Figure 1.2: Energy level scheme of a molecular junction under finite bias. In the left panel the situation corresponding to hole transport through the HOMO is depicted, while the right panel shows the situation corresponding to electron transport through the LUMO.

the LUMO to the left electrode.

The main focus of this thesis is on the investigation of the influence of the vibrational (nuclear) degrees of freedom of the molecule on the conductance properties of the junction. The mechanism of electronic transitions that are accompanied by a change of the vibrational state of the molecule is illustrated in Fig. 1.3. The left panel in Fig. 1.3 shows a situation, where the chemical potential of the left electrode is larger than the energy of the vibrational ground state. In this case an electron on the molecule can tunnel into the left electrode (black arrow) only by absorption of vibrational quanta (red arrow). This process is called vibrationally induced transport and can take place only if the molecule is in a vibrationally excited state. The right panel in Fig. 1.3 describes a situation, where the chemical potential of the left electrode is smaller than the energy of the vibrational ground state. In this case an electron can tunnel from the HOMO by releasing its excess energy into vibrational motion.

Vibronic effects in single molecule conductance have been of great interest recently. The current-induced excitation of the vibrations of the molecule may result in heating of the molecular bridge and could lead to breaking of the junction, if too much energy is deposited in the vibration of a bond that is important for the junction's stability. Conformational changes of the geometry of the conducting molecule are possible mechanisms for negative differential resistance (NDR) and switching behavior, properties which are both of technological interest. Furthermore, the observation of vibrational

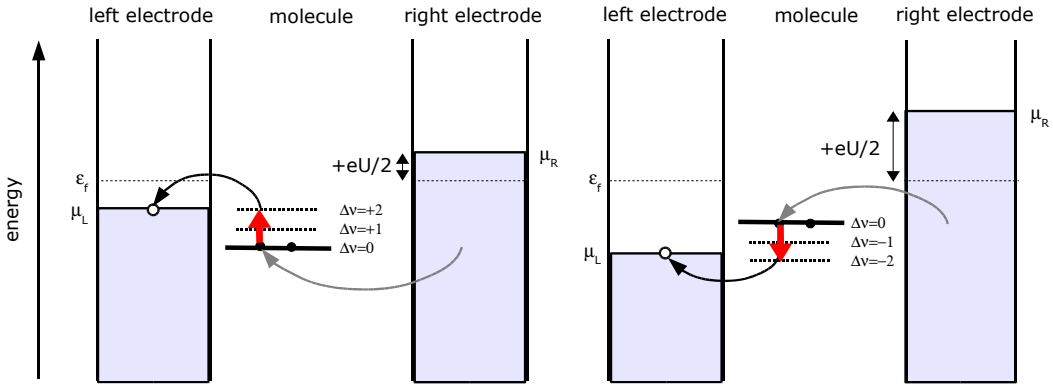

Figure 1.3: Energy level scheme of a molecular junction under finite bias. Transport occurs through the HOMO, which is allowed to interact with vibrations. The bold line indicates the position of the vibrational ground state of the molecule. In the left panel, an electron on the HOMO needs to absorb the energy of two vibrational quanta (red arrow, $\Delta\nu = +2$) before tunneling into the left electrode (black arrow). In the right panel, an electron on the HOMO excites two vibrational quanta (red arrow, $\Delta\nu = -2$) before tunneling into the right electrode (black arrow). The holes on the molecule are refilled by electrons from the right electrode (gray arrows).

structures in conduction measurements allows the unambiguous identification of the molecular character of the current.

This thesis is organized in the following way: Chapter 2 gives a short review of experimental and theoretical methods employed in the investigation of molecular junctions. In Chapter 3, we outline the Hamiltonian of a molecular junction and describe the methodology used to determine the parameters including quantum chemical methods and a projection procedure. Chapter 4 presents general aspects of the description of electron and hole transport through metal-molecule-metal (MMM)-junctions based on scattering theory. Furthermore, results for various model systems will be discussed. In Chapter 5, electron and hole transport in molecular junctions will be described within density matrix theory. Results based on density matrix calculations will be compared to those obtained by scattering theory calculations. An example of a molecular switch is presented in Chapter 6. Finally, Chapter 7 concludes with a summary of the thesis.

Chapter 2

A Survey of Experimental and Theoretical Techniques

2.1 Experimental Methods

There are various techniques which allow to measure the charge flow through a single or a small number of molecules [5]. The molecular systems, which have been studied in recent years, range from small metallic chains to inorganic molecules like H_2 or CO, from organic molecules like benzenedithiol to carbon nanotubes or fullerenes, and to biochemical molecules like DNA. In small metallic chains the conductance could be shown experimentally [6] to be quantized, with the quantum unit of conductance being

$$g_0 = 2\,e^2/h = (12.9\,k\Omega)^{-1}\ , \tag{2.1}$$

as was predicted theoretically [7], where h is Planck's constant ($6.6{\cdot}10^{-34}$ J·s). A conductance of g_0 constitutes an upper limit for conductance that is usually not reached by single molecule junctions.

The experimental method, which is most closely related to the molecular junctions simulated in this work is the 'mechanically controllable break-junction technique' [8]. In this technique a notched wire is glued to a piezoelectrically controlled bendable substrate. By bending, this wire is broken and gaps with widths of a few nanometers are formed, on which a droplet of a solution containing the molecule of interest is applied or which is exposed to gas. The solution is highly diluted in order to prevent clustering. As without molecules conductance quantization could be observed, the electrodes are assumed to be atomically sharp tips. The junction can be repeatedly opened and closed until only a single molecule is bound to the electrodes. One of the advantages of this technique is that it can be used at atmospheric

pressure, while the lack of knowledge about the atomic configuration of the molecule-electrode contact constitutes a disadvantage.

The break-junction method was used in the measurement of H_2, HD, and D_2 between platinum electrodes [9], where abrupt changes in conductance were assigned to switching between two slightly different local geometrical configurations, induced by the transverse motion of the molecule. Observing the shift in the frequencies on stretching of the platinum contact, the molecular modes could be classified as longitudinal or transversal [10]. The conductance of H_2 is slightly below g_0 ($\sim 0.9\, g_0$) and was theoretically demonstrated to be due to a strong hybridization of the anti-bonding state of H_2 with d- and s-like orbitals of the adjacent platinum atoms [11].

An early break-junction experiment was conducted by Reed and coworkers [12] using benzenedithiol as the molecule under study. Later it was criticized that probably not a single but several molecules were measured, an argument that is supported by the fact that, up to now, the results of this measurement, especially at larger voltages ($\sim$5 V), have not been reproduced. Nevertheless, this experiment was the first of its kind and constitutes a breakthrough in the realization of molecular junctions.

Other experiments [13] on more complex organic molecules demonstrated that unsymmetric molecules may lead to unsymmetric current-voltage characteristics, demonstrating the realization of molecular rectifiers. It was also shown that different I-V characteristics can be obtained using one and the same junction, because of fluctuating metal-molecule contact-geometries.

Another important technique to investigate conductance in molecular junctions is inelastic electron tunneling spectroscopy (IETS), an experiment that is conducted in a scanning tunneling microscope (STM). STM has the advantage that the molecular geometry can be determined on an atomic level, but has the drawback that measurements can be done in high vacuum only. In a STM the molecule is contacted on one side by the surface on which it adsorbs and on the other side by the STM-tip. It is obvious that with this assembly the MMM-junction is unsymmetric regardless of the symmetry of the molecule. In IETS, features of vibrational motion are mostly observed in the electronic off-resonant regime.

Using this technique, the influence of vibrations on the molecular conductance of copper phtalocyanin was investigated [14]. It was found that vibrational features can be observed, if the coupling of the molecular adsorbate to the metal surface is comparatively small. The vibrational motion observed in this experiment was associated with the deformation of the phtalocyanin ring and the out-of-plane motion of the indole-units.

In another STM experiment [15] up to 4 progressions of a vibronic (vibra-

tional-electronic) transition were seen. Furthermore, the dependence of the vibronic coupling on the spatial position of the STM-tip was demonstrated.

The conductance of a single molecule can also be measured if this molecule is embedded in a self-assembled monolayer of insulating molecules, which do not interact with the molecule under investigation [16].

A related technique is conducting atomic force microscopy, which usually has a lower spatial resolution than STM, but allows the study of electromechanical properties of the molecular junction. Using this technique it was found, that molecular junctions, in which the molecule is bound to the gold substrate via thiol groups, break in the Au-Au bond [17] and not inside the molecule, when pulling the tip away from the surface.

Another realization of molecular junctions can be achieved by growing a thin gold wire on a SiO_2-layer using electron-beam lithography. The wire is coated with the molecules under investigation and is broken by electromigration until a gap of a length of a few nm results [18]. Disadvantages of this method are the facts that the contact geometry and the actual number of molecules between the electrodes is unknown, as well as the relatively low fabrication yield. In order to increase the probability with which single-molecule devices are fabricated, a method was developed that is based on synthesizing a dimer structure consisting of two colloidal gold particles connected by a dithiolated short organic molecule and electrostatically trapping it between two metal electrodes [19].

Using electron-beam lithography it is also possible to add a gate electrode and build molecular transistors [20, 18, 21]. The majority of experimental work, however, did not employ these electronically relevant three-terminal devices but two-terminal devices, which are easier to fabricate.

Still a great challenge is the simultaneous investigation of the electronic and optical properties of molecular junctions. When irradiating molecular junctions with light in the visible spectrum, the electronic properties may be altered by a light-induced conformational change of the molecule. On the other hand, light emission could be stimulated by the electronic current [22]. A slightly different realization of this idea is described in Ref. [23], where an electron is photo-excited in the STM-tip with green laser light and subsequently transferred onto the unoccupied orbitals of the molecule.

2.2 Theoretical Methods

The theoretical methods to describe quantum transport through a MMM-junction in the presence of vibronic coupling can be classified into three

groups: scattering theory, density matrix approaches, and methods based on many-body techniques [24]. As scattering theory and density matrix methods will be discussed in detail in the respective chapters of this thesis, this section is intended to give an overview of the third group of theoretical methods, among which the non-equilibrium Green's function (NEGF) transport formalism is most important.

The non-equilibrium stationary current is defined by the temporal change of the charge in the left or right electrode in the steady state limit,

$$I = e \lim_{t\to\infty} \frac{d}{dt}\langle \hat{N}_{L/R}(t)\rangle, \quad \hat{N}_{L/R}(t) = 2 \sum_{k\in L/R} c_k^\dagger(t) c_k(t) \ . \tag{2.2}$$

Here $\langle \hat{N}(t)\rangle$ is the expectation value of the number operator, $c_k^\dagger$ (c_k) are electron creation (annihilation) operators, and the factor 2 accounts for spin degeneracy.

In the non-equilibrium (or Keldysh-) Green's function formalism [25], the current (Eq. (2.2)) is expressed in the form

$$I = \frac{2\,e}{h} \int \mathrm{d}E \ \mathrm{tr}\left\{\Sigma^< G^> - \Sigma^> G^<\right\} \ ,$$

where $\Sigma^<$ and $\Sigma^>$ denote the lesser and greater self-energies, and $G^<$ and $G^>$ are the lesser and greater Green's functions, respectively, which are all functions of energy and voltage. The matrix elements of these Green's functions are given by the following Fourier transforms of electron correlation functions,

$$\begin{aligned} G^<_{ij}(E) &= -\ \frac{i}{\hbar}\int \mathrm{d}(t-t') e^{-iE(t-t')/\hbar} \langle c_j^\dagger(t') c_i(t)\rangle \ , \\ G^>_{ij}(E) &= \ \ \frac{i}{\hbar}\int \mathrm{d}(t-t') e^{-iE(t-t')/\hbar} \langle c_i(t) c_j^\dagger(t')\rangle \ , \end{aligned}$$

where in the steady-state limit the integrand only depends on the time-difference $t-t'$. The correlation function $\langle c_j^\dagger(t') c_i(t)\rangle$ describes events where first an electron is annihilated in molecular state i at time t and then another electron is created in molecular state j at time t', while the function $\langle c_i(t) c_j^\dagger(t')\rangle$ describes a situation where first an electron is created in state j at time t' and then another electron is annihilated in state i at time t. Thus, the Green's functions $G^<$ and $G^>$ describe particles or holes that enter and leave the molecule.

The lesser and greater Green's functions and self-energies are related to each other via a kinetic (Keldysh) equation,

$$G^< = G^R \Sigma^< G^A \quad \text{and} \quad G^> = G^R \Sigma^> G^A \ ,$$

where G^A and G^R are the advanced and retarded Green's functions, respectively. In contrast to the lesser and greater Green's functions, G^R describes the dynamics of the particles on the molecule and is given by

$$G^R = \left[E^+ - H - \Sigma^R\right]^{-1} = \lim_{\eta \to 0^+} \left[(E + i\eta)\mathbf{1} - H_M - \Sigma^R\right]^{-1} \ ,$$

where $\mathbf{1}$ is the unit operator, H_M is the Hamiltonian of the molecule, Σ^R is the retarded self-energy, and $G^A = (G^R)^\dagger$.

The lesser/greater and retarded/advanced self-energies may include components due to the interactions of the molecule with the electrodes, due to electron-electron interactions on the molecule, and due to vibronic interactions on the molecule. It is the complexity of the latter two interactions, which restricts the NEGF method to small approximate models. For example, vibronic coupling has so far only been treated in the Born-approximation or the self-consistent Born approximation (SCBA). In the self-consistent approach, the self-energies themselves depend on the lesser/greater Green's function and a self-consisted cycle has to be solved until convergence is reached.

Despite these limitations, the NEGF formalism is attractive because it describes the non-equilibrium dynamics of the electronic and vibrational system simultaneously.

In the absence of electron-electron and vibronic interactions both the NEGF and the scattering formalism (discussed in Chapter 4) yield the same expression for the current,

$$I = \frac{2\,e}{h} \int \mathrm{d}E \, \mathrm{tr}\left\{\Gamma_L G^A \Gamma_R G^R\right\} \, \left[f_L(E) - f_R(E)\right] \ , \tag{2.3}$$

where Γ_L and Γ_R give the coupling strength between molecule and left or right electrode, respectively. In Eq. (2.3) the current is expressed in terms of the transmission function [7] $T(E) = \mathrm{tr}\left\{\Gamma_L G^A \Gamma_R G^R\right\}$.

The NEGF transport formalism has been used by numerous groups to study the influence of vibrational motion in molecular junctions. In Ref. [26] the current as well as the power loss and heat production in a molecular junction were investigated. Thereby, the molecule was described by a generic model comprising a single or two electronic states coupled to a single mode. The authors also studied the lineshape and linewidth of vibrational features in inelastic electron tunneling spectroscopy, where peaks occur in the low-voltage region if the voltage is in resonance with a vibrational transition in the molecule. They found, that the coupling of conducting electrons of the electrodes to nuclear motion of the molecular bridge contributes substantially to the features in the IETS curve.

The same authors developed an approximate, self-consistent procedure for transport in the resonant regime in the case where vibronic coupling is large compared to the electronic coupling between molecule and electrodes[27]. In this approach the Green's functions are derived in second order of the electrode-molecule coupling.

The NEGF-SCBA formalism was also used to investigate the incoherent component of the off-resonant tunneling current and the power dissipated on the molecule for octanedithiol clamped between two gold clusters [28]. The parameters in this study were taken from a DFT parameterized tight-binding (DFTB) calculation and it was found, that C-C stretch modes give the largest contribution to both current and power dissipation. Using NEGF also the IETS spectrum of the fullerene C_{20} [29] and the I-V characteristics of benzenedithiol [30] were calculated.

The IETS-spectra for three different organic compounds were computed using the NEGF formalism in the lowest order expansion in the vibronic coupling [31]. These spectra agreed very well in peak position and peak width with experimental data [32], but overestimated the peak height. The same authors extended their approach to include the SCBA [33], which, except for the linewidth, described experimental data of gold atmoic wires very well. For these systems results based on the lowest order expansion and the SCBA were in good agreement. They also observed that vibronic coupling seems to lower the IETS-signal for high-conductance systems such as gold wires, while it seems to increase the signal for low-conductance systems like organic molecules.

Other techniques to describe inelastic quantum transport at the molecular scale include path-integral methods (e.g. Ref. [34]) and numerical renormalization group methods (e.g. Ref. [35]). The path integral method is a non-perturbative approach that is capable of describing the transient as well as the steady-state regime, but it is computationally demanding. The numerical renormalization group method was used to describe transport in the linear response regime including electron-electron and electron-vibrational interactions.

Chapter 3

Modelling of Molecular Junctions

In this chapter we will derive and discuss the Hamiltonian that is used to describe a MMM-junction. To this end, the MMM-junction is partitioned into several parts, which will be treated by different quantum chemistry methods. We will describe how we employ density functional theory (DFT) to derive the parameters of the Hamiltonian.

3.1 Hamiltonian of the Molecular Junction

The Hamiltonian of an MMM-junction is given by the general expression,

$$H = T_n + V_{nn} + H_e(\mathbf{R}) \ . \tag{3.1}$$

Here, T_n denotes the kinetic energy of the nuclei,

$$T_n = \sum_a \frac{\mathbf{p}_a^2}{2M_a} \ ,$$

where $\mathbf{p}_a$ is the momentum and M_a is the mass of nucleus a. The nuclear repulsion energy is given by,

$$V_{nn} = \sum_{a \neq b} \frac{Z_a Z_b e^2}{|\mathbf{R}_a - \mathbf{R}_b|} \ ,$$

where Z_a is the atomic number and $\mathbf{R}_a$ denotes the Cartesian coordinates of the position of nucleus a. The electronic Hamiltonian, H_e, depends on the nuclear coordinates $\mathbf{R}$ via the nuclei-electron Coulomb attraction.

If no bias voltage is applied, the junction is in its electronic ground state. Employing an effective one particle description, the ground state is given by a single Slater determinant, $|\Psi_g\rangle = \prod_{i=1}^{n_g} c_i^\dagger |0\rangle$, where the operator $c_i^\dagger$ creates an electron in the single particle state (molecular orbital) labeled by i, the product is taken over all electrons in the neutral junction, $|0\rangle$ denotes the vacuum state, and n_g is the number of electrons in the ground state. The electron operators were not labeled by their spin projections, as spin will not be treated explicitly in this work. $|\Psi_g\rangle$ is an approximate solution of the electronic Schrödinger equation,

$$H_e(\mathbf{R})|\Psi_g\rangle = E_g(\mathbf{R})|\Psi_g\rangle$$

with eigenenergy $E_g(\mathbf{R})$, which parametrically depends on the nuclear coordinates. The energy $E_g(\mathbf{R}) + V_{nn}$ represents the adiabatic potential energy surface of the electronic ground state, which will serve as a reference state in the following.

If an external voltage is applied to the MMM-junction, electrons (or holes) are transferred to/from the junction and the electron number, n_g, will change. Within Koopmans' theorem the energy of a cation is given by subtracting the energies of the ionized single particle states from the energy of the neutral ground state. The energy of an anion, on the other hand, is given by adding the energies of the single particle states, that became occupied, to the energy of the neutral ground state. An electronic Hamiltonian that can describe both situations is given by [36],

$$H_e(\mathbf{R}) = E_g(\mathbf{R}) - \sum_{i\in\text{occ.}} E_i(\mathbf{R}) c_i c_i^\dagger + \sum_{j\in\text{unocc.}} E_j(\mathbf{R}) c_j^\dagger c_j \ , \tag{3.2}$$

where the index i labels all orbitals that are occupied in the neutral reference state, while the index j labels all orbitals that are unoccupied in the neutral reference state, and the operator c_i annihilates electrons in the single particle state i. If the electronic spectrum of a molecular junction is such, that the levels, which contribute to conduction, are all located far below or far above the Fermi energy, the third or second term in Eq. (3.2) can be neglected, respectively. In the latter case the current is dominated by electron transport (e. t.), while in the former case hole transport (h. t.) prevails. The electronic Hamiltonian thus reduces to

$$H_e(\mathbf{R}) = E_g(\mathbf{R}) + \sum_{j\in\text{unocc.}} E_j(\mathbf{R}) c_j^\dagger c_j \qquad \text{(e. t.)} \ , \tag{3.3a}$$

$$H_e(\mathbf{R}) = E_g(\mathbf{R}) - \sum_{j\in\text{occ.}} E_j(\mathbf{R}) c_j c_j^\dagger \qquad \text{(h. t.)} \ . \tag{3.3b}$$

As will be discussed in more detail in the next section, the second term in Eqs. (3.3) will be split into three terms, describing the molecule, the left and right electrode, and the electronic coupling between molecule and electrodes,

$$
\begin{aligned}
H_e(\mathbf{R}) &= E_g(\mathbf{R}) + \sum_{j\in M} E_j(\mathbf{R}) c_j^\dagger c_j + \sum_{k\in L,R} E_k c_k^\dagger c_k + V \quad \text{(e. t.)}, \quad (3.4a)\\
H_e(\mathbf{R}) &= E_g(\mathbf{R}) - \sum_{j\in M} E_j(\mathbf{R}) c_j c_j^\dagger - \sum_{k\in L,R} E_k c_k c_k^\dagger + V \quad \text{(h. t.)}, \quad (3.4b)\\
V &= \sum_{j\in M}\sum_{k\in L,R} \left(V_{jk} c_j^\dagger c_k + h.c. \right) \ .
\end{aligned}
$$

Here, the indices j and k denote electrons that now are either localized on the molecule, or on the left or right electrode. In Eqs. (3.4) it was assumed, that the left and right electrode spaces do not interact with each other, and neither the energies of the electrode states nor the coupling elements between electrodes and molecular states depend on the nuclear coordinates.

In the applications considered below, the potential energy of the nuclei, $V_{nn} + E_g(\mathbf{R})$, will be expanded up to second order in the nuclear coordinates around the equilibrium geometry ($\mathbf{R}_{eq}$) of the neutral molecule. Including, furthermore, the kinetic energy of the nuclei gives the nuclear Hamiltonian,

$$
H_{n0} = T_n + V_{nn} + E_g(\mathbf{R}) = \sum_l \hbar\omega_l \left(a_l^\dagger a_l + \frac{1}{2} \right) \tag{3.5}
$$

where ω_l is the frequency of the dimensionless vibrational normal mode q_l, and $a_l^\dagger / a_l$ are the harmonic oscillator creation/destruction operators.

Expanding the molecular orbital energies $E_j(\mathbf{R})$ to first order in the nuclear coordinates around the equilibrium geometry ($\mathbf{R}_{eq}$) of the neutral molecule gives the vibronic coupling term,

$$
H_{ne} = \sum_{l,j\in M} \frac{\kappa_l^{(j)}}{\sqrt{2}} \left(a_l + a_l^\dagger \right) c_j^\dagger c_j \quad \text{(e. t.)} \ , \tag{3.6}
$$

$$
H_{ne} = \sum_{l,j\in M} \frac{\kappa_l^{(j)}}{\sqrt{2}} \left(a_l + a_l^\dagger \right) c_j c_j^\dagger \quad \text{(h. t.)} \ . \tag{3.7}
$$

Here, the vibronic coupling parameter $\kappa_l^{(j)} = \left(\frac{\partial E_j}{\partial q_l} \right)_{\mathbf{R}_{eq}}$ was introduced and the dimensionless normal mode coordinate was expressed in terms of creation and annihilation operators, $q_l = \frac{1}{\sqrt{2}}(a_l^\dagger + a_l)$. The overall Hamiltonian is thus

given by

$$H = \sum_l \hbar\omega_l \left(a_l^\dagger a_l + \frac{1}{2} \right) + \sum_{l,j\in M} \frac{\kappa_l^{(j)}}{\sqrt{2}} \left(a_l + a_l^\dagger \right) c_j^\dagger c_j + \sum_{j\in M} E_j c_j^\dagger c_j + \sum_{k\in L,R} E_k c_k^\dagger c_k + \sum_{j\in M} \sum_{k\in L,R} \left(V_{jk} c_j^\dagger c_k + h.c. \right) \quad \text{(e. t.)} \,, \tag{3.8a}$$

$$H = \sum_l \hbar\omega_l \left(a_l^\dagger a_l + \frac{1}{2} \right) - \sum_{l,j\in M} \frac{\kappa_l^{(j)}}{\sqrt{2}} \left(a_l + a_l^\dagger \right) c_j c_j^\dagger - \sum_{j\in M} E_j c_j c_j^\dagger - \sum_{k\in L,R} E_k c_k c_k^\dagger + \sum_{j\in M} \sum_{k\in L,R} \left(V_{jk} c_j^\dagger c_k + h.c. \right) \quad \text{(h. t.)} \,. \tag{3.8b}$$

The linear form of the vibronic coupling implies that only normal modes belonging to the totally symmetric representation of the respective symmetry group have a non-vanishing coupling constant. The harmonic approximation of the nuclear potential will be valid for small amplitude motion.

For the calculations employing scattering theory (Chapter 4) it is expedient to represent the Hamiltonian in terms of single particle states. In the case of electron transport the single particle states are defined as $|\phi_j\rangle = c_j^\dagger |\Psi_g\rangle$, while in the case of hole transport they are given by $|\phi_j\rangle = c_j |\Psi_g\rangle$. Here, $|\phi_j\rangle$ denotes orthogonal single particle states (molecular orbitals) representing the molecular bridge. The single-particle Hamiltonian is obtained from the many-particle Hamiltonian in Eqs. (3.8) by a projection onto the single-particle states,

$$H \to \sum_{i,i'} |\phi_i\rangle\langle\phi_i| H |\phi_{i'}\rangle\langle\phi_{i'}| \,.$$

We thus obtain

$$H = H_{n0} + H_M + H_{ne} + H_L + H_R + V \quad \text{(e. t.)} \,, \tag{3.9a}$$

$$H = H_{n0} - H_M - H_{ne} - H_L - H_R - V \quad \text{(h. t.)} \,, \tag{3.9b}$$

with

$$H_{n0} = \sum_l \hbar\omega_l \left(a_l^\dagger a_l + \frac{1}{2} \right) \,,$$

$$H_M = \sum_{j\in M} E_j |\phi_j\rangle\langle\phi_j| \,,$$

$$H_{ne} = \sum_{l,j\in M} \frac{\kappa_l^{(j)}}{\sqrt{2}} \left(a_l + a_l^\dagger \right) |\phi_j\rangle\langle\phi_j| \,,$$

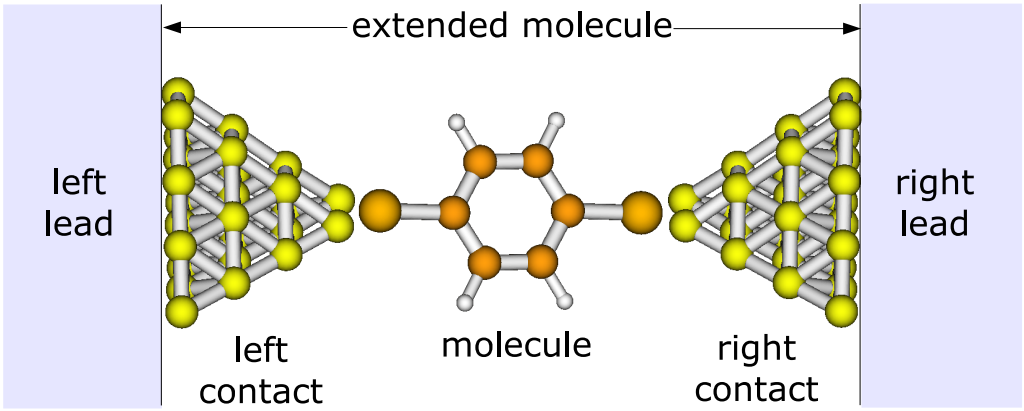

Figure 3.1: The scheme of a molecular junction, consisting of left and right leads, left and right contacts, and the molecule. Left and right contacts and the molecule form the extended molecule. Contact and lead form the electrode.

$$
\begin{aligned}
H_L + H_R &= \sum_{k\in L,R} E_k |\phi_k\rangle\langle\phi_k| \ , \\
V &= \sum_{j\in M}\sum_{k\in L,R} (V_{jk}|\phi_j\rangle\langle\phi_k| + h.c.) \ \text{(e. t.)} \ , \\
V &= \sum_{j\in M}\sum_{k\in L,R} (V_{kj}|\phi_j\rangle\langle\phi_k| + h.c.) \ \text{(h. t.)} \ .
\end{aligned}
$$

3.2 Partitioning of the Molecular Junction

The Hamiltonian introduced in the last section contains several parameters, energies, electronic and vibronic coupling elements, that have to be determined by quantum chemistry methods. To this end ab initio methods like Hartree Fock (HF) and Density Functional Theory (DFT) or semi-empirical methods like extended Hückel (also called tight-binding) may be employed.

When using quantum chemistry methods, we are confronted with the problem that an MMM-junction constitutes a non-periodic, open system of infinite dimension. Thereby, conventional quantum chemistry methods that either compute small finite or periodic infinite systems cannot be used straightforwardly.

We circumvent this problem by partitioning the junction into a finite part that is treated explicitly, and an infinite, periodic part, that is treated implicitly by self-energies, i.e. by the effect it has on the finite part. The

separation scheme is illustrated in Fig. 3.1. The finite part, referred to as the 'extended molecule', comprises the actual molecule and parts of the metal electrodes. The parts of the metal electrodes which are included in the extended molecule are in the following referred to as the 'contacts'. A quantum chemical calculation will be performed for this extended molecule. This ensures that changes in the molecular geometry as well as in the molecular electronic structure due to bond formation with the electrodes are included explicitly.

Thus, the molecular junctions are subdivided into five parts. The molecular part, the part of the left and right electrode, that is explicitly included in the quantum chemistry calculation, and the part of the left and right electrodes that is not treated explicitly in the ab initio calculation, referred to as the left and right leads and modelled by semi-infinite solids.

The quantum chemistry calculation of the extended molecule provides us with a single particle Hamiltonian matrix, h, and the overlap matrix, S, both given in the space of atomic non-orthogonal orbitals $\{|\chi\rangle\}$,

$$h_{ij} = \langle\chi_i|h|\chi_j\rangle, \qquad\qquad S_{ij} = \langle\chi_i|\chi_j\rangle \ .$$

In order to divide the overall Hilbert-space into three mutually orthogonal subspaces describing the molecular and the two contact parts of the model system, the following projection procedure was employed (a similar separation scheme as above was employed in the study of electron transfer dynamics in dye-semiconductor systems [37]): The atomic orbital basis was orthogonalized using a Löwdin orthogonalization procedure [38], which among all the possible orthonormal functions yields those closest, in the least-squares sense, to the original non-orthogonal ones. The new orbitals, $\{|\tilde{\chi}\rangle\}$, may no longer be localized on single atoms only, which constitutes a disadvantage of the Löwdin procedure and may lead to errors for orbitals that are located close to the partition boundary. As compared to the widely used Gram-Schmidt orthogonalization scheme, the scheme of Löwdin has the advantage of being unbiased, i.e. the basis functions do not have to be ordered in some arbitrary way, but are all treated simultaneously. To this end, S was diagonalized to calculate its inverse square root and the Hamiltonian was transformed to this new basis,

$$A^T S A = s \qquad S^{-\frac{1}{2}} = A s^{-\frac{1}{2}} A^T \qquad \tilde{h} = S^{-\frac{1}{2}} h S^{-\frac{1}{2}} \ .$$

Here,

$$\tilde{h}_{ij} = \langle\tilde{\chi}_i|h|\tilde{\chi}_j\rangle, \qquad\qquad .$$

The basis states $|\tilde{\chi}\rangle$ are arranged in a way that elements of the Hamiltonian

matrix $\tilde{h}$ belonging only to L, M, or R form blocks on the diagonal,

$$\tilde{h} = \begin{pmatrix} \tilde{h}_L & \tilde{h}_{LM} & \tilde{h}_{LR} \\ \tilde{h}_{ML} & \tilde{h}_M & \tilde{h}_{MR} \\ \tilde{h}_{RL} & \tilde{h}_{RM} & \tilde{h}_R \end{pmatrix} . \tag{3.10}$$

At this stage we add a surface self-energy (Σ^{sf}) to the Hamiltonian matrix elements belonging to the gold atoms of the outermost layer of the contacts in order to describe the effect of infinite leads (cf. App. A),

$$h^{\mathrm{sf}} = \tilde{h} + \Sigma^{\mathrm{sf}} . \tag{3.11}$$

This surface self-energy can, for example, be modelled by a single parameter or by a tight binding model of a semi-infinite solid (cf. Sec. 4.3).

In the next step h^{sf},

$$h^{\mathrm{sf}} = \begin{pmatrix} h^{\mathrm{sf}}_L & h^{\mathrm{sf}}_{LM} & h^{\mathrm{sf}}_{LR} \\ h^{\mathrm{sf}}_{ML} & h^{\mathrm{sf}}_M & h^{\mathrm{sf}}_{MR} \\ h^{\mathrm{sf}}_{RL} & h^{\mathrm{sf}}_{RM} & h^{\mathrm{sf}}_R \end{pmatrix} ,$$

will be transformed by a matrix that diagonalizes the submatrices h^{sf}_L, h^{sf}_M, and h^{sf}_R, yielding the block-diagonalized matrix h^{u}:

$$h^{\mathrm{u}} = U^T h^{\mathrm{sf}} U = \begin{pmatrix} E^L & V^{LM} & V^{LR} \\ V^{ML} & E^M & V^{MR} \\ V^{RL} & V^{RM} & E^R \end{pmatrix} , \; U = \begin{pmatrix} U_L & 0 & 0 \\ 0 & U_M & 0 \\ 0 & 0 & U_R \end{pmatrix} . \tag{3.12}$$

The diagonal submatrices E^L and E^R contain the contact energies E_k, the diagonal submatrix E^M contains the eigenenergies of the molecular bridge, E_j, and the submatrices V denote the electronic coupling between states localized on the contact and on the molecule. We note, that while the eigenvectors that directly diagonalize h constitute the adiabatic states of the total electronic system, the eigenvectors of h^{sf}_L, h^{sf}_M, and h^{sf}_R can be considered as quasi-diabatic states and the whole block-diagonalization corresponds to a diabatization procedure [39].

As the surface self-energy, Σ^{sf}, is, in general, not Hermitian, the Hamiltonian matrix, h^{sf}, is complex symmetric. This has the consequence that after block-diagonalization the eigenstates in the left and right contact spaces form a bi-orthogonal basis (cf. App. A).

3.3 Density Functional Theory

In this work the electronic structure of the extended molecule will be computed using density functional theory. In DFT (cf. the corresponding chapters in Refs. [40, 41]) the central quantity is the electron density ρ of the

electronic ground state, which is a function of three spatial coordinates (neglecting spin). This is in contrast to other computational chemistry methods, in which the central quantity is the electronic wave function, which depends on 3·n spatial coordinates, where n denotes the number of electrons.

As was proven by Hohenberg and Kohn, the electron density uniquely determines the energy of the non-degenerate electronic ground state via the functional $E[\rho]$, which is a sum of functionals describing the kinetic energy, the electron-nuclei attraction, and the electron-electron repulsion. The latter is split into the Coulomb and the exchange part. The functionals describing electron-nuclei attraction, $E_{ne}[\rho]$, and the Coulomb functional, $J[\rho]$, are given by,

$$\begin{aligned} E_{ne}[\rho] &= \sum_a \int \mathrm{d}\mathbf{r} \frac{Z_a \rho(\mathbf{r})}{|\mathbf{R} - \mathbf{r}|} \ , \\ J[\rho] &= \frac{1}{2} \int \int \mathrm{d}\mathbf{r} \mathrm{d}\mathbf{r}' \frac{\rho(\mathbf{r})\rho(\mathbf{r}')}{|\mathbf{r}' - \mathbf{r}|} \ . \end{aligned}$$

In Kohn-Sham theory the exact kinetic energy functional for non-interacting electrons is given by

$$T = \sum_i \langle \tilde{\phi}_i | -\frac{1}{2} \nabla^2 | \tilde{\phi}_i \rangle \ ,$$

where the Kohn-Sham orbitals $|\tilde{\phi}_i\rangle$ are the components of a Slater determinant. The difference in kinetic energy between interacting and non-interacting electrons and the exchange term form an exchange-correlation functional, which again is split into an exchange and a correlation part. There exist different approximations to these exchange and correlation functionals.

Similar to HF, the set of Kohn-Sham orbitals are computed in a way that minimizes the total energy, which, because of the density dependence of the Coulomb and exchange-correlation term, leads to a self-consistent procedure. When expanding the Kohn-Sham orbitals in a non-orthogonal basis set, the Kohn-Sham equations have the form: $h_{KS}C = SC\varepsilon$, where h_{KS} is the Kohn-Sham matrix, C is the matrix of the expansion coefficients, S is the overlap matrix, and the vector ε contains the eigenvalues of the Kohn-Sham orbitals.

When working with Kohn-Sham orbitals, as will be done in all of the following calculations, it should be noted that they are the orbitals of a fictitious reference system of non-interacting electrons with the same electron density and therefore, strictly speaking, have no physical reality. However, when considering this a drawback as compared to Hartree-Fock theory one should note, that the molecular orbitals in HF belong to a reference system of electrons, which experience only the average field of the other electrons

(mean field theory). This is also only an approximation to the true electronic interactions in a molecule. Unlike Hartree-Fock theory, DFT with an approximate exchange-correlation functional is not variational and can yield molecular energies below the true ground state energy.

Using DFT or Hartree-Fock theory to describe the extended molecule usually implies that only a single electron configuration is computed and ionic states, which are supposed to emerge during resonant charge transport, are described within Koopmans' theorem i.e. via an additional electron/hole in the corresponding molecular orbital. Only few researchers take excited configurations explicitly into account [42]. It should also be mentioned that, while the use of Koopmans' theorem in HF can be justified for all molecular orbitals, this is not the case for the Kohn-Sham orbitals in DFT, where a similar relation exists only for the HOMO.

Hartree-Fock theory is not a good choice for the computation of molecular junctions, as it does not account for electron-correlation effects, which are expected to play an important role in electron transport. As the described systems are usually large and contain metal atoms, density functional theory is expected to perform better. However, it was found, that DFT has a tendency towards underestimating the HOMO-LUMO-gap, predicting a too metallic behavior, and overestimating the broadening [43], and it was suggested that functionals optimized for transport problems, including non-equilibrium functionals, should be developed.

3.4 Determination of the Parameters

The parameters for the extended molecule were determined employing electronic-structure calculations, performed with the TURBOMOLE package (Version 5-7) [44] using DFT with the B3-LYP hybrid functional. A double split valence, SV(P), basis set of Gaussian type atomic orbitals including polarization functions and an effective core potential, describing 60 core electrons, ECP-60-MWB, on the gold atoms is used. The B3-LYP functional was chosen based on test calculations with various functionals, although it has the practical disadvantage, that the timesaving resolution of identity approximation [45] cannot be used.

In the B3-LYP functional both the exchange functional, E_x, and the correlation functional, E_c, are a combination of local density approximation (LDA) type functionals and generalized gradient approximation (GGA) type functionals, where the exchange functional additionally contains exact HF exchange contributions,

$$E_{xc}^{B3-LYP} = (1-a)E_x^{LDA} + bE_x^{GGA} + aE_x^{HF} + (1-c)E_c^{LDA} + cE_c^{GGA} \ ,$$

where the three parameters a, b, and c were optimized to fit the results of high-level quantum chemistry methods or experimental data to give a=0.2, b=0.72, and c=0.81.

The final structures of the extended molecules were obtained in several optimization cycles: A full geometry optimization of the isolated neutral molecule was followed by a full geometry optimization of the molecule after replacing the hydrogens on sulfur by two gold atoms. Covalent bonding to two gold atoms is the preferred bond formation, if no symmetry constraints are applied [13, 46]. Afterwards, a second metal layer, containing 5 gold atoms, was added, and the system's geometry was again optimized in order to determine a more realistic molecule-contact binding configuration, this time keeping the internal coordinates of the second gold layer fixed.

It is quite common to use structures where the sulfur atom binds to three gold atoms which form a triangle, separated by the bulk distance of 2.88 Å. This geometry, which has the advantage that calculations can be done in three-fold symmetry groups, contradicts chemical intuition, because the sp^3-hybridization of the sulfur atom would cause the sulfur-gold bonds to be under strong strain.

Another chemically non-intuitive approximation, that is often found in the literature, is to assume that sulfur binds to a perfectly symmetric surface. The interaction between sulfur and gold is usually so strong that it destroys the lattice geometry close to the adsorption site. In test calculations we performed a full geometry optimization of a benzenedithiol molecule bonded between two Au_{13}-clusters in symmetry-group C_1. The gold clusters, which initially formed perfect cuboctahedrons, became amorphous in the course of the optimization procedure and the sulfur atoms ended up bonded to two gold atoms only. A similar effect was found for chemisorption of benzenethiol on a Ag_{51} cluster in Ref. [47].

The nuclear degrees of freedom of the molecular bridge were characterized based on a normal mode analysis of the system with two gold layers. Thereby, the mass of the gold atoms was set to 10^9 atomic mass units, in order to obtain separation of the nuclear motion in the molecule and the gold clusters.

After the normal mode analysis, the metal contacts were enlargened by increasing the second layer by several atoms and/or adding two more metal layers, which are cutouts of the (111)-plain of the face-centered-cubic lattice of solid gold.

A DFT electronic structure single point calculation was performed on this system, which yielded the Kohn-Sham and overlap matrices, that enter the

projection procedure described in Sec. 3.2. In all our model systems direct contact-contact coupling, V^{LR}, was small enough to be neglected, because of the relatively large distance between the two metal clusters.

The vibronic coupling constants $\kappa_l^{(j)}$ were obtained from the numerical gradients of the energies E_j with respect to the dimensionless normal coordinates q_l. To this end, two DFT calculations with molecular geometries elongated along the positive and negative vibrational normal mode coordinate were performed. These calculations were done for the extended molecule using the normal modes of the smaller two-layer system. The elongation parameter, Δ, was chosen to be 0.1. Test calculations have shown that this value is large enough to avoid numerical problems, but also small enough so that the difference quotient is still a good approximation to the differential quotient. After projection the vibronic coupling parameters were calculated as follows,

$$\kappa_l^{(j)} = \left(\frac{\partial E_j}{\partial q_l} \right)_{q=q_{eq}} \approx \frac{E_j(q_{eq} + \Delta q_l) - E_j(q_{eq} - \Delta q_l)}{2\Delta} \quad . \tag{3.13}$$

In principle, all the parameters appearing in Eqs. (3.8) and (3.9) may depend on the external voltage and on the voltage induced molecular charge, and would have to be recalculated at any voltage value. In this work, however, we will, for simplicity, assume that the voltage dependence appears only as a shift in the real part of the contact eigenenergies, $E_{k_L} \to E_{k_L} \pm \eta\, e\, U$ and $E_{k_R} \to E_{k_R} \pm (1-\eta) e\, U$, and the chemical potentials, $\mu_L = \epsilon_f \pm \eta\, e\, U$ and $\mu_L = \epsilon_f \pm (1-\eta) e\, U$. Here η is the voltage division factor, which specifies the amount of the voltage drop in the individual electrodes, and which is 0.5 in a symmetric junction.

A method which includes the voltage dependence implicitly in the DFT calculation is the NEGF-DFT formalism, which is not to be confused with the NEGF-transport formalism introduced in Sec. 2.2. NEGF-DFT constitutes a method to derive the electronic properties of a molecular junction, where the DFT equations are solved by NEGF methods [48]. In this connection, the bias potential is included self-consistently, so that the influence of the voltage on the molecular orbitals and the electrodes is computed rigorously, and no assumptions on the position of the voltage drop and the voltage division factor have to be made. NEGF-DFT is computationally demanding as an electronic structure calculation has to be done at each voltage value.

Chapter 4

Scattering Theory

The idea to view transport through mesoscopic conductors as a scattering process goes back to R. Landauer [7], who first considered elastic, coherent transport in the linear response regime (at small voltages U), and showed that under these conditions the current is given by the transmission probability at the Fermi level $T(\epsilon_f)$,

$$I = g_0 \; T(\epsilon_f) U \; .$$

Scattering theory approaches have since been extended to transport at larger voltages [25] and also to include inelastic effects [2].

In this chapter we will employ an inelastic scattering formalism to describe charge transport through MMM-junctions. In the first part we introduce and derive the method and in the second part we present applications to several model molecular junctions.

4.1 Scattering Theory Formalism

4.1.1 Transmission Probability

The central quantity in the scattering theory approach is the transmission function, $T(E_i, E_f)$, which describes the probability that a charge carrier with initial energy E_i is scattered by the molecule. After the scattering process the charge carrier has energy E_f. The transmission probability is determined by the matrix elements of the $\hat{T}$-operator,

$$\hat{T} = V + VGV \; . \tag{4.1}$$

Here, G is the total, energy-dependent, retarded Green's function,

$$G(E) = \lim_{\eta \to 0^+} [(E + i\,\eta)\mathbf{1} - H]^{-1} = \left[E^+ - H\right]^{-1} \; , \tag{4.2}$$

where $\mathbf{1}$ is the unit-operator, H is the Hamiltonian of the total system (Eqs. (3.9)), and η is a positive infinitesimal. The first term in Eq. (4.1), which corresponds to direct electrode-electrode coupling, in our applications is small enough to be neglected.

If vibronic interactions on the molecule are taken into account, the situation can be viewed as a multi-channel scattering problem. The probability of electron scattering from the left electrode to the right electrode is given by

$$\begin{aligned} T_{R\leftarrow L}(E_i, E_f) &= 4\pi^2 \sum_{\boldsymbol{\nu}_i,\boldsymbol{\nu}_f} \sum_{k_i\in L} \sum_{k_f\in R} P_{\boldsymbol{\nu}_i}\, \delta(E_f + E_{\boldsymbol{\nu}_f} - E_i - E_{\boldsymbol{\nu}_i}) \qquad (4.3) \\ &\quad \times \delta(E_i - E_{k_i})\delta(E_f - E_{k_f}) \left|\langle \boldsymbol{\nu}_f|\langle\phi_{k_f}|VG(E_i)V|\phi_{k_i}\rangle|\boldsymbol{\nu}_i\rangle\right|^2 . \end{aligned}$$

Here, $|\phi_k\rangle$ denotes asymptotic electronic single particle states in the electrodes, and $|\boldsymbol{\nu}\rangle$ describes asymptotic vibrational states on the molecule. The vibrational function $|\boldsymbol{\nu}\rangle$ is a product of the harmonic oscillator wavefunctions of the individual modes l, $|\boldsymbol{\nu}\rangle = \prod_l |\nu_l\rangle$. $P_{\boldsymbol{\nu}_i} = \langle \boldsymbol{\nu}_i|\rho_0|\boldsymbol{\nu}_i\rangle$ denotes the population probability of the initial vibrational state, where

$$\rho_0 = e^{-H_{n0}/(k_BT)}/Z$$

is the equilibrium density operator in the vibrational subspace, with

$$Z = \sum_l \langle \boldsymbol{\nu}_l|e^{-H_{n0}/(k_BT)}|\boldsymbol{\nu}_l\rangle$$

being the corresponding partition function.

In Eq. (4.3) the δ-function accounts for energy conservation, $E_{\boldsymbol{\nu}_f} + E_f = E_{\boldsymbol{\nu}_i} + E_i$, with $E_{\boldsymbol{\nu}_i}$ and $E_{\boldsymbol{\nu}_f}$ being the energies of the initial and final vibrational states, $|\boldsymbol{\nu}_i\rangle$ and $|\boldsymbol{\nu}_f\rangle$, and E_i and E_f are the initial and final energies of the scattered electron in the left and right electrode, respectively.

Eq. (4.3) describes the transmission probability for electron transport through the unoccupied orbitals of the molecule. If transport through the HOMO is the dominating process, the transmission probability is given by

$$\begin{aligned} T_{R\leftarrow L}(E_i, E_f) &= 4\pi^2 \sum_{\boldsymbol{\nu}_i,\boldsymbol{\nu}_f} \sum_{k_i\in L} \sum_{k_f\in R} P_{\boldsymbol{\nu}_i}\, \delta(E_f - E_{\boldsymbol{\nu}_f} - E_i + E_{\boldsymbol{\nu}_i}) \qquad (4.4) \\ &\quad \times \delta(E_i - E_{k_i})\delta(E_f - E_{k_f}) \left|\langle \boldsymbol{\nu}_f|\langle\phi_{k_f}|VG(E_i)V|\phi_{k_i}\rangle|\boldsymbol{\nu}_i\rangle\right|^2 . \end{aligned}$$

Here, the δ-function again accounts for energy conservation, $E_{\boldsymbol{\nu}_f} - E_f = E_{\boldsymbol{\nu}_i} - E_i$, with $E_{\boldsymbol{\nu}_i}$ and $E_{\boldsymbol{\nu}_f}$ being the energies of the initial and final vibrational states, $|\boldsymbol{\nu}_i\rangle$ and $|\boldsymbol{\nu}_f\rangle$, and E_i and E_f are the initial and final electronic energies of the scattered hole in the left and right electrode, respectively.

If vibrational motion can be neglected, equations (4.3) and (4.5) result in the same expression for the purely elastic transmission probability,

$$T_{R\leftarrow L}(E) = 4\pi^2 \sum_{k_i\in L}\sum_{k_f\in R} \delta(E-E_{k_i})\delta(E-E_{k_f}) \left|\langle\phi_{k_f}|VG(E)V|\phi_{k_i}\rangle\right|^2 \ .$$

The differentiation between hole and electron transport transmission probabilities already indicates, that the multi-channel scattering formalism outlined above cannot be used, if the HOMO or LUMO are located close to the Fermi energy. In this case the level-shift and splitting due to nuclear motion may change the occupation of the molecular orbital.

In the systems considered in this work, the charge carriers couple primarily to modes with relatively high frequencies ($\omega > 300\,\mathrm{cm}^{-1}$). At room temperature or below only the vibrational ground state of these modes will be occupied significantly. Therefore, the density operator ρ_0 will be identified with the operator of the vibrational ground state, $\rho_0 = |\mathbf{0}\rangle\langle\mathbf{0}|$.

4.1.2 Trace Formula

The transmission functions in Eqs. (4.3) and (4.5) contain operators that are defined in the infinite space of the total molecular function. In this section an alternative formulation of the transmission function will be derived, which only involves operators in the finite molecular space. The involved operations are similar for the electron and hole transmission functions, but will be written for hole transport, as this is the dominant transport mechanism in the applications presented below.

We start by rewriting Eq. (4.5),

$$\begin{aligned} T_{R\leftarrow L}(E_i,E_f) \;=\; & 4\pi^2 \sum_{\boldsymbol{\nu}_i,\boldsymbol{\nu}_f}\sum_{k_i\in L}\sum_{k_f\in R} P_{\boldsymbol{\nu}_i}\ \delta(E_f - E_{\boldsymbol{\nu}_f} - E_i + E_{\boldsymbol{\nu}_i}) \\ & \times\delta(E_i-E_{k_i})\,\delta(E_f-E_{k_f}) \\ & \times\langle\boldsymbol{\nu}_i|\langle\phi_{k_i}|VG^\dagger(E_i)V|\phi_{k_f}\rangle|\boldsymbol{\nu}_f\rangle\langle\boldsymbol{\nu}_f|\langle\phi_{k_f}|VG(E_i)V|\phi_{k_i}\rangle|\boldsymbol{\nu}_i\rangle \ . \end{aligned}$$

Next we define the projection operators P, Q_L, and Q_R, which project onto the molecular space, the left electrode space, and the right electrode space, respectively,

$$P = \sum_{j\in M}|\phi_j\rangle\langle\phi_j|, \quad Q_L = \sum_{k\in L}|\phi_k\rangle\langle\phi_k|, \quad Q_R = \sum_{k\in R}|\phi_k\rangle\langle\phi_k|,$$

and insert their sum, $P + Q_L + Q_R = 1$, on the left and right side of each V-operator. Expanding the obtained expression yields numerous terms, the

majority of which vanishes, because the operator V only couples M with L or R,

$$\begin{aligned}(P+Q_L+Q_R)|\phi_{k_f}\rangle &= Q_R|\phi_{k_f}\rangle = |\phi_{k_f}\rangle \ , \\ (P+Q_L+Q_R)|\phi_{k_i}\rangle &= Q_L|\phi_{k_i}\rangle = |\phi_{k_i}\rangle \ .\end{aligned}$$

This leads us to

$$\begin{aligned}T_{R\leftarrow L}(E_i,E_f) &= 4\pi^2 \sum_{\boldsymbol{\nu}_i,\boldsymbol{\nu}_f} \sum_{k_i\in L} \sum_{k_f\in R} P_{\boldsymbol{\nu}_i}\ \delta(E_f-E_{\boldsymbol{\nu}_f}-E_i+E_{\boldsymbol{\nu}_i})\delta(E_i-E_{k_i}) \\ &\quad \times \delta(E_f-E_{k_f})\,\langle\boldsymbol{\nu}_i|\langle\phi_{k_i}|VP\ PG^\dagger(E_i)P\ PV|\phi_{k_f}\rangle|\boldsymbol{\nu}_f\rangle \\ &\quad \times \langle\boldsymbol{\nu}_f|\langle\phi_{k_f}|VP\ PG(E_i)P\ PV|\phi_{k_i}\rangle|\boldsymbol{\nu}_i\rangle \ , \qquad (4.5)\end{aligned}$$

where we used the idempotency of the projection operator, $P^2=P$. $PG(E_i)P$ is the Green's function projected onto the molecular space, which will be referred to as $G_M(E_i)$. An expression for $G_M(E_i)$, which is used in the practical calculations, will be derived in the next section. In order to simplify Eq. (4.5), the remaining P-operators will be written explicitly and the terms will be rearranged yielding the following expression,

$$\begin{aligned}T_{R\leftarrow L}(E_i,E_f) &= \sum_{\boldsymbol{\nu}_i,\boldsymbol{\nu}_f} \sum_{a,b,c,d\in M} P_{\boldsymbol{\nu}_i}\ \delta(E_f-E_{\boldsymbol{\nu}_f}-E_i+E_{\boldsymbol{\nu}_i}) \\ &\quad \times \sum_{k_i\in L} 2\pi\delta(E_i-E_{k_i})\langle\boldsymbol{\nu}_i|\langle\phi_d|V|\phi_{k_i}\rangle\langle\phi_{k_i}|V|\phi_a\rangle\langle\phi_a|G_M^\dagger(E_i)|\phi_b\rangle|\boldsymbol{\nu}_f\rangle \\ &\quad \times \sum_{k_f\in R} 2\pi\delta(E_f-E_{k_f})\langle\boldsymbol{\nu}_f|\langle\phi_b|V|\phi_{k_f}\rangle\langle\phi_{k_f}|V|\phi_c\rangle\langle\phi_c|G_M(E_i)|\phi_d\rangle|\boldsymbol{\nu}_i\rangle \ .\end{aligned}$$

Here, we used that V is assumed to be independent of vibrational motion and therefore commutes with the vibrational states. We note that the scattering treatment can be extended to include the dependence of the coupling elements between molecule and contact on the nuclear coordinates [49].

Defining the matrix elements of the energy dependent left and right width function Γ_L and Γ_R as

$$\begin{aligned}\Gamma_L(E_i)_{da} &= \langle\phi_d|\Gamma_L(E_i)|\phi_a\rangle = \sum_{k_i\in L} 2\pi\delta(E_i-E_{k_i})\langle\phi_d|V|\phi_{k_i}\rangle\langle\phi_{k_i}|V|\phi_a\rangle \ , \\ \Gamma_R(E_f)_{bc} &= \langle\phi_b|\Gamma_R(E_f)|\phi_c\rangle = \sum_{k_f\in R} 2\pi\delta(E_f-E_{k_f})\langle\phi_b|V|\phi_{k_f}\rangle\langle\phi_{k_f}|V|\phi_c\rangle \ ,\end{aligned}$$

leads us to

$$\begin{aligned} T_{R\leftarrow L}(E_i,E_f) &= \sum_{\boldsymbol{\nu}_i,\boldsymbol{\nu}_f}\sum_{a,b,c,d\in M} P_{\boldsymbol{\nu}_i}\ \delta(E_f-E_{\boldsymbol{\nu}_f}-E_i+E_{\boldsymbol{\nu}_i}) \\ &\quad\times\langle\boldsymbol{\nu}_i|\langle\phi_d|\Gamma_L(E_i)|\phi_a\rangle\langle\phi_a|G_M^\dagger(E_i)|\phi_b\rangle|\boldsymbol{\nu}_f\rangle \\ &\quad\times\langle\boldsymbol{\nu}_f|\langle\phi_b|\Gamma_R(E_f)|\phi_c\rangle\langle\phi_c|G_M(E_i)|\phi_d\rangle|\boldsymbol{\nu}_i\rangle\ , \end{aligned}$$

which, because of the idempotency of P, can be written as

$$\begin{aligned} T_{R\leftarrow L}(E_i,E_f) &= \sum_{\boldsymbol{\nu}_i,\boldsymbol{\nu}_f}\sum_{d\in M} P_{\boldsymbol{\nu}_i}\ \delta(E_f-E_{\boldsymbol{\nu}_f}-E_i+E_{\boldsymbol{\nu}_i}) \\ &\quad\times\langle\boldsymbol{\nu}_i|\langle\phi_d|\Gamma_L(E_i)G_M^\dagger(E_i)|\boldsymbol{\nu}_f\rangle\langle\boldsymbol{\nu}_f|\Gamma_R(E_f)G_M(E_i)|\phi_d\rangle|\boldsymbol{\nu}_i\rangle\ . \end{aligned}$$

The sum over d corresponds to a trace operation in the electronic molecular space,

$$\begin{aligned} T_{R\leftarrow L}(E_i,E_f) &= \sum_{\boldsymbol{\nu}_i,\boldsymbol{\nu}_f}\mathrm{tr}\Big\{P_{\boldsymbol{\nu}_i}\ \delta(E_f-E_{\boldsymbol{\nu}_f}-E_i+E_{\boldsymbol{\nu}_i}) \\ &\quad\times\ \langle\boldsymbol{\nu}_i|\Gamma_L(E_i)G_M^\dagger(E_i)|\boldsymbol{\nu}_f\rangle\langle\boldsymbol{\nu}_f|\Gamma_R(E_f)G_M(E_i)|\boldsymbol{\nu}_i\rangle\Big\}\ . \end{aligned}$$

Using $\langle\boldsymbol{\nu}_i|E_{\boldsymbol{\nu}_i}=\langle\boldsymbol{\nu}_i|H_{n0}$ and the expression for $P_{\boldsymbol{\nu}_i}$ we obtain

$$\begin{aligned} T_{R\leftarrow L}(E_i,E_f) &= \sum_{\boldsymbol{\nu}_i,\boldsymbol{\nu}_f}\mathrm{tr}\Big\{\langle\boldsymbol{\nu}_i|\rho_0|\boldsymbol{\nu}_i\rangle\langle\boldsymbol{\nu}_i|\ \delta(E_f-E_{\boldsymbol{\nu}_f}-E_i+H_{n0}) \\ &\quad\times\Gamma_L(E_i)G_M^\dagger(E_i)|\boldsymbol{\nu}_f\rangle\langle\boldsymbol{\nu}_f|\Gamma_R(E_f)G_M(E_i)|\boldsymbol{\nu}_i\rangle\Big\}\ . \end{aligned}$$

Because ρ_0 and $|\boldsymbol{\nu}_i\rangle\langle\boldsymbol{\nu}_i|$ commute, the sum over $\boldsymbol{\nu}_i$ results in the trace over the vibrational degrees of freedom and we finally obtain the trace formula of the molecular transmission function for hole transport

$$\begin{aligned} T_{R\leftarrow L}(E_i,E_f) &= \sum_{\boldsymbol{\nu}_f}\mathrm{tr}\Big\{\ \delta(E_f-E_{\boldsymbol{\nu}_f}-E_i+H_{n0})\rho_0 \\ &\quad\times\Gamma_L(E_i)G_M^\dagger(E_i)|\boldsymbol{\nu}_f\rangle\langle\boldsymbol{\nu}_f|\Gamma_R(E_f)G_M(E_i)\Big\}\ \text{(h. t.)}\ . \end{aligned} \tag{4.7}$$

For electron transport, on the other hand, we obtain in the same way,

$$\begin{aligned} T_{R\leftarrow L}(E_i,E_f) &= \sum_{\boldsymbol{\nu}_f}\mathrm{tr}\Big\{\ \delta(E_f+E_{\boldsymbol{\nu}_f}-E_i-H_{n0})\rho_0 \\ &\quad\times\Gamma_L(E_i)G_M^\dagger(E_i)|\boldsymbol{\nu}_f\rangle\langle\boldsymbol{\nu}_f|\Gamma_R(E_f)G_M(E_i)\Big\}\ \text{(e. t.)}\ . \end{aligned} \tag{4.8}$$

The total transmission probability, $T_{R\leftarrow L}(E_i)$, is obtained by integrating $T_{R\leftarrow L}(E_i, E_f)$ over the final energies of the charge carrier,

$$T_{R\leftarrow L}(E_i) = \int \mathrm{d}E_f T_{R\leftarrow L}(E_i, E_f) \ .$$

In the absence of vibronic coupling, Eqs. (4.7) and (4.8) reduce to

$$T(E) = \mathrm{tr}\left\{\Gamma_L(E) G_M^{\dagger}(E) \Gamma_R(E) G_M(E)\right\} \ . \tag{4.9}$$

4.1.3 Molecular Green's function

In this section we will derive an expression for the Green's function projected onto the molecular subspace, $G_M = PGP$.

The starting point is the Lippmann-Schwinger equation [50]

$$G = G_0 + G_0 V G \quad , \tag{4.10}$$

where G_0 is the Green's function related to the electronically uncoupled Hamiltonian H_0,

$$\begin{aligned} G_0 &= \left[E^+ - H_0\right]^{-1} \ , \\ H_0 &= H_{n0} + H_M + H_L + H_R \qquad \text{(electron transport)} \ , \\ H_0 &= H_{n0} - H_M - H_L - H_R \qquad \text{(hole transport)} \ . \end{aligned}$$

The energy dependence of G and G_0 is not written for clarity. Applying the projection operator P from both sides to Eq. (4.10) we obtain

$$G_M = PGP = PG_0P + PG_0VGP \quad .$$

The sum of projection operators, $P + Q_L + Q_R = 1$, is inserted on both sides of the operator V. Using similar arguments as in Sec. (4.1.2), it can be shown that only three terms remain

$$G_M = PGP = PG_0P + PG_0PVQ_LGP + PG_0PVQ_RGP \quad . \tag{4.11}$$

The terms Q_LGP and Q_RGP can again be evaluated using the Lippmann-Schwinger equation and inserting $1 = P + Q_L + Q_R$. This leads to

$$Q_LGP = Q_LG_0Q_LVPGP \quad .$$

and a similar expression for Q_RGP. Inserting this equation into Eq. (4.11) gives

$$\begin{aligned} G_M &= PG_0P + PG_0PVQ_LG_0Q_LVPGP + PG_0PVQ_RG_0Q_RVPGP \ , \\ &= PG_0P + PG_0P\tilde{\Sigma}_LPGP + PG_0P\tilde{\Sigma}_RPGP \ , \\ &= PG_0P + PG_0P\tilde{\Sigma}_LG_M + PG_0P\tilde{\Sigma}_RG_M \ , \end{aligned} \tag{4.12}$$

where the idempotency of P was used and where we have introduced the retarded self-energy

$$\begin{aligned}\tilde{\Sigma}_L &= PVQ_L G_0 Q_L VP \ , \\ \tilde{\Sigma}_R &= PVQ_R G_0 Q_R VP \ .\end{aligned}$$

Eq. (4.12) can be rearranged as

$$G_M = \left[E^+ - PG_0P\tilde{\Sigma}_L - PG_0P\tilde{\Sigma}_R\right]^{-1} PG_0P \quad ,$$

where the positive infinitesimal η was reintroduced (cf. Eq. (4.2)).

Using the operator relation $A^{-1}B = [B^{-1}A]^{-1}$ we obtain

$$\begin{aligned}G_M &= \left[(PG_0P)^{-1}\left(E^+ - PG_0P\tilde{\Sigma}_L - PG_0P\tilde{\Sigma}_R\right)\right]^{-1} \\ &= \left[(PG_0P)^{-1} - \tilde{\Sigma}_L - \tilde{\Sigma}_R\right]^{-1} \\ &= \left[E^+ - PHP - \tilde{\Sigma}_L - \tilde{\Sigma}_R\right]^{-1} \ ,\end{aligned}$$

with

$$\begin{aligned}PHP &= H_{n0} - H_{ne} - H_M \qquad \text{(e. t.)} \ , \\ PHP &= H_{n0} + H_{ne} + H_M \qquad \text{(h. t.)} \ .\end{aligned}$$

Writing the energy dependence of the Green's function explicitly, we obtain the expressions,

$$G_M(E) = \left[E^+ - PHP - \tilde{\Sigma}_L(E) - \tilde{\Sigma}_R(E)\right]^{-1} \tag{4.13}$$

$$\begin{aligned}\tilde{\Sigma}_L(E) &= PVQ_L \, G_0(E) \, Q_L VP \\ \tilde{\Sigma}_L(E) &= PVQ_L \left[E^+ - Q_L H Q_L\right]^{-1} Q_L VP \ .\end{aligned} \tag{4.14}$$

Using

$$\begin{aligned}Q_L H Q_L &= H_{n0} - H_L \qquad \text{(e. t.)} \ , \\ Q_L H Q_L &= H_{n0} + H_L \qquad \text{(h. t.)} \ ,\end{aligned}$$

the expressions for the self-energy operators read

$$\begin{aligned}\tilde{\Sigma}_L(E) &= PVQ_L \left[E^+ - H_{n0} + H_L\right]^{-1} Q_L VP \qquad \text{(e. t.)} \ , \\ \tilde{\Sigma}_L(E) &= PVQ_L \left[E^+ - H_{n0} - H_L\right]^{-1} Q_L VP \qquad \text{(h. t.)} \ .\end{aligned}$$

As in our model the electronic coupling is assumed to be independent of the vibrational motion, we can rewrite Eq. (4.14) in a form that does not contain the vibrational Hamiltonian in $\tilde{\Sigma}(E)$. We define a slightly altered self-energy function

$$\Sigma_L(E) \;=\; PVQ_L\left[E^+ - H_L\right]^{-1} Q_L V P \tag{4.15}$$

which is related to the original one via

$$\begin{aligned}\Sigma(E - H_{n0}) &= +\tilde{\Sigma}(E) \qquad \text{(e. t.)}\ ,\\ \Sigma(H_{n0} - E) &= -\tilde{\Sigma}(E) \qquad \text{(h. t.)}\ .\end{aligned}$$

Also the Green's function will be redefined as,

$$\bar{G}_M(E) = \left[E^+ - H_{ne} - H_M - \Sigma_L(E) - \Sigma_R(E)\right]^{-1}\ , \tag{4.16}$$

which is related to the original Green's function as

$$\begin{aligned}\bar{G}_M(E - H_{n0}) &= +G_M(E) \qquad \text{(e. t.)}\ ,\\ \bar{G}_M(H_{n0} - E) &= -G_M(E) \qquad \text{(h. t.)}\ .\end{aligned}$$

The transmission function for electron transport can thus be written as

$$\begin{aligned}T_{R\leftarrow L}(E_i, E_f) \;=\; \sum_{\boldsymbol{\nu}_f} \mathrm{tr}_M \Big\{\ & \delta(E_f + E_{\boldsymbol{\nu}_f} - E_i - H_{n0})\rho_0 \\ & \times \Gamma_L(E_i)\bar{G}_M^{\dagger}(E_i - H_{n0})|\boldsymbol{\nu}_f\rangle\langle\boldsymbol{\nu}_f|\Gamma_R(E_f)\bar{G}_M(E_i - H_{n0})\Big\}\ .\end{aligned} \tag{4.17}$$

The transmission probability for hole transport, on the other hand, finally becomes

$$\begin{aligned}T_{R\leftarrow L}(E_i, E_f) \;=\; \sum_{\boldsymbol{\nu}_f} \mathrm{tr}_M \Big\{\ & \delta(E_f - E_{\boldsymbol{\nu}_f} - E_i + H_{n0})\rho_0 \\ & \times \Gamma_L(E_i)\bar{G}_M^{\dagger}(H_{n0} - E_i)|\boldsymbol{\nu}_f\rangle\langle\boldsymbol{\nu}_f|\Gamma_R(E_f)\bar{G}_M(H_{n0} - E_i)\Big\}\ .\end{aligned} \tag{4.18}$$

The self-energy in Eq. (4.15) describes the interaction of the electrodes with the molecular unit and should not be mistaken for the surface self-energy (Σ^{sf}) in Eq. (3.11). While the surface self-energy describes the influence of the leads on the contacts, the self-energy in Eq. (4.15) describes the influence of the overall electrodes on the molecule.

The matrix elements of the self-energy in Eq. (4.15) are given by

$$\begin{aligned}\Sigma_L(E)_{ij} \;&=\; \sum_{k,k'\in L} \langle\phi_i|V|\phi_k\rangle\langle\phi_k|\frac{1}{(E^+ - H_L)}|\phi_{k'}\rangle\langle\phi_{k'}|V|\phi_j\rangle\ , \qquad (4.19)\\ \Sigma_L(E)_{ij} \;&=\; \sum_{k\in L} \frac{V_{ik}\,V_{kj}}{(E^+ - E_k)} = \Delta_L(E)_{ij} - \frac{i}{2}\Gamma_L(E)_{ij}\ .\end{aligned}$$

The self-energy function describes the level-shift, Δ, and the level-broadening, Γ, of the molecular states due to coupling to the metallic electrodes. The matrix elements of Γ were defined in Eqs. (4.6).

When working with the finite number of bi-orthogonal states discussed in App. A, an element of this self-energy in the following calculations is approximated by the expression,

$$\Sigma_L(E)_{ij} = \sum_{k \in L} \frac{V_{ik} V_{kj}}{S_k^u (E^+ - E_k)} \ . \tag{4.20}$$

Here, S_k^u is the overlap of left and right eigenvectors which is defined in App. A.

4.1.4 Calculation of the Current

The transmission function is related to the current via a generalized Landauer equation [2]

$$\begin{aligned} I &= I_{R \leftarrow L} - I_{L \leftarrow R} \\ &= \frac{2e}{h} \int \mathrm{d}E_i \mathrm{d}E_f \, \{ T_{R \leftarrow L}(E_i, E_f) f_L(E_i) [1 - f_R(E_f)] \\ &\quad - T_{L \leftarrow R}(E_i, E_f) f_R(E_i) [1 - f_L(E_f)] \} \ \text{(e. t.)} \ , \end{aligned} \tag{4.21}$$

where the factor 2 accounts for spin degeneracy. The electron transmission probability $T_{R \leftarrow L}(E_i, E_f)$ is weighted by the probability, $f_L(E_i)$, that in the left electrode the state with energy E_i is occupied, while in the right electrode the state with energy E_f is unoccupied, $[1 - f_R(E_f)]$. To obtain the current from left to right, $I_{R \leftarrow L}$, this weighted probability is integrated over all initial and final hole energies. The Fermi function is given by

$$f_{L/R}(E) = \left[e^{\frac{E - (\epsilon_f \pm e\,U/2)}{k\,T}} + 1 \right]^{-1} \ .$$

The terms $[1 - f_R(E_f)]$ and $[1 - f_L(E_f)]$ represent Pauli exclusion or blocking factors, the use of which is discussed critically in the literature [25]. It was argued that, if the electronic coupling between molecule and contacts is strong, the situation does not correspond to a transition between separated states, but a scattering state, consisting of an incoming wave in one electrode and an outgoing wave in the other electrode, is formed and will contribute to transport as long as it is occupied. In this case we are dealing with a single state only, therefore, no exclusion factors are needed, and the following expression should be used instead,

$$I = \frac{2e}{h} \int \mathrm{d}E_i \mathrm{d}E_f \, \{ T_{R \leftarrow L}(E_i, E_f) f_L(E_i) - T_{L \leftarrow R}(E_i, E_f) f_R(E_i) \} \ . \tag{4.22}$$

However, it is generally assumed, that if the coupling between molecule and electrodes is rather small, the probabilistic approach of Eq. (4.21) yields a better description. Neither Eq. (4.21) nor Eq. (4.22) have been derived from sophisticated transport theories so far.

In this work we will use the current formula with the Pauli blocking factors formulated for hole transport

$$\begin{aligned} I &= I_{R\leftarrow L} - I_{L\leftarrow R} \\ &= \frac{2e}{h}\int \mathrm{d}E_i \mathrm{d}E_f \, \{T_{R\leftarrow L}(E_i,E_f) f_R(E_f)[1-f_L(E_i)] \\ &\quad - T_{L\leftarrow R}(E_i,E_f) f_L(E_f)[1-f_R(E_i)]\} \ \text{(h. t.)} \ , \end{aligned} \tag{4.23}$$

Expression (4.23) is valid if many-electron processes are negligible. In particular, non-equilibrium effects in the electrodes and electron correlation due to vibronic coupling are not taken into account. Furthermore, it is implicitly assumed, that between individual scattering processes the system relaxes to the vibrational equilibrium.

In the case of symmetric transmission functions, $T_{R\leftarrow L} = T_{L\leftarrow R}$, i.e. whenever no magnetic fields or other factors, that break microscopic reversibility, are present, and if transport is elastic, $E_i = E_f$, both Eqs. (4.21), (4.22), and (4.23) reduce to the same form,

$$I = \frac{2e}{h}\int \mathrm{d}E \; T(E) \, \{f_R(E) - f_L(E)\} \ . \tag{4.24}$$

Here, the blocking factors are no longer necessary, because transitions from occupied states in the left to occupied states in the right are exactly cancelled by the transitions in the opposite direction.

If we consider the elastic transmission function at $E = \epsilon_f$ and assume it to be independent of voltage, and further expand $\{f_R(E) - f_L(E)\}$ up to first order in U, we obtain the original Landauer equation,

$$I = \frac{2e^2}{h} \; T(\epsilon_f) U = g_0 \; T(\epsilon_f) U \ ,$$

which is valid at low voltages (in the linear response regime).

4.2 Application to Benzenethiolates

In this section the multi-channel scattering formalism, presented in the previous section, is applied to several MMM-junctions. The molecular units of these junctions consist of a phenyl ring that is bonded to two gold cluster via

alkane thiolate-linkers of different lengths. We present the calculated transmission probabilities and currents for these systems and compare between purely electronic and vibronic features.

A few technical details of the calculations that concern all molecular junctions investigated in this section will be mentioned before.

- The model systems exhibit either symmetry group C_i or C_2, which does not only halve CPU-time in the DFT-calculation, but also simplifies the ensuing transport calculations as it establishes a left-right symmetry and thus makes the current an odd function of voltage, so only the positive voltage range will be shown.

- The Fermi energy was approximated as the average value of the HOMO and LUMO of the extended molecule.

- The temperature was set to T=0 K in all computations.

- In order to reduce the computational effort, only those four vibrational modes with the strongest effective coupling were explicitly taken into account. The effective coupling was determined by the ratio of the vibronic coupling parameter $\kappa_l^{(j)}$ and the electronic coupling characterized by the width function Γ at the molecular eigenenergies E_j of the involved molecular orbitals.

- A vibrational basis set consisting of 12 to 16 functions per mode was used. This number was first converged in calculations including a single mode. For the calculations that include four modes simultaneously not all combinations of vibrational product states were considered, but only those which had a total energy of, $E = \sum_l \hbar\omega_l\nu_l$, smaller than a cutoff energy E_c. Converged results were obtained for E_c=1.5 eV.

4.2.1 Benzenedithiolate

First, we discuss transport through a benzenedithiolate (BDT) molecular junction. This system was chosen, because several experimental [3, 51] studies exist, which triggered numerous theoretical studies, where BDT was investigated using different theories to describe elastic transport [52, 53, 54, 55, 46, 56, 57, 42] and vibronic effects in the off-resonant, tunneling regime [58, 59, 60]. Experimentalists investigated this molecule because, due to the π-electron system, it is expected to be a good conductor, it is rigid, and it forms strong bonds to the gold electrodes.

The extended molecule of this system is shown in Fig. 4.1. The gold contacts are formed by pyramidal gold clusters consisting of 30 gold atoms.

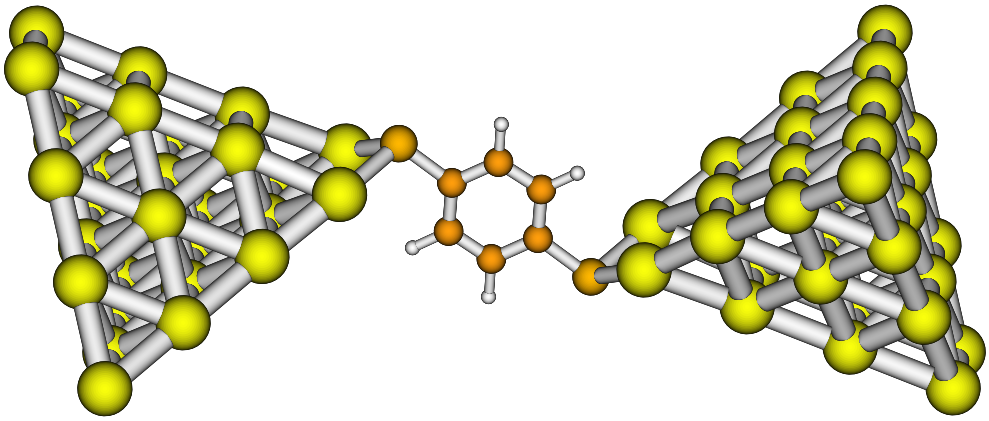

Figure 4.1: The extended molecule of a BDT-junction with two pyramidal gold clusters consisting of 30 gold atoms.

When considering the sulfur atom as the tip of the pyramid, its base is formed by a cutout of the (111)-surface of bulk gold.

The modes that were included in the transport calculation are shown in Fig. 4.2 and can be characterized as a C-C-C bending (a), the benzene ring breathing (b), a C-C-H bending (c), and a C-C stretching mode (d). They are similar to those four modes found to have the largest vibronic coupling parameters in Ref. [58].

As not all 128 orbitals, that span the molecular space of this system, will give a significant contribution to the transport characteristics, only those 7 states, which reproduced the transmission function including all 128 states satisfyingly, were included in the calculation.

In Fig. 4.3 the total transmission probability through a BDT junction is shown. It is plotted relative to the Fermi level, which in this system was approximately -5.10 eV. In addition to the transmission probability based on a vibronic calculation (red line), also the result of a purely electronic calculation (blue line) (where all electronic-nuclear coupling constants $\kappa_l^{(j)}$ were set to zero) is presented.

The transmission probability exhibits several pronounced peaks. There are four peaks at energies -2.66, -2.50, -2.11, and -1.29 eV, respectively, which are caused by the three orbitals depicted in Fig. 4.3. The peak positions are shifted relative to the energies of the orbitals after projection, which are located 2.55 and 0.45 eV below, and +0.76 eV above ϵ_f, respectively. These orbitals are related to the e_{1g}-orbitals of benzene and p-orbitals at the sulfur atoms and are similar to the HOMO-2, HOMO-1, and HOMO of the isolated molecule, respectively. In the isolated molecule these states have energy

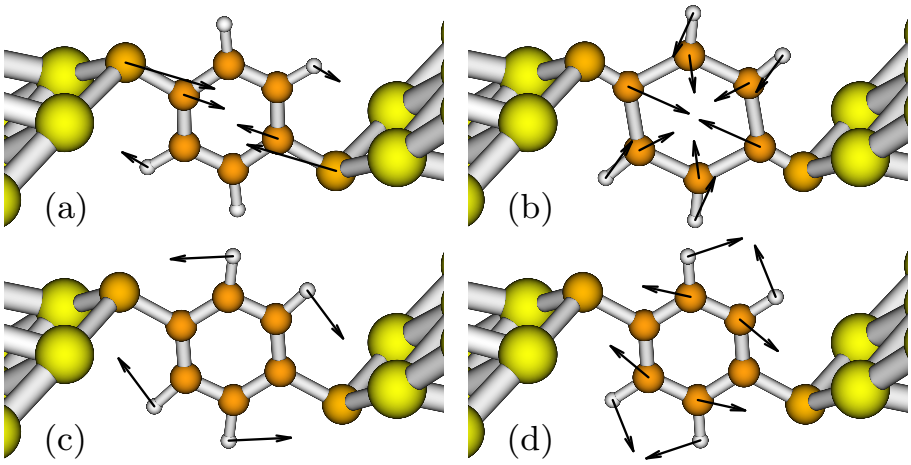

Figure 4.2: Normal modes of BDT included in the calculation. The arrows indicate the direction and relative lengths of the amplitudes.

-2.11, -1.91, and -0.44 eV relative to ϵ_f, respectively.

The levels in the projected space will not be characterized as HOMO or LUMO, as there is a charge flow onto the molecule on bond formation with the gold cluster. Instead a comparison with the states of the isolated molecule (without gold atoms but with hydrogen on sulfur), where the term HOMO is well defined, will be used. The charge flow from the gold atoms to the molecular unit can be estimated by calculating the Mulliken gross population [41], and gives a charge of the molecular unit of - 0.177 e for the BDT junction.

While orbitals B and C in Fig. 4.3 have significant contributions from the bridging sulfur atoms, orbital A is completely localized on the phenyl-ring. As a result, the molecule-contact coupling strength and also the level shift for the three orbitals is quite different: the width function, Γ_{jj}, at zero voltage and the respective peak energy vary from 0.01 eV (A), 0.06 eV (B) to 0.20 eV (C), which corresponds to electronic lifetimes, approximately given by the uncertainty relation $\hbar/\Gamma_{jj}$, of 66 fs (A), 12 fs (B), and 3 fs (C), respectively. Consequently, the structures in the transmission probability caused by orbitals B and C are rather broad, whereas orbital A results in a narrow resonance peak.

The comparison of the vibronic transmission probability (red line in Fig. 4.3) with the results of the purely electronic calculation (blue line) reveals that the electron-nuclear coupling in BDT has significant effects on narrow resonances. In particular, it results in a splitting of the narrow peak at -2.66 eV into a number of smaller structures. These structures are due to

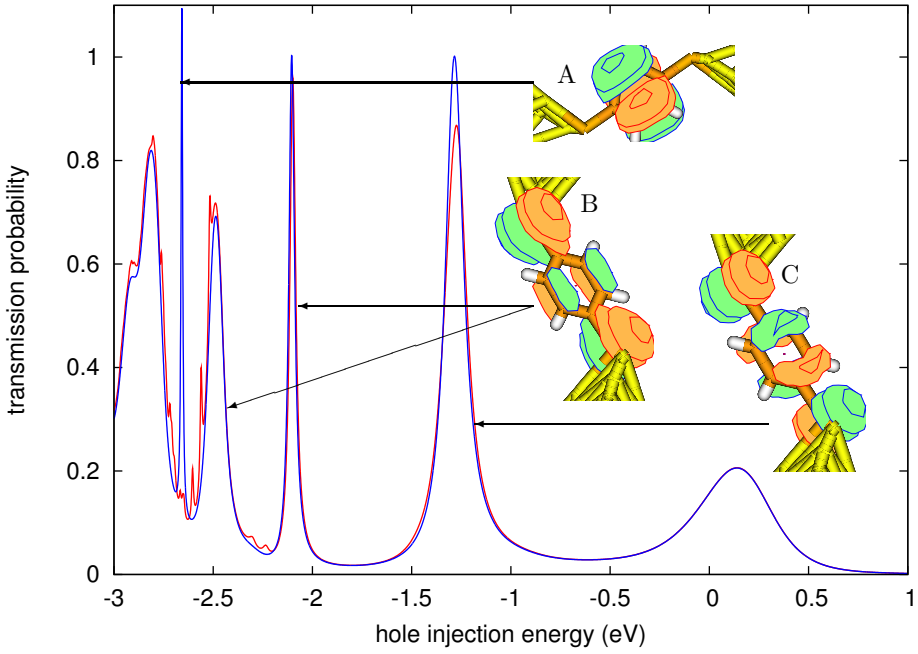

Figure 4.3: Purely Electronic (blue line) and vibronic (red line) total transmission probability through a BDT molecular junction at zero voltage as a function of the initial energy of the electron (relative to the Fermi energy). Molecular orbital plots of the three localized molecular orbitals, denoted A, B, and C, which dominate the transmittance at the indicated peaks, are shown. Only the relevant part of the energy interval [-3:+3], corresponding to a voltage window of 6 V, is shown.

vibronic transitions to the molecular cation state that are weighted by the respective Franck-Condon factors.

The effect of nuclear motion on the other peaks in the transmission probability, on the other hand, is rather small. This can be rationalized by considering the vibronic and electronic coupling constants in the corresponding states. The importance of vibronic effects caused by the nuclear mode q_l in state $|\phi_j\rangle$ is determined by the ratio of the vibronic and electronic coupling constants, $\kappa_l^{(j)}/\Gamma_{jj}$. Although the electronic-vibrational coupling constants $\kappa_l^{(j)}$ of some of the nuclear modes in states $|\phi_B\rangle$ and $|\phi_C\rangle$ are relatively large (cf. Tab. 4.1), the lifetime of the electron on the molecular bridge is short, resulting in a small effective coupling $\kappa_l^{(j)}/\Gamma_{jj}$.

Besides this ratio, vibronic effects for orbitals B and C are also expected to be small, because the residence time of the electrons in these orbitals (12 fs

	ω (cm^{-1})	T (fs)	$\kappa^{(A)}$ (meV)	$\kappa^{(B)}$ (meV)	$\kappa^{(C)}$ (meV)
(a)	349.26	96	61	8	62
(b)	1092.02	31	72	80	33
(c)	1198.14	28	90	13	16
(d)	1627.28	20	152	93	36

Table 4.1: Frequencies and periods (T) of the four most important vibrational modes of BDT as well as gradients of these modes for the three orbitals, A, B, and C, dominating conduction.

and 3 fs, respectively) are much smaller than the periods of the included normal mode vibrations (cf. Tab. 4.1).

In Fig. 4.3 there is another peak at +0.14 eV, which is independent of vibronic coupling. This peak is influenced by orbitals B and C, in the sense that it vanishes if both states are excluded from the transmission calculation, but cannot be exclusively related to any of the orbitals of the molecular bridge. It might be due to a metal-induced gap state [61, 54], which, from IETS-studies [62], is known to appear if tip-like geometries of metal contacts are used.

The simulated current-voltage characteristic of BDT, depicted in Fig. 4.4, exhibits a nonlinear behavior: A small increase of the current at small voltages caused by the peak at ϵ_f is followed by a strong increase at larger voltages resulting from the contributions of orbitals B and C. Because orbitals B and C are strongly coupled to the metal contacts and thus have small effective vibronic coupling, the influence of nuclear motion on the current in BDT is almost negligible.

It is also noted that, similar as in previous (purely electronic) simulations of electron transport through BDT, the current is significantly larger than in experimental results [3, 51], which is probably due to the deficiencies of DFT that were discussed in Sec. 3.3.

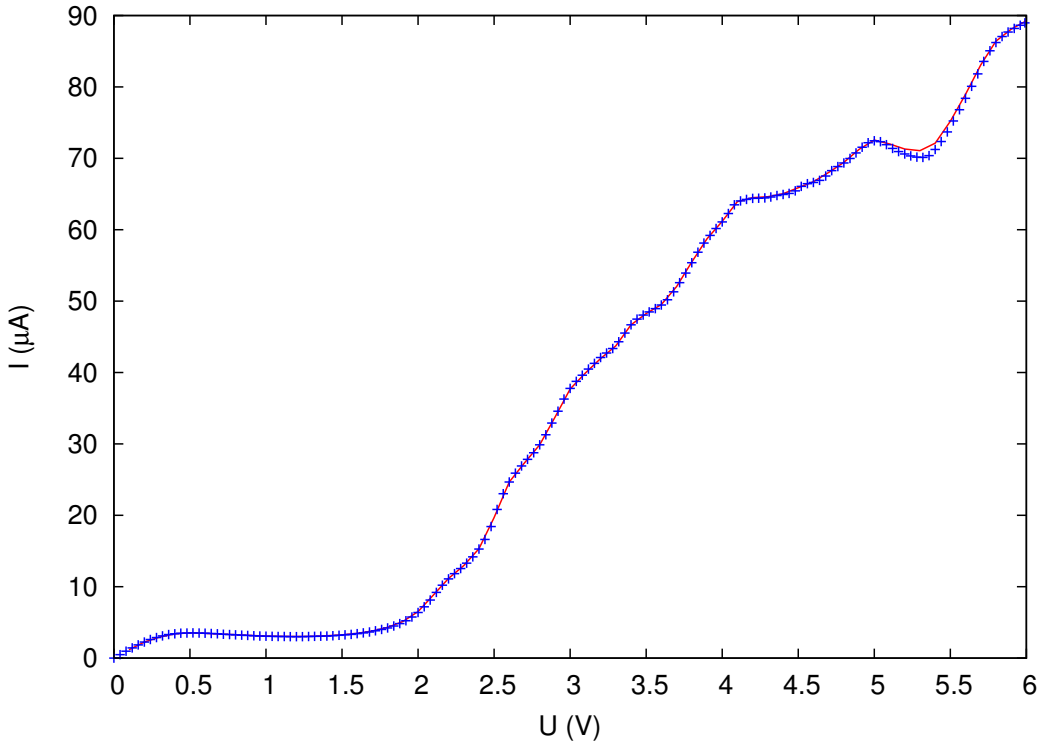

Figure 4.4: Current-voltage characteristic of BDT. Shown are results of calculations with (solid red line) and without (blue crosses) coupling to molecular vibrations.

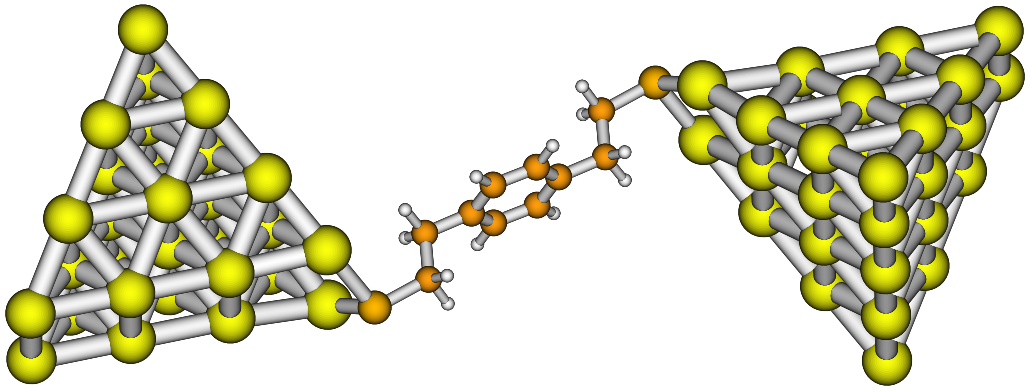

Figure 4.5: The extended molecule of a BDET-junction with two pyramidal gold clusters consisting of 30 gold atoms.

4.2.2 Benzenedi(ethanethiolate)

We saw in the last section, that only small vibronic effects can be seen in the transmission probability and in the I-V characteristic, if the electronic coupling between contacts and molecular orbitals is strong. The coupling between orbitals localized on the benzene ring and the contacts is expected to decrease, if a spacer group is inserted between them. Therefore, in this section we will present investigations on benzene-di(ethanethiolate) (BDET), where two methylene groups on both sides of the benzene ring separate the sulfur atom from the π-electron system. A cartoon of the extended molecule (Fig. 4.5) shows BDET between two pyramidal gold clusters comprising 30 gold atoms.

The charge of the molecular unit, determined by a Mulliken populations analysis, is - 0.026 e and thus significantly smaller than the charge of the molecular unit in the BDT junction of the previous section.

The number of states $|\phi_j\rangle$ on the molecular bridge, which were explicitly included in the calculation of the transmission, was reduced from 200 to 12 including only those with energies in the vicinity of the Fermi level. Similarly, of the total number of 36 totally symmetric normal modes, the four normal modes with the largest ratio between gradient (Eq. (3.13)) and electronic coupling were included in the calculation. They can be characterized as: C-C-C bending (a), C-C-H bending (b), another C-C-C bending (c), and C-C stretching (d) (cf. Fig. 4.6).

The transmission probability of BDET at zero voltage is depicted in Fig. 4.7. The purely electronic transmission (blue line) is dominated by two resonance peaks at energies -2.23 and -1.85 eV, which are caused by molecu-

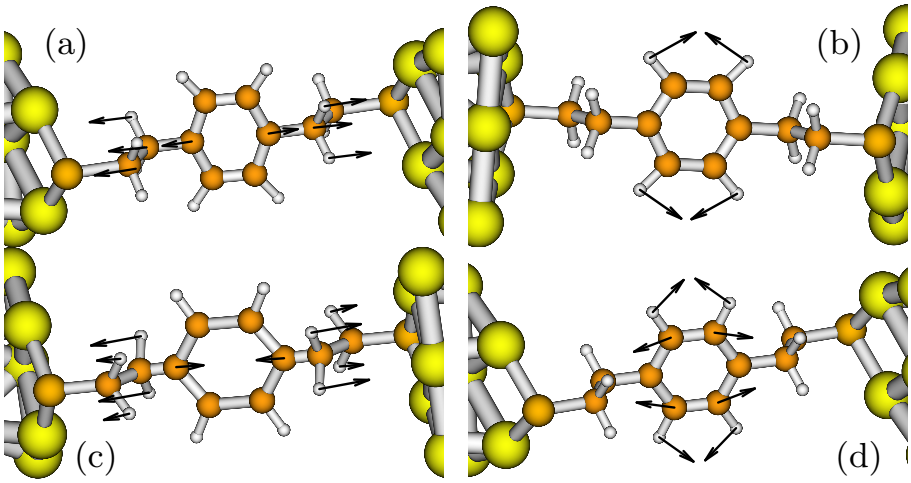

Figure 4.6: Normal modes of BDET included in the calculation.

lar orbitals A and B. Around 0.80 eV a small broad peak due to sulfur states can be seen.

The projected orbitals A and B are similar to the HOMO-3 and HOMO-2 of the isolated molecule, where they are located 1.89 and 1.52 eV below ϵ_f, respectively. The Fermi energy in this system is ϵ_f=-5.15 eV. After projection those orbitals have an energy of -2.23 and -1.84 eV, respectively. The HOMO-1 and HOMO orbitals of the isolated molecule are quasi-degenerate and predominantly localized on the sulfur atoms. While the peak due to orbital A is not shifted with respect to its eigenenergy, the peak due to orbital B is shifted by -0.01 eV. The corresponding vibronic coupling constants in the most important molecular orbitals and the normal mode frequencies are given in Tab. 4.2.

The peak positions in the transmission function do not coincide with the eigenenergies of the states after projection, as both peak position and peak width are influenced by neighboring states. For example, there exist four pairwise degenerate sulfur p-states with energies slightly below the Fermi level, which cause the tiny peak at -0.79 eV in the transmission function, but influence the transport much more via their interaction with states A and B. This interaction is mediated by the gold clusters via the non-diagonal elements in the self-energy matrix.

The shoulder on the left of the peak due to orbital B (blue line) is caused by interactions of orbital B with two states that are energetically located below state A. These states are localized on the spacer groups and the sulfur atoms and do not directly contribute to transmission in the considered energy

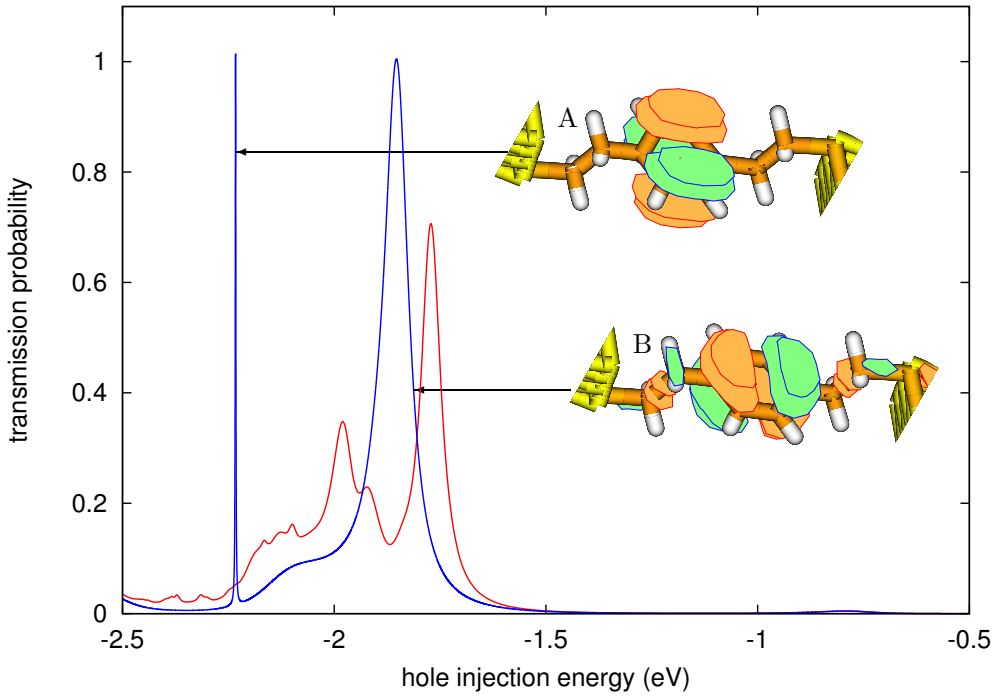

Figure 4.7: Purely electronic (blue line) and vibronic (red line) total transmission probability through a BDET molecular junction with a tip-like gold cluster geometry at zero voltage as a function of the initial energy of the hole (relative to the Fermi energy). The two orbitals, denoted A and B, dominate the transmittance at the indicated peaks. Only the relevant part of the energy interval [-2.5:+2.5], corresponding to a voltage window of 5 V, is shown.

range.

While orbital A resembles an e_{1g}-orbital of benzene, orbital B has additional contributions on the ethyl-groups and the sulfur atoms. As a consequence, state A has smaller electronic coupling to the contacts ($\Gamma_{AA} = 1.9 \cdot 10^{-4}$ eV, corresponding to a lifetime of $\tau = 3466$ fs) resulting in a very narrow peak in the transmission probability, whereas the significant coupling of orbital B to the contacts ($\Gamma_{BB} = 1.1 \cdot 10^{-1}$ eV, $\tau = 6$ fs) results in a rather broad structure.

The comparison between the results of vibronic (red line in Fig. 4.7) and purely electronic (blue line) calculations demonstrates that the electronic-vibrational coupling in BDET alters the transmission probability significantly. The elastic 0_0^0-peak due to state B is shifted to the right by 0.08 eV. Here, spectroscopic notation was used, where the first zero indicates that no

	ω (cm^{-1})	T (fs)	$\kappa^{(A)}$ (meV)	$\kappa^{(B)}$ (meV)
(a)	544.48	61	76	22
(b)	1197.11	28	51	69
(c)	1229.49	27	110	47
(d)	1671.56	20	136	162

Table 4.2: Frequencies, periods (T), and vibronic coupling parameters with respect to the two orbitals (A,B) of the four most important vibrational modes of BDET between pyramidal gold contacts.

vibrations were involved in this transition, the subscript denotes the vibrational quantum number in the neutral reference state, and the superscript denotes the vibrational quantum number in the cation. At -1.92 eV and -1.98 eV single vibrational excitations of mode (b) and (d), respectively, can be seen.

Only side-bands to the left are seen in the vibronic transmission, because phonon absorption is not possible, as the system is assumed to relax into the vibrational ground state, ($\boldsymbol{\nu}_i = \mathbf{0}$), after each electron scattering process and as the temperature is not large enough to significantly populate excited vibrational levels thermally.

The 0_0^0-transition belonging to state A, which is expected to be a narrow line, cannot be seen, because it is coincidentally shifted into resonance with a peak caused by the transmission through sulfur p-states. This latter peak cannot be seen by itself, but it gains width and height on interaction with state A and causes a broadening of the elastic peak due to this state. The structure resulting from this effect can be seen around peak A but it is too broad to assign individual modes. At about -2.15 eV the $(\mathrm{m})_0^2$ transition peaks of state B overlap with the 0_0^0 transition of state A, where (m) denotes all four included modes.

The current-voltage characteristic of BDET is shown in Fig. 4.8. The result obtained from a purely electronic calculation (blue line) shows an increase of the current at about 3.5 V caused by state B, which is followed by a pronounced decrease of the current at 4 V. The weakly coupled state A results only in a small step-like increase of the current shortly before 4.5 V and the following rise is due to the increasing width of the peak which appears at -1.85 eV in the transmission. The negative-differential resistance (NDR) effect at 4 V is caused by the voltage dependence of the self-energies Σ_L, Σ_R and the corresponding width functions Γ.

Including the coupling to the nuclear degrees of freedom changes the current-voltage characteristic substantially. In particular, the electronic-

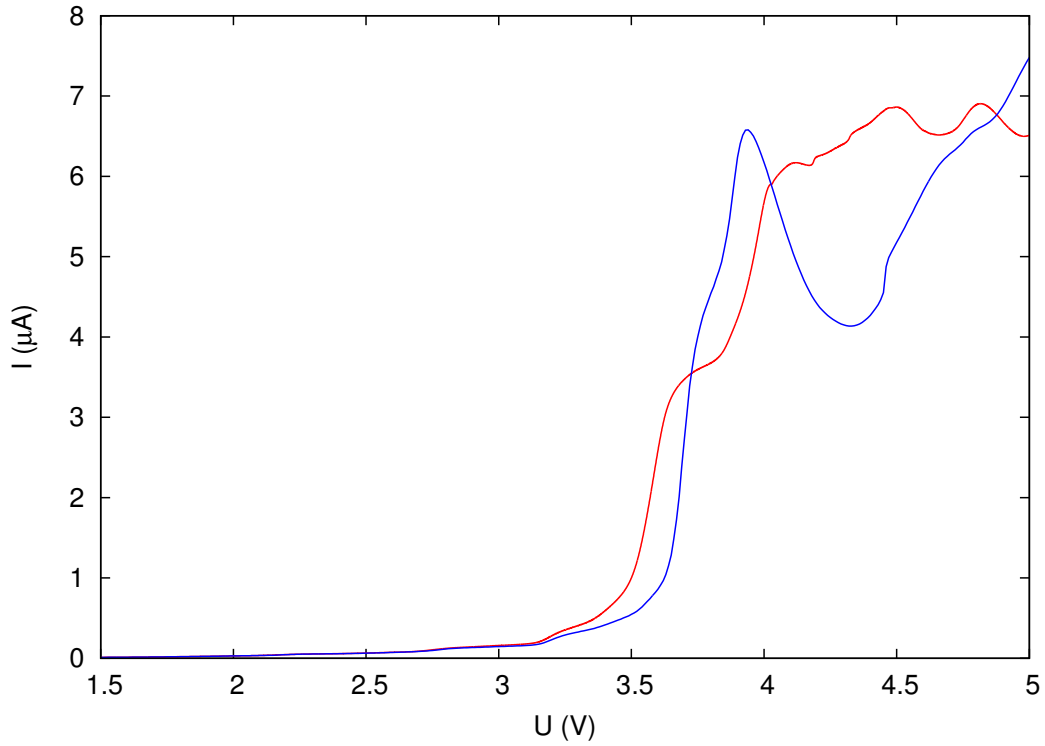

Figure 4.8: Current-voltage characteristic of BDET bound to pyramidal gold contacts. Shown are results of calculations with (blue line) and without (red line) molecular vibrations. Only the non-zero part of the voltage range is shown.

vibrational coupling results in a quenching of the NDR effect, an increased current between 3.10 and 3.72 V and a reduced current for voltages in the range 3.72 - 4.03 V. The 0_0^0 transition due to orbital B causes a step around 3.5 V, while the step at 3.9 V is due to vibrational excitations. The step due to orbital A is seen at 4.18 V.

The increased current is due to the fact that upon interaction with vibrations the resonance peaks are shifted to higher energies and thus enter the voltage window at lower voltage. If the voltage window is large enough to comprise all inelastic peaks, the difference in current vanishes. The smaller current and the vibrational substructures are a result of the splitting of each electronic resonance into several vibronic resonances (cf. Fig. 4.7), which contribute with different weights (determined by the respective Franck-Condon factors) to the transmission. In contrast to the purely electronic case, the

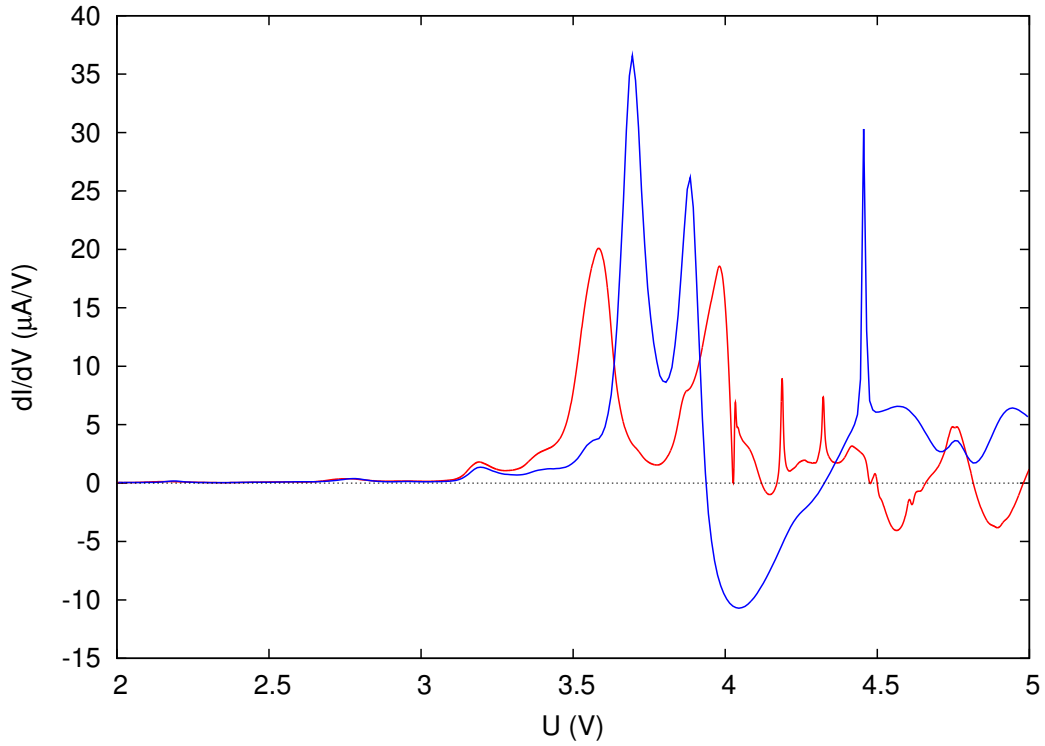

Figure 4.9: Purely electronic (blue line) and vibronic (red line) conductance of BDET.

current thus increases in several steps. This effect is well known from previous model studies [63, 64].

Fig. 4.9 shows the differential conductance, obtained by numerical differentiation of the curves in Fig. 4.8. Overall the differential conductance reflects the transmission behavior of the junction, however, it incorporates its voltage dependence. In the purely electronic conductance this manifests itself in the splitting of the peak due to state B as well as the negative differential resistance between 4 and 4.3 V. At 4.5 V a narrow resonance due to state A can be seen.

The vibrational structures are even more pronounced if the conductance (red line in Fig. 4.9) is considered instead of the zero-voltage transmission. Orbital B causes the first large peak at 3.58 V, without vibrational excitations, while at 3.98 V the $(\mathrm{d})^1_0$-transition can be observed. There are several narrow features due to orbital A, that could not be seen in the zero-voltage transmission. Besides the peak due to the 0^0_0 transition at 4.17 V, we see the

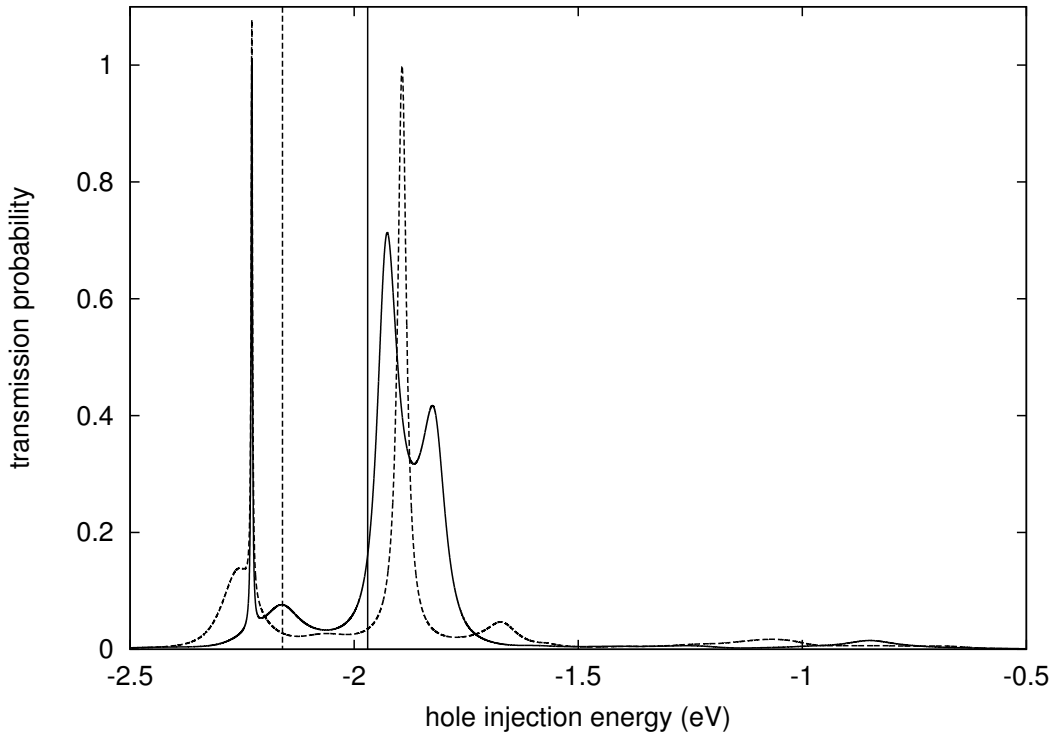

Figure 4.10: Purely electronic transmission of BDET at 3.94 V (solid line) and at 4.32 V (dashed line). The two vertical lines indicate the respective lower integration boundaries.

$(a)_0^1$ transition at 4.32 V.

The vibronic differential conductance curve shows a small negative differential resistance around 4.15 V and two additional negative regions from 4.50 to 4.66 V and from 4.81 to 4.98 V, which do not exist in the purely electronic differential conductance.

The negative differential resistance in the current and conductance curve can be understood from Fig. 4.10, where we compare the transmission function at 3.94 V (the local maximum in the I-V curve) to the transmission function at 4.32 V (the local minimum in the I-V curve). We recall that the current is given by the energy-integral of the transmission function (Sec. 4.1.4) and thus corresponds to the 'area below the transmission curve'. The peak caused by orbital B in the 4.32 V curve is much thinner than the corresponding peak in the 3.94 V curve. Although the current in the former case corresponds to the integral with lower boundary -2.16 (see solid vertical line in

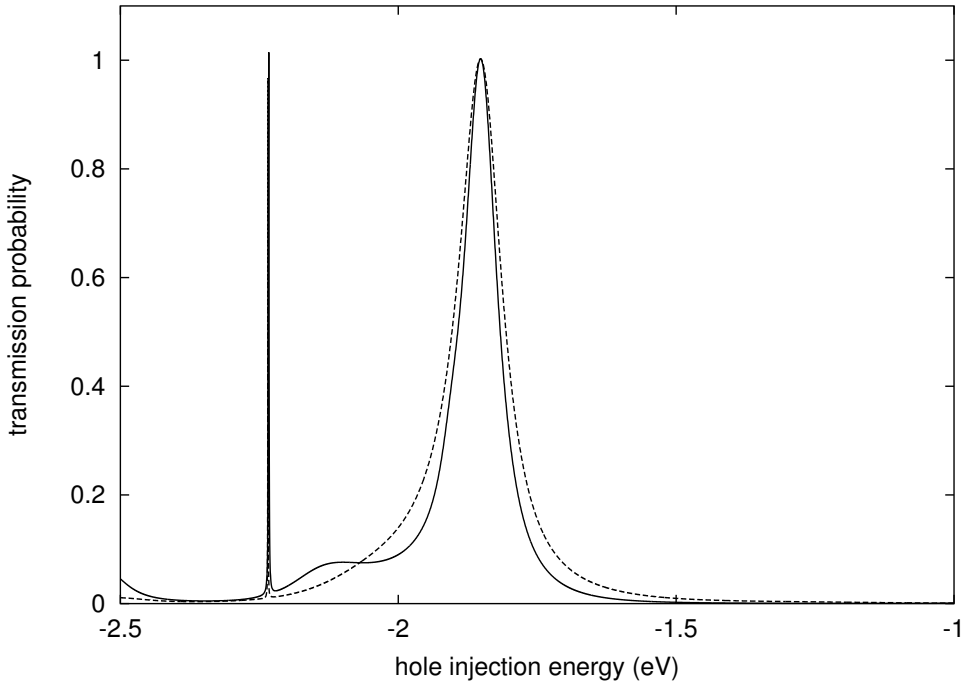

Figure 4.11: Purely electronic zero-voltage transmission of BDET employing a four layer (dashed line) and a five layer (solid line) gold contact.

Fig. 4.10) and in the latter case the integral is taken only to -1.97 (dashed vertical line), the area under the '4.32 V'-transmission-curve is much smaller, which explains the NDR in the current-voltage characteristic and conductance.

Our results show, that neither the peak position nor the peak width change systematically with increasing voltage. Therefore, NDR phenomena cannot be predicted. It should be emphasized that this NDR effect can only be described if the energy and voltage dependence of the self-energies is taken into account and will be missed within the often used wide-band approximation, where $\Gamma(E)$ is assumed to be independent of energy and, therefore, $\Delta = 0$.

Finally, we consider the influence of the size of the gold cluster on the conductance properties of the molecular junction. All results discussed so far employed a four layer gold cluster. Fig. 4.11 shows a comparison of the zero-voltage transmission functions of a system with a four layer and a system with a five layer gold cluster. They agreed very well after taking into account the different Fermi levels and different shifts of the localized molecular states after

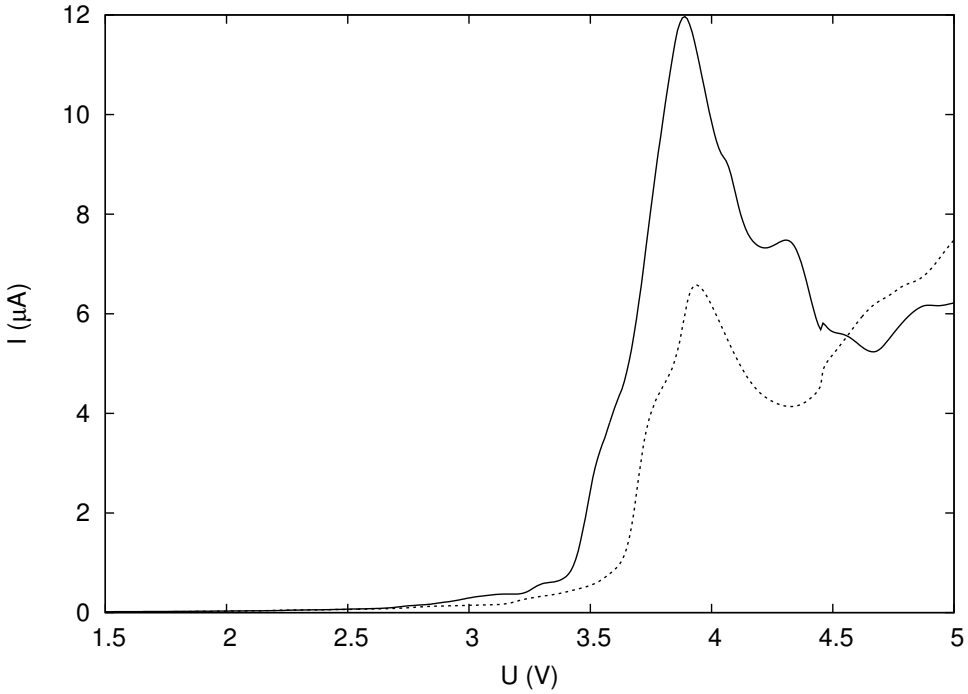

Figure 4.12: Current-voltage characteristic of the BDET junction employing a four layer (dashed line) and a five layer (solid line) gold contact.

projection. However, the differences in the transmission functions increase, if they are regarded at larger voltages. Consequently, the I-V characteristics of both junctions differ significantly, as shown in Fig. 4.12. In particular, the maximum current of the junction with the five layer contact is almost twice as large, as the maximum current of the junction with the four layer contact.

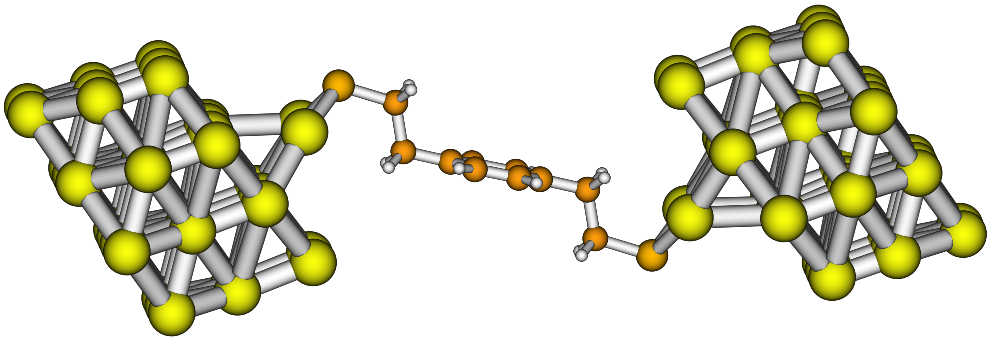

Figure 4.13: The extended molecule of a BDET-junction with two cuboid-shaped gold clusters consisting of 38 gold atoms.

4.2.3 BDET between cuboid-shaped gold clusters

In order to investigate the influence of the gold-cluster geometry on the transport features, we did studies with the same molecule (BDET) clamped between two gold-clusters of a cuboid shape. To build this geometry, we started from the optimized 2-layer system mentioned in Sec. 3.4. Next, the number of gold atoms in the second layer was increased from 5 to 12, and two more (111) layers also consisting of 12 gold atoms were added, resulting in a metal cluster of 38 gold atoms on each side (cf. Fig. 4.13). For better comparison with the above results, the same value was used for the Fermi energy (ϵ_f=-5.15 eV). We note that, because of the strong voltage dependence of the transmission function, different choices of the Fermi energy may lead to I-V characteristics that differ significantly. The chosen normal modes and projected molecular states are similar to those in Fig. 4.6. The charge of the molecular unit for BDET between cuboids is - 0.053 e, which is twice as much as in the system with the pyramidal contacts.

Fig. 4.14 shows the zero-voltage transmission probability as a function of the hole energy of this system. A large difference, with respect to the purely electronic transmission curve of the system with the pyramidal gold contacts, is that the resonance due to state B is split into three peaks at -1.71, -1.79 and -1.95 eV, while the eigenenergy of that peak lies 1.75 eV below the Fermi energy. This is caused by the electrode-mediated interaction of state B with both lower and higher lying states, which seems to be more pronounced using this gold-cluster geometry. There is a small broad peak at +0.39 eV due to two sulfur p-orbitals, which is not affected by vibronic coupling, as the included normal modes show no motions of the sulfur atoms. At -2.17 eV there is a narrow peak due to state A, which is located only 0.01 eV below

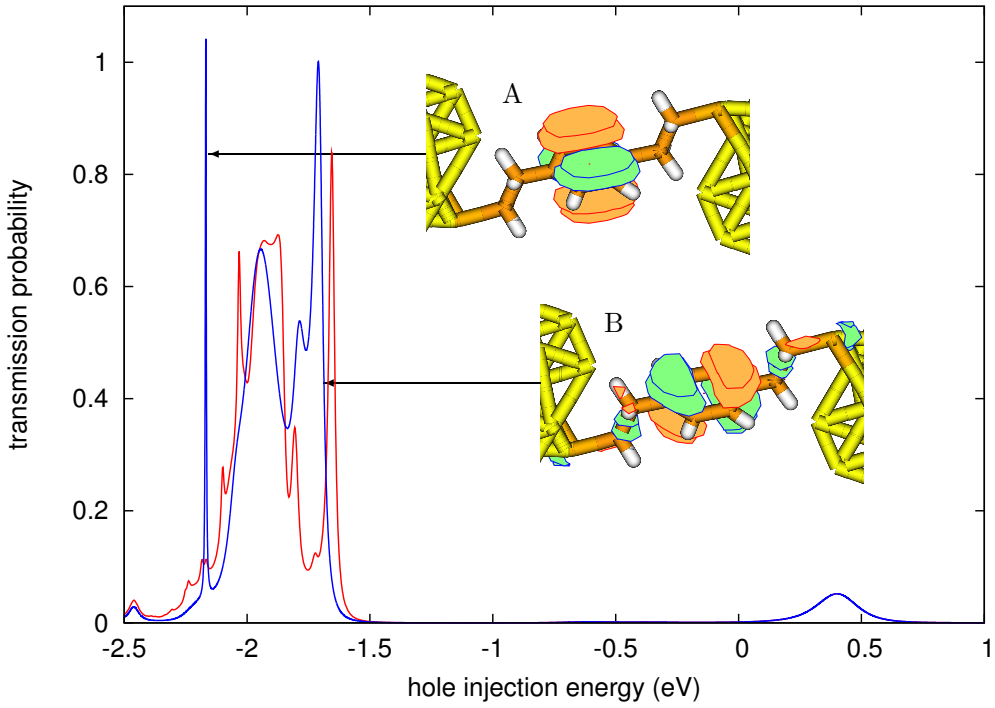

Figure 4.14: Purely electronic (blue line) and vibronic (red line) total transmission probability through a BDET molecular junction with a cuboid-shaped contact geometry at zero voltage as a function of the initial energy of the hole (relative to the Fermi energy). The two orbitals, denoted A and B, dominate the transmittance at the indicated peaks. Only the relevant part of the energy interval [-2.5:+2.5], corresponding to a voltage window of 5 V, is shown.

the eigenenergy of that orbital after projection. The coupling of states A and B to the contacts is of comparable size as in the pyramidal gold geometry: $\Gamma_{AA}(-2.17) = 4.0 \cdot 10^{-4}\,\mathrm{eV}$ (corresponding to a lifetime of $\tau = 1646\,\mathrm{fs}$), $\Gamma_{BB}(-1.98) = 6.5 \cdot 10^{-2}\,\mathrm{eV}$ ($\tau = 10\,\mathrm{fs}$), and $\Gamma_{BB}(-1.71) = 1.1 \cdot 10^{-1}\,\mathrm{eV}$ ($\tau = 6\,\mathrm{fs}$).

In the transmission function based on a vibronic calculation the thin peak due to state B is shifted to higher energies by 0.05 eV and shows peaks at -1.72, -1.81, and -1.87 eV due to modes (a), (b), and (d) (cf. Fig. 4.6). The broad peak at -1.98 eV and the small peak at -1.80 eV due to state B are not significantly affected by vibronic coupling. In this system also the 0_0^0-transition and vibrational progressions of the peak due to state A are visible. There are no accidental coincidences with transmission features of

	ω (cm^{-1})	T (fs)	$\kappa^{(A)}$ (meV)	$\kappa^{(B)}$ (meV)
(a)	545.38	61	76	21
(b)	1195.46	28	51	68
(c)	1229.71	27	108	46
(d)	1674.61	20	134	163

Table 4.3: Frequencies, periods (T), and vibronic coupling parameters corresponding to the two orbitals (A,B) and the four most important vibrational modes of BDET between cuboid-shaped gold contacts.

other states, as there were in the system with the pyramidal contact geometry. The 0_0^0-line due to state A appears at -2.03 eV and the $(m)_0^1$ transition peaks can be seen at -2.10, -2.17, -2.18, and -2.24 eV and are caused by normal modes (a), (b), (c) and (d), respectively. As the vibronic coupling of mode (a) (cf. Tab. 4.3) is almost equal in both the pyramidal and the cuboid system, structures due to this mode can here only be seen because of smaller electronic coupling.

Up to 3 V the features in the current-voltage characteristic (Fig. 4.15) arise from orbitals localized on the sulfur atoms themselves, or from their interaction with orbital B. There is a rise in the purely electronic current due to state B, which reaches a first plateau at 3.66 V and rises again until it reaches a maximum at 3.77 V. This is due to the threefold peak structure of the resonance due to this state. The following NDR is again due to decreasing peak width and height at higher voltages. At 4.00 V a minimum is reached, then the current rises again, due to increasing peak height and width of the transmission features of state B until at 4.21 V for a small range the slope increases again, indicating the contribution of state A.

When including vibronic coupling into the current calculation, the rise due to state B occurs at smaller voltages than in the purely electronic curve, as the 0_0^0 transition enters the voltage window earlier than the purely electronic resonance peak. The current reaches a maximum at 3.90 V thereby exceeding the maximum current without vibrations by 6.72 μA and then decreases for the rest of the voltage window. The contributions of state B are too small to be seen distinctly. In this case the NDR is not quenched by the inclusion of vibronic coupling, probably due to larger electronic coupling.

The question arises how the vibronic current can be larger than that without vibrations? The vibronic coupling increases the transmission probability by shifting and splitting resonance peaks. Thus, they may reach positions where the electronic coupling to the contacts, but also to other molecular states via the contacts, is significantly different from the electronic interac-

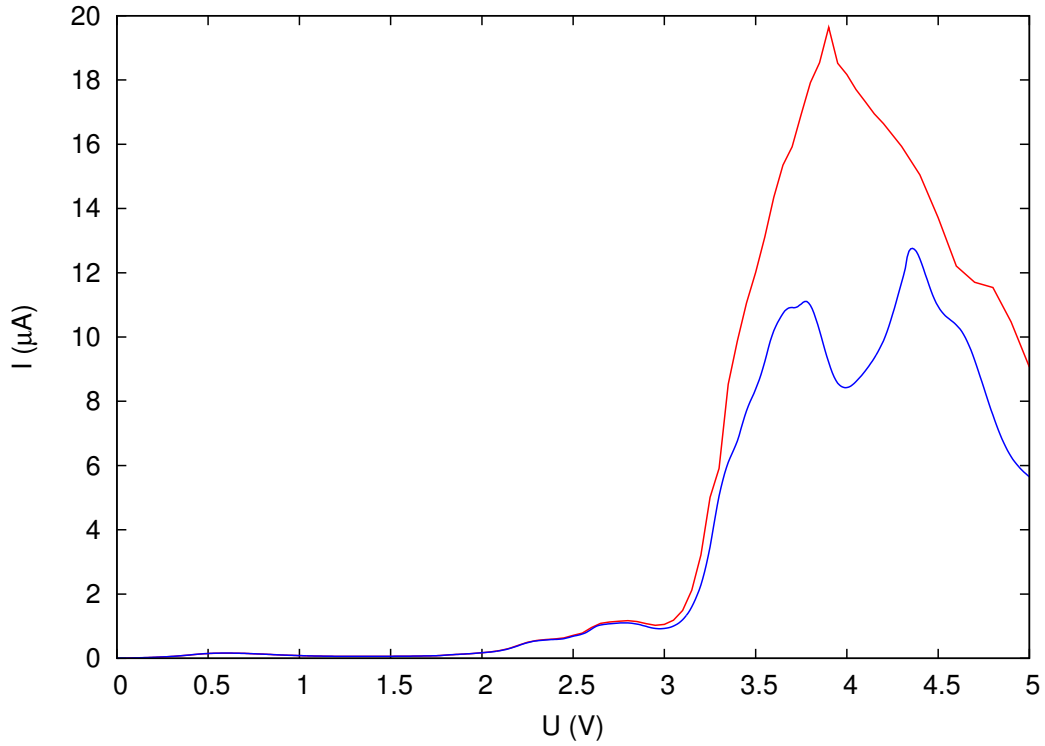

Figure 4.15: Current-voltage characteristic of BDET bound to cuboid-shaped gold contacts. Shown are results of calculations with (red line) and without (blue line) molecular vibrations. Only the part including transport due to state A and B is shown.

tion at the initial position. Consequently, the transmission probability may change and in this case increases.

To conclude this subsection we note that the geometry of the gold contact does have a significant influence on the transport characteristics of the molecular junction. Both the transmission and the current are influenced by the obviously different coupling of molecular state B to the contact, while state A is, at least in transmission, not much affected. The current is larger by about a factor of two for the system with the cuboid gold contacts.

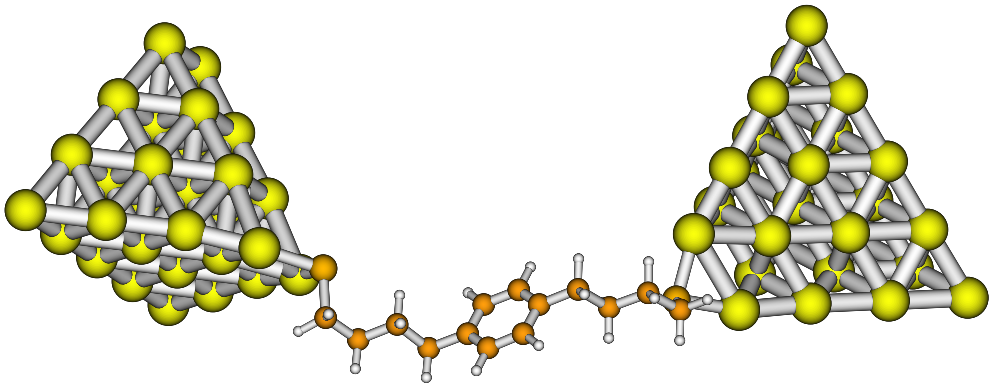

Figure 4.16: BDBT between two pyramidal gold clusters consisting of 30 gold atoms.

4.2.4 Benzenedi(butanethiolate)

In order to further reduce the electronic coupling between the benzene-ring and the gold cluster, and thus increase the lifetime of the electron and vibronic effects, a model system with two butyl-bridges, p-benzene-di(butanethiolate) (BDBT) was studied (Fig. 4.16). This system was only investigated with the pyramidal cluster geometry. The transmission function can be well described using only 6 electronic states. These comprise two states similar to states A and B in BDET, and four sulfur p-orbitals.

BDBT has 54 totally symmetric normal modes. Those four with the largest effective vibronic coupling (Fig. 4.17) were chosen to be included in the calculation. They are similar to the normal modes in BDET: a C-C-C bending mode (a), a C-C-H bending mode (b), a combined C-C-C/C-C-H bending mode, and a combined C-C stretching/C-C-H bending mode (d).

The projected orbitals A and B are similar to the HOMO-3 and HOMO-2 of the isolated molecule and lie -1.55 and -1.17 eV below the Fermi energy, respectively. The Fermi energy in this system was approximately -5.16 eV. After projection the states A and B have energies -1.77 and -1.38 eV, respectively, which means that both states were shifted to lower energies. The HOMO-1 and HOMO of the isolated molecule are quasi-degenerate, mostly localized on the sulfur atoms and resemble two of the projected sulfur orbitals (those at larger energy). The charge of the molecular unit, as determined by a population analysis is - 0.041 e.

The purely electronic zero-voltage transmission, depicted in Fig. 4.18, shows two narrow peaks at -1.78 and -1.39 eV. These peaks are due to states A and B, which couple to gold with coupling strengths of $\Gamma_{AA}(-1.78) =$

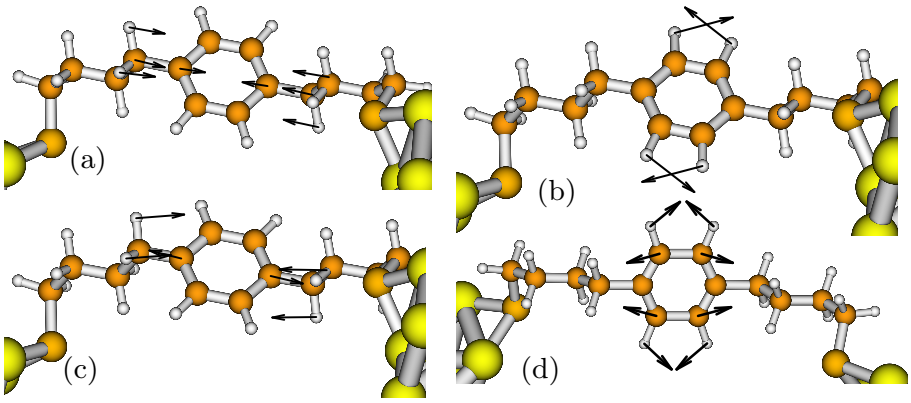

Figure 4.17: Normal modes of BDBT included in the calculation.

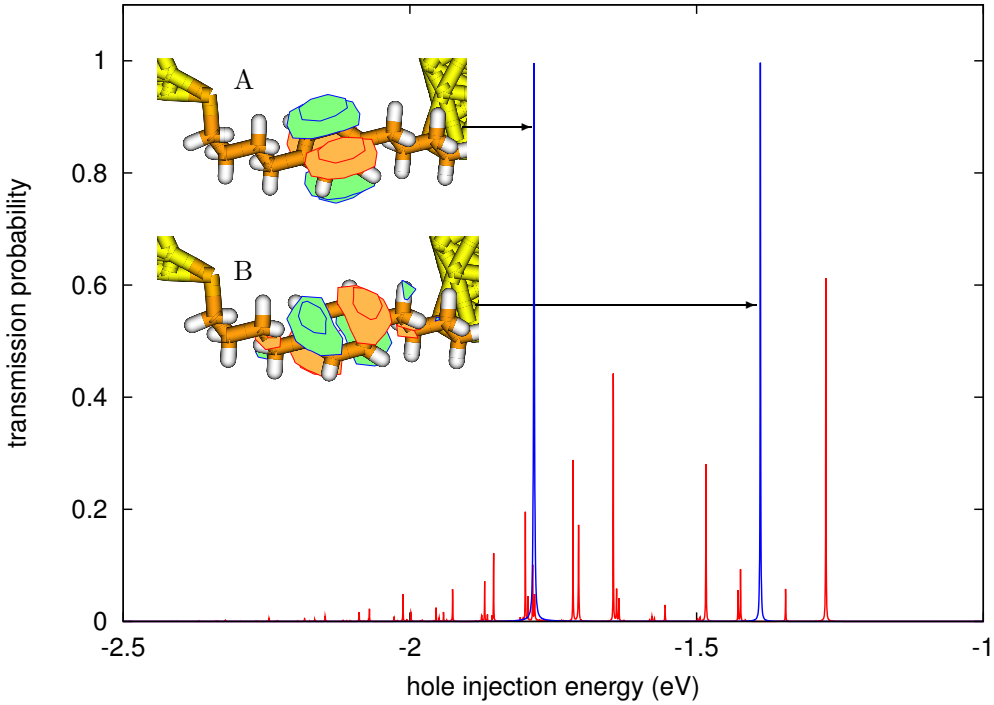

Figure 4.18: Purely electronic (blue line) and vibronic (red line) total transmission probability through a BDBT molecular junction at zero voltage as a function of the initial energy of the hole (relative to the Fermi energy). The two orbitals, denoted A and B, dominate the transmittance at the indicated peaks. Only the relevant part of the energy interval [-2.5:+2.5], corresponding to a voltage window of 5 V, is shown.

	ω (cm^{-1})	T (fs)	$\kappa^{(A)}$ (meV)	$\kappa^{(B)}$ (meV)
(a)	566.12	59	69	29
(b)	1198.40	28	52	73
(c)	1232.90	27	114	56
(d)	1676.10	20	132	170

Table 4.4: Frequencies and periods (T) of the four most important vibrational modes of BDBT as well as gradients of these modes for the two orbitals (A,B) dominating conduction.

$1.0 \cdot 10^{-3}$ eV ($\tau = 659$ fs) and $\Gamma_{BB}(-1.39) = 5.4 \cdot 10^{-4}$ eV ($\tau = 1220$ fs), respectively. Due to the small coupling, these states exhibit negligible level shift.

If vibronic coupling is included, the peak due to state B becomes shifted to -1.27 eV, while the 0_0^0 transition of the peak due to orbital A appears at -1.65 eV. Both peaks show pronounced vibrational progressions, whose positions are arranged in Tab. 4.5. The individual peak heights correspond to the respective Franck-Condon factors (vibronic coupling parameters). For example, the peak due to single excitation of mode (d) in orbital B is larger than all the other single excitation peaks. Also, for orbital B the $(c)_0^1$ transition of mode is much smaller than the corresponding transition of mode (b). For orbital A this situation is reversed.

orbital A	mode (a)	mode (b)	mode (c)	mode (d)
$(m)_0^1$	-1.72		-1.80	-1.85
$(m)_0^2$	-1.79		-1.93	-2.07
orbital B	mode (a)	mode (b)	mode (c)	mode (d)
$(m)_0^1$	-1.35	-1.42	-1.43	-1.48
$(m)_0^2$		-1.56		-1.71

Table 4.5: The positions (in eV) of the vibronic transitions in the transmission function of BDBT. Blank entries correspond to transitions that can not be seen, because of too small vibronic coupling.

The purely electronic current curve (blue line in Fig. 4.19) shows a small rise up to 2.0 V and a first step at 2.06 V, which would not be expected from the zero-voltage transmission. Both features are due to the sulfur p-states, which cause a small, but very broad peak around the Fermi level and a small, narrow peak at -1.07 eV, which can be seen in the transmission probability calculated at 2 V (inset in Fig. 4.20), but not in the zero-voltage transmission.

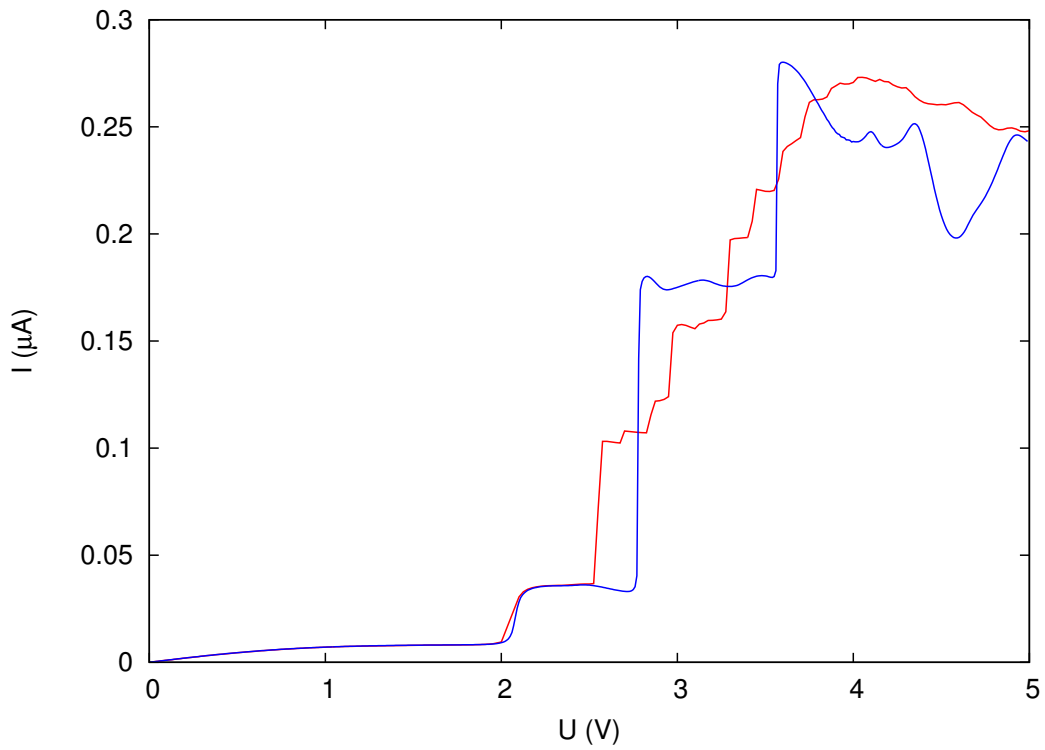

Figure 4.19: Current-voltage characteristic of BDBT. Shown are results of calculations with (red line) and without (blue line) molecular vibrations.

When comparing the transmission probabilities at equilibrium and at 2 V, it can also be seen that the height of the two peaks caused by orbitals A and B is smaller at 2 V than at 0 V.

In the I-V curve two steps follow at 2.76 and 3.56 V, which are due to orbitals B and A, respectively. As in the other model systems, NDR is visible after the last step, which is again due to decreasing height of the peaks due to states B and A with further increasing voltage. In the vibronic current the step at 2.06 V is also present, confirming that this step must be due to orbitals that do not couple to vibrations. Furthermore, a number of additional steplike structures appear which can be assigned to excitation of the different vibrational modes in states A and B. The most pronounced features are analyzed in Table 4.6. The NDR following the last step still exists but is significantly smaller compared to the purely electronic case.

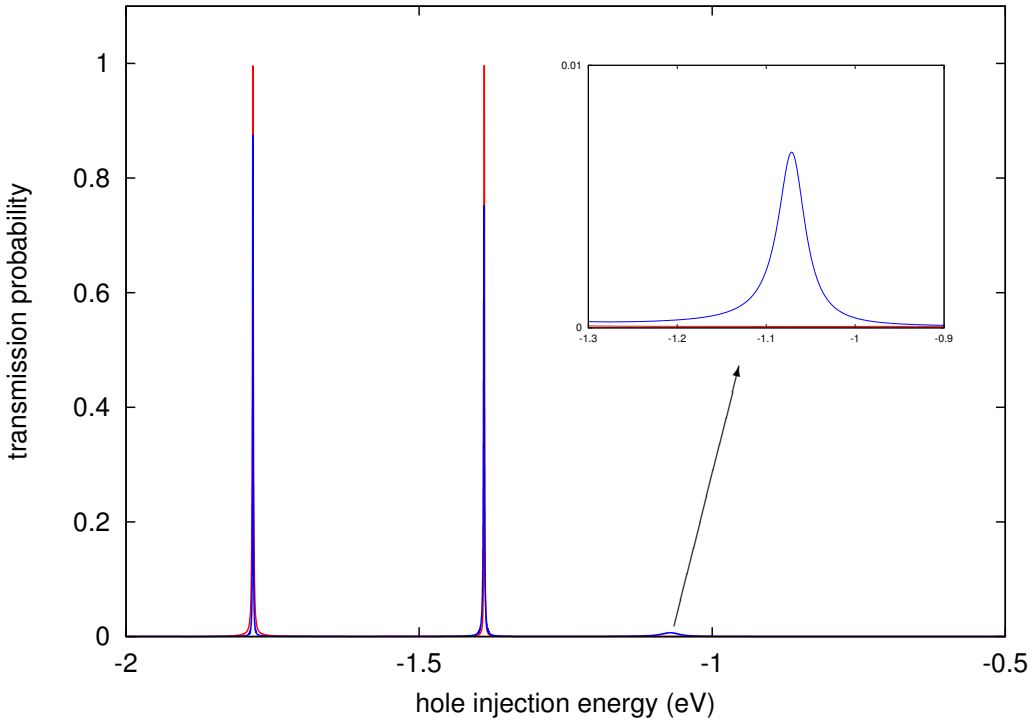

Figure 4.20: Purely electronic transmission probability of BDBT at equilibrium (red line) and at 2 V (blue line).

	0_0^0	$(a)_0^1$	$(b)_0^1$	$(c)_0^1$	$(d)_0^1$	$(d)_0^2$
orbital A	3.27	3.42	3.57	3.57	3.73	
orbital B	2.55	2.68	2.85	2.85	2.95	3.42

Table 4.6: The positions (in V) of the vibronic transitions in the I-V curve of BDBT. Blank entries correspond to transitions that can not be seen, because of too small vibronic coupling.

4.3 Surface self-energy models

As was discussed in Sec. 3.2 and Appendix A, the influence of the semi-infinite solid on the contacts is described by the surface self-energy (of a (111) gold surface). In this section we will discuss the influence of different surface self-energy models on the transport characteristics of molecular junctions. As an example we will consider transmission through the BDT junction presented in Sec. 4.2.1 without vibronic interactions.

In a frequently employed model for the surface self-energy Σ^{sf}, a diagonal matrix containing a purely imaginary value σ is added to the diagonal Kohn-Sham matrix elements belonging to the gold atoms of the outermost gold layer (cf. Eq. (3.11)) [65, 37]. In this model we neglect that s-, p-, and d-orbitals might be influenced differently by the interaction with a semi-infinite solid, and coupling elements between orbitals of the same atom but also between different atoms are assumed not be influenced.

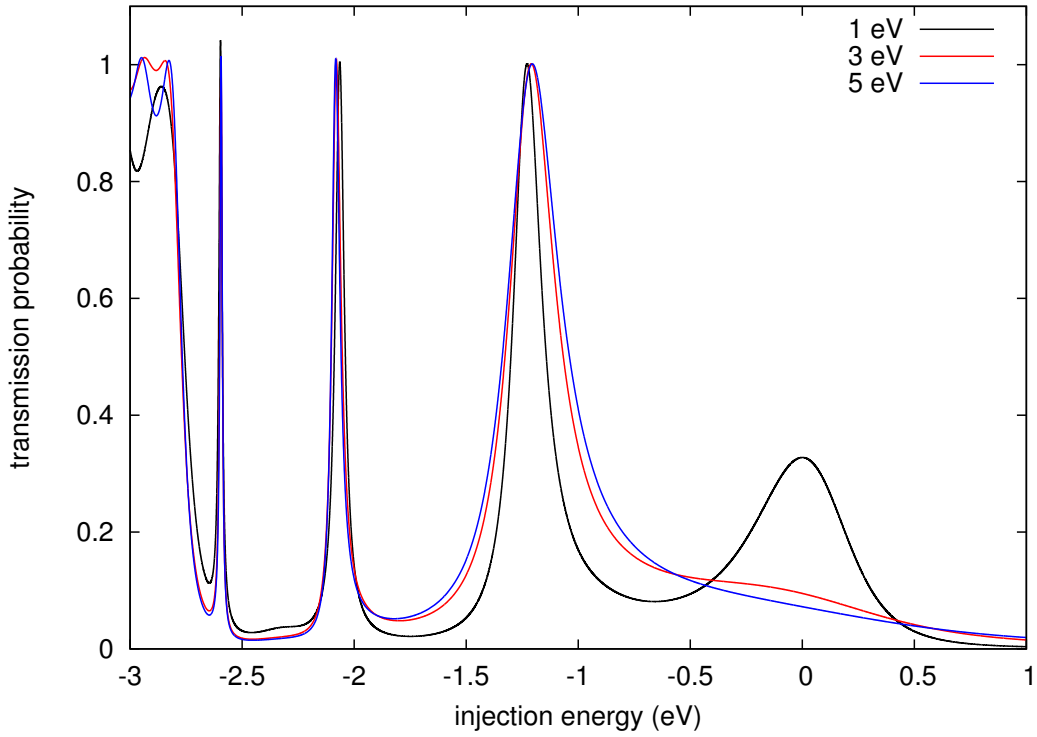

Figure 4.21: The purely electronic transmission probability through BDT, when using σ values of 1 eV (black line), 3 eV (red line), and 5 eV (blue line).

In Fig. 4.21 the purely electronic transmission probability through BDT is shown for three different values of the surface self-energy parameter. It can be seen that the peaks due to states A (-2.61 eV) and B (-2.06 eV) are almost independent of this parameter, while the peak due to orbital C (-1.25 eV) increases in width with increasing self-energy. This is probably due to the smaller electronic coupling of states A and B to the contacts (cf. Sec. 4.2.1). The peak at the Fermi level becomes flatter and vanishes at large self-energy values.

To optimize the value of this self energy parameter, we investigated two linear tight-binding models. These models consisted of a single electronic state on the molecule, which was coupled to an infinite and a finite linear gold chain, respectively. The transmission through the model with the infinite linear gold chain was calculated exactly while an imaginary part was added to the elements of the outer sites of the finite linear gold chain. The transmission through this model system was calculated at different self-energy values. The number that yielded the smallest least-mean-squares error was taken in the calculation of the quantum-chemical system, its value was 0.93 eV. All parameters in the tight-binding model were taken to be similar to the parameters delivered by the quantum chemistry model.

An indication that this single parameter self-energy model is not sufficient, can be deduced from Fig. 4.22, where the purely electronic transmission probability through BDT is shown for the same self-energy value (0.93 eV), but for different locations of the boundary between molecule and contact in the partitioning of the molecular junction.

When separating the extended molecule into molecule and contact part, all gold atoms are allocated to the latter, while all remaining atoms belong to the molecular space. Fig. 4.22 shows data where two or seven gold atoms on both sides of the molecule are additionally included into the molecular space, respectively. It can be seen that the peak around ϵ_f strongly depends on the projection boundary. Its transmission probability rises from 0.37, when using the conventional projection boundary, to 0.63, when including 2x2 gold atoms of the first layer in molecular space, to 0.87, when including both 2x2 gold atoms of the first and 2x5 gold atoms of the second layer in molecular space. The other peaks, which could be assigned uniquely to molecular orbitals, depend only weakly on this projection boundary.

The transmission functions in Fig. 4.22 were calculated including all electronic states in molecular space for comparability. In principle, the transmission features should be independent of the partitioning of the molecular junction.

Another popular surface self-energy model is based on a tight-binding calculation of the semi-infinite gold (111) crystal. This model was employed

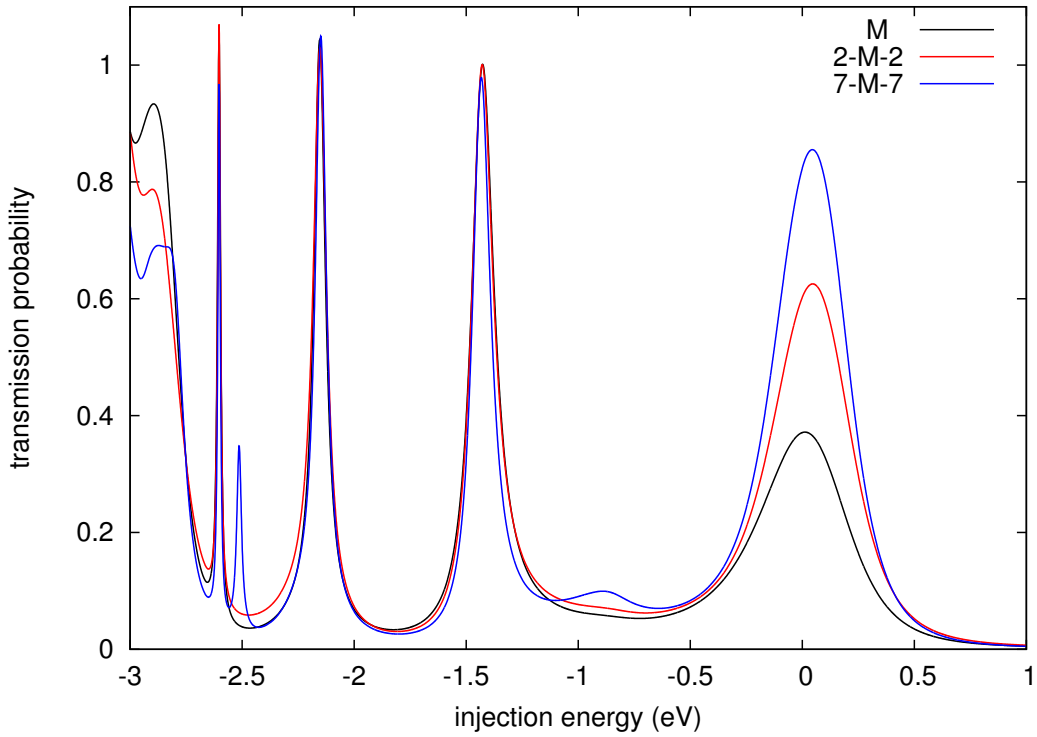

Figure 4.22: The purely electronic transmission probability through BDT. A single imaginary self-energy parameter of 0.93 eV and different partitioning boundary were used: border between S and the two gold atoms of the first layer (black line), border between the first and the second gold layer (red line), and border between the second and the third gold layer (blue line).

in the calculations presented in Sec. 4.2. The self-energy was obtained calculating the surface Green's function [54] for the semi-infinite electrode using a DFT-parameterized tight-binding model for gold. This model neglects self-energy contributions to coupling elements between different gold atoms in the outermost gold layer. The surface self-energy matrix for the second outer gold-layer, was small enough to be neglected.

The transmission probability through BDT for different projection boundaries is shown in Fig. 4.23. The peak at the Fermi level is still present, but its dependence on the projection boundary is much weaker, and the peaks themselves are not as large as in Fig. 4.22. From a transmission probability of 0.23 for the conventional projection boundary, the peak maximum rises to 0.31 for 2x2 additional gold atoms, and 0.35 if 2x7 gold atoms are included

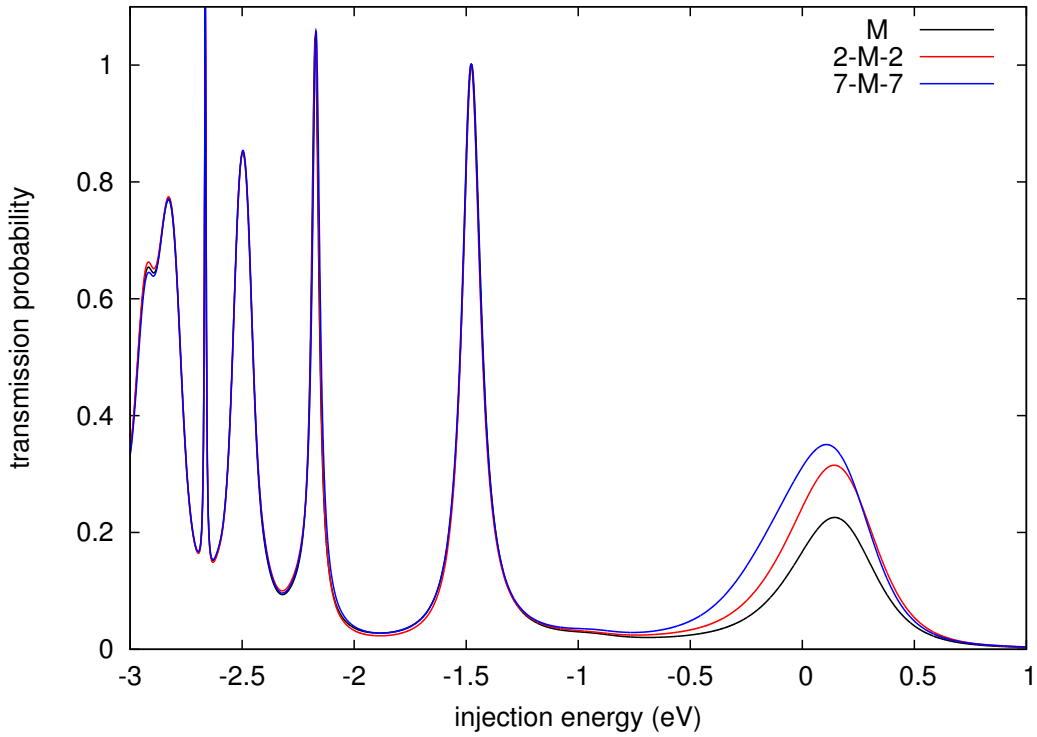

Figure 4.23: The purely electronic transmission probability through BDT, when using different projection boundaries: boundary between S and the two gold atoms of the first layer (black line), boundary between the first and the second gold layer (red line), and boundary between the second and the third gold layer (blue line). The surface self-energy from a tight-binding model of the semi-infinite gold solid was used.

in molecular space. When comparing the remaining features in the transmission functions obtained with the two different surface self-energy models, we notice that the three peaks in Fig. 4.21 are slightly shifted to the left and now appear at -2.67 (orbital A), -2.18 (B), and -1.48 eV (C). An additional peak at -2.50 eV appeared, which is also due to orbital (B), and also the features below -2.70 eV are different for the two employed self-energy models.

We conclude, that the influence of different surface self-energy models on the transmission features through the BDT molecular junction is significant. It leads to a shift and splitting of resonance peaks and strongly determines the intensity of the peak at the Fermi level. When testing the surface self-energy model systems with respect to different projection boundaries, the

tight-binding model gives a significantly better description than the single parameter model.

4.4 Summary

In this chapter we investigated the transport characteristics of molecular junctions using a scattering theory formalism. The central quantity in this approach is the multi-channel transmission probability, from which we obtain the current via a generalized Landauer formula.

We applied the scattering formalism to four different model junctions: Benzenedithiolate, benzenedi(ethanethiolate), and benzenedi(buthanethiolate) with pyramidal gold contacts, as well as benzenedi(ethanethiolate) with cuboid-shaped gold contacts. These three molecules differ in the length of the spacer group that separates the benzene ring from the contacts. Expectedly, the overall current decreased, the longer the spacer group, which is in accord with experimental studies of BDT and benzenedi(methanethiolate) [66]. We found that the transport characteristics around the Fermi energy can be assigned to a small number of molecular orbitals. There is strong interaction between orbitals located on the benzene ring and orbitals located on the sulfur atoms of the thiolate group, which is mediated by the metal contacts. For BDET, we investigated the influence of different gold contact geometries and found that cuboid-shaped and pyramidal gold clusters lead to different transport characteristics of the molecular junction. For all four molecular junctions we observed negative differential resistance, which we attributed to the voltage dependence of the self-energy that describes the effect of the electrodes on the molecule.

The main focus of this chapter, however, was on the investigation of vibronic effects on molecular conductance. The results show that due to electronic-vibrational coupling resonance structures (peaks and steps) are shifted to the extent of the reorganization energy and they are split into several substructures whose individual amplitudes are determined by the respective Franck-Condon factor. We found that several time and energy scales have to be considered simultaneously in order to understand the extent of vibronic coupling. As a rule, vibronic effects increase with increasing vibronic coupling between orbitals and normal mode vibrations and they decrease with decreasing lifetime of the electron (hole) in these orbitals. The latter is determined by electronic coupling between molecular orbitals and electronic states in the electrodes. Furthermore, vibronic effects are more pronounced the larger the lifetime of the electron (hole) on the molecule with respect to the period of the normal mode vibrational. As a result,

vibronic features are less pronounced for BDT than for BDET, and smaller for BDET than for BDBT.

To conclude this chapter we discuss related work. While we used the scattering formalism to describe inelastic transport in the electronically resonant regime, scattering theory can also be used to describe inelastic tunneling in the off-resonant region. To this end, the molecular Green's function, rather than the Hamiltonian, is expanded to first order in the vibronic interaction [67], and the involved matrices are of the dimension of the molecular, electronic subsystem. In contrast to our method, for a given Hamiltonian, this is a perturbative treatment of the vibronic coupling and only single vibrational excitations can be described. Using this technique the experimental spectra in Ref. [32] could be reproduced [68]. Within scattering theory IETS spectra can also be simulated by expanding the system's wavefunctions to first order in the nuclear coordinates [59].

An effect that is closely related to vibrational excitation in molecular junctions is heat generation. Heating of a BDT-junction and a single gold-atom contact due to vibrational excitation was investigated in Ref. [69] using a first-order perturbation expansion in the vibronic coupling within a scattering theory approach. The authors found that much more heat is generated in single atom junctions than in single molecule junctions, as the latter constitute a much larger resistance. Using a similar approach, the same authors demonstrated the dependence of the inelastic, low-voltage conductance on the contact geometry [70] by binding BDT to two gold clusters or a single gold cluster, respectively. Finally, in Ref. [71] a time-dependent scattering approach was used to investigate processes like molecule desorption or molecular reactions in a STM configuration, where the final scattering state is non-bonded.

Chapter 5

Density Matrix Theory

Density Matrix Theory is a formulation of quantum mechanics, in which a quantum mechanical system is not described by a single wavefunction, but by a density operator. This density operator is, in general, a sum of projection operators onto different quantum mechanical states, weighted by the probability with which the state is occupied by the system [72],

$$\hat{R} = \sum_s w_s \left|\Psi_s\right\rangle\left\langle\Psi_s\right| \ . \tag{5.1}$$

If all but one w_s are zero, the system is in a pure state, otherwise it is in a mixed state.

In this chapter we will present a transport formalism that is based on the density matrix reduced onto the molecular space. In the first part, we derive the rate equations for the transitions from electrode to molecule and vice versa, and we deduce an expression for the current. In the second part, the density matrix formalism is applied to the BDBT molecular junction.

5.1 Density Matrix Formalism

5.1.1 Density Operator

In the framework of density matrices the expectation value of the current through electrode α, α being either L or R, is given by

$$I_\alpha = e\left\langle \hat{I}_\alpha(t)\right\rangle = e\,\mathrm{tr}_{B+S}\left\{\hat{R}(t)\hat{I}_\alpha\right\} \ , \tag{5.2}$$

where $\hat{R}(t)$ is the density operator of the total system, $\hat{I}$ is the current operator, and the trace is taken over all degrees of freedom (DOF), i.e. electronic

and vibrational states of the molecule (S) and the bath (B). In the applications considered here, the bath corresponds to the electronic states in the left and right electrodes ($B = L + R$).

The current operator is the time derivative of the number operator $\hat{N}$ of the respective electrode,

$$\hat{I}_\alpha = \frac{d\hat{N}_\alpha}{dt} = \frac{i}{\hbar}\left[H, \hat{N}_\alpha\right], \quad \hat{N}_\alpha = 2\sum_{k\in\alpha} c_k^\dagger c_k \ , \tag{5.3}$$

where the factor two accounts for spin degeneracy. Taking the time derivative results in the evaluation of the commutator of the number operator with the Hamiltonian of the total system.

The time-evolution of the total density operator is given by the Liouville-von Neumann equation

$$\frac{\partial}{\partial t}\hat{R}(t) = \dot{R}(t) = -\frac{i}{\hbar}\left[H, \hat{R}(t)\right] = -i\mathcal{L}\hat{R}(t) \ ,$$

where Liouville-space notation was introduced, $\mathcal{L}\hat{O} = \frac{1}{\hbar}[H, \hat{O}]$, with $\hat{O}$ being some arbitrary operator.

As the density operator of the total molecular junction, $\hat{R}(t)$, is a considerably large quantity, we will express the current and the time-evolution in terms of the reduced density operator $\rho(t)$,

$$\rho(t) = \mathrm{tr}_B\left\{\hat{R}(t)\right\} \ ,$$

where the trace is taken over the bath (i.e. the electrodes) DOF.

5.1.2 Derivation of the Equation of Motion

The time-evolution of the reduced density operator is given by [73]

$$\dot{\rho}(t) = \dot{\rho}(t)^{coh} + \dot{\rho}(t)^{diss} = -\frac{i}{\hbar}\left[H_S, \rho(t)\right] - \frac{i}{\hbar}\mathrm{tr}_B\left\{\left[V, \hat{R}(t)\right]\right\} \ , \tag{5.4}$$

where the first term describes the coherent evolution of ρ and the second term describes its dissipation caused by the interaction (V) of the molecular system with the contacts.

In order to remove the total density operator in the dissipation term and to obtain a closed equation for $\rho(t)$, projection operators P and Q are introduced. In contrast to the projection operators introduced in the previous

chapters, which were defined in Hilbert space, P and Q here are defined in Liouville space. P is given by its effect on an arbitrary operator $\hat{O}$,

$$P\,\hat{O} = B_{eq}\,\mathrm{tr}_B\left\{\hat{O}\right\}\ . \tag{5.5}$$

For $\hat{R}(t)$ this gives

$$P\hat{R}(t) = B_{eq}\,\rho(t), \tag{5.6}$$

i.e. P factorizes the total density operator in a density operator of the electrodes at equilibrium and the reduced density operator, $\rho(t)$. The equilibrium density operator of the electrodes is ($\beta = (k\,T)^{-1}$)

$$B_{eq} = Z_B^{-1}\exp\left\{-\beta\sum_{k\in\alpha}(E_k-\mu_\alpha)c_k^\dagger c_k\right\}\ ,$$

where Z_B is the partition function of the electrodes in the grand-canonical ensemble,

$$Z_B = \mathrm{tr}_B\left[\exp\left\{-\beta\sum_{k\in\alpha}(E_k-\mu_\alpha)c_k^\dagger c_k\right\}\right]\ .$$

Introducing the sum of projection operators, $P+Q=1$, into the dissipative part of Eq. (5.4) gives

$$\begin{aligned}\dot{\rho}(t)^{diss} &= -\frac{i}{\hbar}\mathrm{tr}_B\left\{\left[V, P\hat{R}(t)+Q\hat{R}(t)\right]\right\}\\ &= -\frac{i}{\hbar}\mathrm{tr}_B\left\{[V,B_{eq}\rho(t)]+\left[V,Q\hat{R}(t)\right]\right\}\quad .\end{aligned} \tag{5.7}$$

The first commutator vanishes upon taking the trace, because the interaction Hamiltonian V is linear in the electrode operators. Using Liouville-space notation the right part of Eq. (5.7) can be written more compactly

$$\dot{\rho}(t)^{diss} = -i\,\mathrm{tr}_B\left\{\mathcal{L}_V Q\hat{R}(t)\right\}\ . \tag{5.8}$$

where $\mathcal{L}_V\hat{O} = \frac{1}{\hbar}[V,\hat{O}]$.

In order to evaluate this term, the equation of motion (EOM) for $\hat{R}(t)$ is rewritten,

$$\begin{aligned}\frac{\partial}{\partial t}\hat{R}(t) &= -i\mathcal{L}\hat{R}(t) = -i\mathcal{L}Q\hat{R}(t) - i\mathcal{L}P\hat{R}(t)\\ &= -i\mathcal{L}Q\hat{R}(t) - i\mathcal{L}B_{eq}\rho(t)\ .\end{aligned}$$

This is a first order inhomogeneous differential equation that can be formally solved to give

$$\hat{R}(t) = e^{-i\mathcal{L}Q(t-t_0)}\hat{R}(t_0) - i\int_{t_0}^{t} \mathrm{d}t_1 e^{-i\mathcal{L}Q(t-t_1)}\mathcal{L}B_{eq}\rho(t_1) \ . \tag{5.9}$$

The first term of Eq. (5.9), when multiplied by Q, vanishes, if at time t_0 there are no initial correlations between the electrodes and the molecule. Inserting Eq. (5.9) into Eq. (5.8) gives

$$\begin{aligned}
\dot{\rho}(t)^{diss} &= -\int_{t_0}^{t} \mathrm{d}t_1 \mathrm{tr}_B \left\{\mathcal{L}_V Q e^{-i\mathcal{L}Q(t-t_1)}\mathcal{L}B_{eq}\rho(t_1)\right\} \\
&= -\int_{t_0}^{t} \mathrm{d}t_1 \mathrm{tr}_B \left\{\mathcal{L}_V e^{-iQ\mathcal{L}(t-t_1)}Q\mathcal{L}B_{eq}\rho(t_1)\right\} \\
&= -\int_{t_0}^{t} \mathrm{d}t_1 \mathrm{tr}_B \left\{\mathcal{L}_V e^{-iQ\mathcal{L}(t-t_1)}(1-P)\left(\mathcal{L}_S+\mathcal{L}_V+\mathcal{L}_B\right)B_{eq}\rho(t_1)\right\} \ .
\end{aligned}$$

Of the term $(1-P)\left(\mathcal{L}_S+\mathcal{L}_V+\mathcal{L}_B\right)B_{eq}\rho(t_1)$ all terms except $\mathcal{L}_V B_{eq}\rho(t_1)$ vanish. If the treatment is restricted to second (i.e. first non-vanishing) order perturbation theory in the electrode-molecule interaction (V), the Liouville operator in the exponent $\mathcal{L} = \mathcal{L}_S+\mathcal{L}_V+\mathcal{L}_B$ is approximated by $\mathcal{L} \approx \mathcal{L}_S+\mathcal{L}_B$. In the exponent it can then also be shown, that the term including P vanishes, which gives

$$\begin{aligned}
\dot{\rho}(t)^{diss} &= -\int_{t_0}^{t} \mathrm{d}t_1 \mathrm{tr}_B \left\{\mathcal{L}_V e^{-i(1-P)(\mathcal{L}_S+\mathcal{L}_B)(t-t_1)}\mathcal{L}_V B_{eq}\rho(t_1)\right\} \\
&= -\int_{t_0}^{t} \mathrm{d}t_1 \mathrm{tr}_B \left\{\mathcal{L}_V e^{-i(\mathcal{L}_S+\mathcal{L}_B)(t-t_1)}\mathcal{L}_V B_{eq}\rho(t_1)\right\} \\
&= -\int_{t_0}^{t} \mathrm{d}t_1 \mathrm{tr}_B \left\{\mathcal{L}_V\mathcal{L}_V(t-t_1)B_{eq}e^{-\frac{i}{\hbar}H_S(t-t_1)}\rho(t_1)e^{+\frac{i}{\hbar}H_S(t-t_1)}\right\} . \qquad (5.10)
\end{aligned}$$

Here it was used that B_{eq} commutes with both $\mathcal{L}_S$ and $\mathcal{L}_B$, while $\rho(t)$ only commutes with H_B, and the time-dependence of $V(t-t_1)$ was defined as

$$V(t-t_1) = e^{-\frac{i}{\hbar}(H_S+H_B)(t-t_1)}Ve^{+\frac{i}{\hbar}(H_S+H_B)(t-t_1)} \ .$$

The EOM for $\rho(t)$ in the form of Eq. (5.10) corresponds to an integro-differential equation, that is referred to as the 'second order Born approximation'. To obtain a simple differential equation, the integration variable is substituted by $\tau = t - t_1$

$$\dot{\rho}(t)^{diss} = -\int_{0}^{t-t_0} \mathrm{d}\tau \ \mathrm{tr}_B \left\{\mathcal{L}_V\mathcal{L}_V(\tau)B_{eq}e^{-\frac{i}{\hbar}H_S\tau}\rho(t-\tau)e^{+\frac{i}{\hbar}H_S\tau}\right\} \ ,$$

and the Markov-approximation

$$e^{-\frac{i}{\hbar}H_S\tau}\rho(t-\tau)e^{+\frac{i}{\hbar}H_S\tau} \approx \rho(t) \ ,$$

is invoked. Physically the Markov approximation implies that memory effects are neglected, i.e. the system at time t is not influenced by its evolution at times earlier than t. The EOM for the reduced density operator in the Markov approximation has the form

$$\dot{\rho}(t) = -\frac{i}{\hbar}\left[H_S, \rho(t)\right] - \int_0^{t-t_0} \mathrm{d}\tau \ \mathrm{tr}_B\left\{\mathcal{L}_V\mathcal{L}_V(\tau)B_{eq}\rho(t)\right\} \ .$$

If the bath-correlation functions decay fast enough, the integrand vanishes at times earlier than $t-t_0$ and the upper integration boundary can be taken to infinity. This yields the Redfield equation, which is characterized by t-independent transition rates,

$$\dot{\rho}(t) = -\frac{i}{\hbar}\left[H_S, \rho(t)\right] - \int_0^{\infty} \mathrm{d}\tau \ \mathrm{tr}_B\left\{\mathcal{L}_V\mathcal{L}_V(\tau)B_{eq}\rho(t)\right\} \ .$$

We are interested in the steady state situation, which is established in the limit $t \to \infty$ and at which the reduced density matrix is constant in time $\dot{\rho} = 0$. Writing the commutators explicitly and using the notation,

$$\lim_{t\to\infty}\rho(t) = \rho_\infty \ ,$$

we obtain the equation for the stationary density operator,

$$-\frac{i}{\hbar}\left[H_S, \rho_\infty\right] - \frac{1}{\hbar^2}\int_0^{\infty} \mathrm{d}\tau \ \mathrm{tr}_B\left\{[V, [V(\tau), B_{eq}\rho_\infty]]\right\} = 0 \quad . \tag{5.11}$$

Next the expression for the current, Eq. (5.2), is written in terms of the reduced density operator,

$$\begin{aligned} I_\alpha &= e\,\mathrm{tr}_{B+S}\left\{\hat{R}(t)\hat{I}_\alpha\right\} \\ &= e\,\mathrm{tr}_{B+S}\left\{P\hat{R}(t)\hat{I}_\alpha\right\} + e\,\mathrm{tr}_{B+S}\left\{Q\hat{R}(t)\hat{I}_\alpha\right\} \\ &= e\,\mathrm{tr}_{B+S}\left\{B_{eq}\rho(t)\hat{I}_\alpha\right\} + e\,\mathrm{tr}_{B+S}\left\{Q\hat{R}(t)\hat{I}_\alpha\right\} \\ &= e\,\mathrm{tr}_{B+S}\left\{Q\hat{R}(t)\hat{I}_\alpha\right\} \ . \end{aligned}$$

The term including P vanishes, because the current operator is linear in the electrode DOF. The expression for $Q\hat{R}(t)$ can be extracted from Eq. (5.11), which gives the current in terms of the reduced density operator

$$I_\alpha = -i\frac{e}{\hbar}\int_0^{\infty} \mathrm{d}\tau \ \mathrm{tr}_{B+S}\left\{\left[V(\tau), B_{eq}\rho_\infty\hat{I}_\alpha\right]\right\} \ . \tag{5.12}$$

5.1.3 Polaron transformation of the Hamiltonian

The many-particle Hamiltonian (Eqs. 3.8) contains the interaction terms V and H_{ne}. In order to obtain an expression that contains only one interaction term, which will be treated by perturbation theory, the Hamiltonian will be transformed, $\tilde{H} = e^S H e^{-S}$. The transformation S is chosen such, that there is no vibronic coupling term in the new Hamiltonian $\tilde{H}$. This is the case if (from now on atomic units, where $\hbar = 1, e = 1$, will be used)

$$\begin{aligned} S &= \sum_{j,l} \frac{\kappa_l^{(j)}}{\sqrt{2}\omega} \left(a_l^\dagger - a_l\right) c_j^\dagger c_j \qquad \text{(electron transport)} , \\ S &= \sum_{j,l} \frac{\kappa_l^{(j)}}{\sqrt{2}\omega} \left(a_l^\dagger - a_l\right) c_j c_j^\dagger \qquad \text{(hole transport)} . \end{aligned}$$

The transformation is performed with the help of its series expansion

$$\tilde{H} = e^S H e^{-S} = H + [S, H] + \frac{1}{2!}[S, [S, H]] + \cdots , \tag{5.13}$$

which gives

$$\begin{aligned} \tilde{H} &= \tilde{H}_0 + \tilde{V} , \\ \tilde{H}_0 &= \tilde{H}_S + \tilde{H}_B , \\ \tilde{H}_S &= \sum_l \omega_l a_l^\dagger a_l + \sum_{j \in M} \tilde{E}_j c_j^\dagger c_j + \sum_{l,j,j'} \frac{\kappa_l^{(j)} \kappa_l^{(j')}}{2\,\omega_l} c_j^\dagger c_{j'}^\dagger c_j c_{j'} , \\ \tilde{H}_B &= \sum_{k \in L,R} E_k c_k^\dagger c_k , \\ \tilde{V} &= \sum_{j \in M} \sum_{k \in L,R} \left(V_{jk} X_j c_j^\dagger c_k + V_{kj} X_j^\dagger c_j c_k^\dagger\right) , \end{aligned} \tag{5.14}$$

where constant terms, which do not contribute to dynamics, were skipped, so that Eq. 5.14 describes both electron and hole transport. The molecular orbital energy was renormalized by the reorganization energy (also called the polaron shift)

$$\tilde{E}_j = E_j - \sum_l \frac{\left(\kappa_l^{(j)}\right)^2}{2\omega_l} \qquad \text{(e. t.)} , \tag{5.15}$$

$$\tilde{E}_j = E_j + \sum_l \frac{\left(\kappa_l^{(j)}\right)^2}{2\omega_l} \qquad \text{(h. t.)} . \tag{5.16}$$

The operator X_j is given by the expression

$$X_j = e^{-i\sum_l \frac{\kappa_l^{(j)}}{\omega_l} p_l} = e^{\sum_l \frac{\kappa_l^{(j)}}{\sqrt{2}\omega_l}\left(a_l^\dagger - a_l\right)}, \tag{5.17}$$

where $p_l = \frac{i}{\sqrt{2}}\left(a_l^\dagger - a_l\right)$ is the dimensionless nuclear momentum of normal mode l. The last term in Eqs. 5.14 is neglected, ignoring processes where two electrons (holes) are simultaneously created on the molecule.

5.1.4 Solving the Equation of Motion

In this section, we will express the generic EOM in Eq. (5.11) in terms of the Hamiltonian derived in Sec. 5.1.3 and we will transform the operator equation into a system of linear equations by taking the matrix elements with respect to the vibrational and electronic molecular states. Using the Hamiltonian of Sec. 5.1.3 the expression for the time-dependent interaction operator becomes

$$\begin{aligned}
\tilde{V}(\tau) &= e^{-i\tilde{H}_0\tau}\tilde{V}e^{+i\tilde{H}_0\tau} \\
&= \sum_{k'\in L,R}\sum_{j'\in M}\Big(V_{j'k'}e^{-i\left(\tilde{E}_{j'}-E_{k'}\right)\tau}X_{j'}(\tau)c_{j'}^\dagger c_{k'} \\
&\quad + V_{k'j'}e^{+i\left(\tilde{E}_{j'}-E_{k'}\right)\tau}X_{j'}^\dagger(\tau)c_{j'}c_{k'}^\dagger\Big)\ ,
\end{aligned} \tag{5.18}$$

where $X_{j'}(\tau) = e^{-i\sum_l \omega_l a_l^\dagger a_l \tau} X_{j'} e^{+i\sum_l \omega_l a_l^\dagger a_l \tau}$. The current operator, Eq. (5.3), takes the form

$$\hat{I}_\alpha = i\left[\tilde{H}, \hat{N}_\alpha\right] = 2\,i\sum_{j,k\in\alpha}\left(V_{jk}X_j c_j^\dagger c_k - V_{kj}X_j^\dagger c_j c_k^\dagger\right)\ . \tag{5.19}$$

Using Eq. (5.11), expanding the commutator, and exploiting the Hermiticity of the operators we obtain

$$0 = -i\left[\tilde{H}_S, \rho_\infty\right] - \int_0^\infty \mathrm{d}\tau\ \mathrm{tr}_B\left\{\tilde{V}\tilde{V}(\tau)B_{eq}\rho_\infty - \tilde{V}B_{eq}\rho_\infty\tilde{V}(\tau) + h.c.\right\}\quad .$$

The multiplication of $\tilde{V}$ by $\tilde{V}(\tau)$ yields four terms. If the trace with respect to the electrode DOF is taken, those terms including $c_k c_{k'} B_{eq}$ and $c_k^\dagger c_{k'}^\dagger B_{eq}$ vanish. The other two terms give

$$\begin{aligned}
\mathrm{tr}_B\left\{c_k^\dagger c_{k'}B_{eq}\right\} &= \delta_{kk'}f(E_k-\mu_\alpha), \\
\mathrm{tr}_B\left\{c_k c_{k'}^\dagger B_{eq}\right\} &= \delta_{kk'}\left(1-f(E_k-\mu_\alpha)\right),
\end{aligned}$$

where f is the Fermi distribution function. Thus we obtain

$$
\begin{aligned}
0 &= -i\left[\tilde{H}_S, \rho_\infty\right] - \int_0^\infty \mathrm{d}\tau \sum_{j,j'\in M} \sum_{k\in L,R} \left(D^\dagger + D\right) \qquad , (5.20)\\
D &= V_{jk}V_{kj'}e^{+i\left(\tilde{E}_{j'}-E_k\right)\tau} X_j X_{j'}^\dagger(\tau) c_j^\dagger c_{j'} \rho_\infty \left(1-f(E_k-\mu_\alpha)\right)\\
&\quad + V_{j'k}V_{kj}e^{-i\left(\tilde{E}_{j'}-E_k\right)\tau} X_j^\dagger X_{j'}(\tau) c_j c_{j'}^\dagger \rho_\infty f(E_k-\mu_\alpha)\\
&\quad - V_{jk}V_{kj'}e^{+i\left(\tilde{E}_{j'}-E_k\right)\tau} X_j c_j^\dagger \rho_\infty c_{j'} X_{j'}^\dagger(\tau) f(E_k-\mu_\alpha)\\
&\quad - V_{j'k}V_{kj}e^{-i\left(\tilde{E}_{j'}-E_k\right)\tau} X_j^\dagger c_j \rho_\infty c_{j'}^\dagger X_{j'}(\tau) \left(1-f(E_k-\mu_\alpha)\right).
\end{aligned}
$$

In the next step, we derive the representation of the operator Eq. (5.20) in a vibrational basis. To this end, Eq. (5.20) is multiplied by $\langle\boldsymbol{\nu}_1|$ from the left and $|\boldsymbol{\nu}_2\rangle$ from the right, and the completeness relation, $\sum_i |\boldsymbol{\nu}_i\rangle\langle\boldsymbol{\nu}_i| = 1$, is inserted twice,

$$
\begin{aligned}
0 &= -i\left\langle \boldsymbol{\nu}_1 \middle| \left[\tilde{H}_S, \rho_\infty\right] \middle| \boldsymbol{\nu}_2 \right\rangle - \int_0^\infty \mathrm{d}\tau \sum_{j,j'\in M} \sum_{k\in L,R} \sum_{\boldsymbol{\nu}_3,\boldsymbol{\nu}_4} \left[\left\langle \boldsymbol{\nu}_1 \middle| D^\dagger \middle| \boldsymbol{\nu}_2 \right\rangle + \langle \boldsymbol{\nu}_1 | D | \boldsymbol{\nu}_2 \rangle\right] \qquad (5.21)\\
&\langle \boldsymbol{\nu}_1 | D | \boldsymbol{\nu}_2 \rangle =\\
&\quad V_{jk}V_{kj'}e^{+i\left(\tilde{E}_{j'}-E_k\right)\tau} \langle\boldsymbol{\nu}_1|X_j|\boldsymbol{\nu}_3\rangle\langle\boldsymbol{\nu}_3|X_{j'}^\dagger(\tau)|\boldsymbol{\nu}_4\rangle\langle\boldsymbol{\nu}_4|c_j^\dagger c_{j'}\rho_\infty|\boldsymbol{\nu}_2\rangle \left(1-f(E_k-\mu_\alpha)\right)\\
&+ V_{j'k}V_{kj}e^{-i\left(\tilde{E}_{j'}-E_k\right)\tau} \langle\boldsymbol{\nu}_1|X_j^\dagger|\boldsymbol{\nu}_3\rangle\langle\boldsymbol{\nu}_3|X_{j'}(\tau)|\boldsymbol{\nu}_4\rangle\langle\boldsymbol{\nu}_4|c_j c_{j'}^\dagger\rho_\infty|\boldsymbol{\nu}_2\rangle f(E_k-\mu_\alpha)\\
&- V_{jk}V_{kj'}e^{+i\left(\tilde{E}_{j'}-E_k\right)\tau} \langle\boldsymbol{\nu}_1|X_j|\boldsymbol{\nu}_3\rangle\langle\boldsymbol{\nu}_3|c_j^\dagger\rho_\infty c_{j'}|\boldsymbol{\nu}_4\rangle\langle\boldsymbol{\nu}_4|X_{j'}^\dagger(\tau)|\boldsymbol{\nu}_2\rangle f(E_k-\mu_\alpha)\\
&- V_{j'k}V_{kj}e^{-i\left(\tilde{E}_{j'}-E_k\right)\tau} \langle\boldsymbol{\nu}_1|X_j^\dagger|\boldsymbol{\nu}_3\rangle\langle\boldsymbol{\nu}_3|c_j\rho_\infty c_{j'}^\dagger|\boldsymbol{\nu}_4\rangle\langle\boldsymbol{\nu}_4|X_{j'}(\tau)|\boldsymbol{\nu}_2\rangle \left(1-f(E_k-\mu_\alpha)\right) .
\end{aligned}
$$

The term $\langle\boldsymbol{\nu}_i|X_j|\boldsymbol{\nu}_{i'}\rangle$ is the product of Franck-Condon factors of various modes

$$
\langle\boldsymbol{\nu}_i|X_j|\boldsymbol{\nu}_{i'}\rangle = \left\langle \boldsymbol{\nu}_i \middle| \prod_l e^{\frac{\kappa_l^{(j)}}{\sqrt{2}\omega_l}\left(a_l^\dagger - a_l\right)} \middle| \boldsymbol{\nu}_{i'} \right\rangle = \prod_l \left\langle \nu_l^{(i)} \middle| X_l^{(j)} \middle| \nu_l^{(i')} \right\rangle .
$$

Here it was used, that the total vibrational wave function factorizes into the functions of the single modes, $|\boldsymbol{\nu}_i\rangle = \prod_l |\nu_l^{(i)}\rangle$, where $\nu_l^{(i)}$ is the quantum number of normal mode l in vibrational state i. Furthermore the abbreviation

$$
X_l^{(j)} = e^{\frac{\kappa_l^{(j)}}{\sqrt{2}\omega_l}\left(a_l^\dagger - a_l\right)}
$$

was used. The Franck-Condon factors of the individual modes are given by:

$$\langle\nu'|X_l^{(j)}|\nu\rangle = \begin{cases} \displaystyle\sum_{h=0}^{\nu} \frac{\left(-\frac{\kappa^{(j)^2}}{2\omega^2}\right)^h \left(\frac{\kappa^{(j)}}{\sqrt{2}\omega}\right)^{\nu'-\nu} \sqrt{\nu!\nu'!}}{h!\,(\nu'-\nu+h)!\,(\nu-h)!} e^{-\frac{\kappa^{(j)^2}}{4\omega^2}} & \text{if} \quad \nu' \geq \nu \\ \displaystyle\sum_{h=0}^{\nu'} \frac{\left(-\frac{\kappa^{(j)^2}}{2\omega^2}\right)^h \left(-\frac{\kappa^{(j)}}{\sqrt{2}\omega}\right)^{\nu-\nu'} \sqrt{\nu!\nu'!}}{h!\,(\nu-\nu'+h)!\,(\nu'-h)!} e^{-\frac{\kappa^{(j)^2}}{4\omega^2}} & \text{if} \quad \nu \geq \nu' \end{cases} \tag{5.22}$$

For the time-dependent X_j-operator one obtains

$$\langle\boldsymbol{\nu}_i|X_j(\tau)|\boldsymbol{\nu}_{i'}\rangle = \langle\boldsymbol{\nu}_i|X_j|\boldsymbol{\nu}_{i'}\rangle e^{-i\sum_l \omega_l\left(\nu_l^{(i)}-\nu_l^{(i')}\right)}\,.$$

Introducing the abbreviation $\langle\boldsymbol{\nu}_i|X_j|\boldsymbol{\nu}_{i'}\rangle = X_j^{ii'}$, and using the relation $\langle\nu'|X_l^{(j)^\dagger}|\nu\rangle = \langle\nu|X_l^{(j)}|\nu'\rangle$ Eq. (5.21) becomes

$$\begin{aligned} 0 &= -i\left\langle\boldsymbol{\nu}_1\left|\left[\tilde{H}_S,\rho_\infty\right]\right|\boldsymbol{\nu}_2\right\rangle \\ &\quad - \sum_{j,j'\in M}\sum_{k\in L,R}\sum_{\boldsymbol{\nu}_3,\boldsymbol{\nu}_4}\left[\left\langle\boldsymbol{\nu}_1\left|D^\dagger\right|\boldsymbol{\nu}_2\right\rangle + \left\langle\boldsymbol{\nu}_1\left|D\right|\boldsymbol{\nu}_2\right\rangle\right] \qquad (5.23) \\ \langle\boldsymbol{\nu}_1|D|\boldsymbol{\nu}_2\rangle &= \sigma_{jj'}^{34}X_j^{13}X_{j'}^{43}\langle\boldsymbol{\nu}_4|c_j^\dagger c_{j'}\rho_\infty|\boldsymbol{\nu}_2\rangle\left(1-f(E_k-\mu_\alpha)\right) \\ &\quad +\sigma_{jj'}^{34^*}X_j^{31}X_{j'}^{34}\langle\boldsymbol{\nu}_4|c_j c_{j'}^\dagger\rho_\infty|\boldsymbol{\nu}_2\rangle f(E_k-\mu_\alpha) \\ &\quad -\sigma_{jj'}^{42}X_j^{13}X_{j'}^{24}\langle\boldsymbol{\nu}_3|c_j^\dagger\rho_\infty c_{j'}|\boldsymbol{\nu}_4\rangle f(E_k-\mu_\alpha) \\ &\quad -\sigma_{jj'}^{42^*}X_j^{31}X_{j'}^{42}\langle\boldsymbol{\nu}_3|c_j\rho_\infty c_{j'}^\dagger|\boldsymbol{\nu}_4\rangle\left(1-f(E_k-\mu_\alpha)\right)\,. \end{aligned}$$

Here we used the abbreviation

$$\sigma_{jj'}^{ll'} = V_{jk}V_{kj'}\int_0^\infty \mathrm{d}\tau e^{+i\left(\tilde{E}_{j'}-E_k+\sum_l\omega_l\left(\nu_l^{(l)}-\nu_l^{(l')}\right)\right)\tau}\,. \tag{5.24}$$

In order to convert Eq. (5.23) into a matrix equation, we also introduce electronic many-particle basis states $|\Psi\rangle$, and multiply Eq. (5.23) by $\langle\Psi_1|$ from the left and $|\Psi_2\rangle$ from the right,

$$\begin{aligned} 0 &= -i\left\langle\Psi_1\left|\left\langle\boldsymbol{\nu}_1\left|\left[\tilde{H}_S,\rho_\infty\right]\right|\boldsymbol{\nu}_2\right\rangle\right|\Psi_2\right\rangle \\ &\quad - \sum_{j,j'\in M}\sum_{k\in L,R}\sum_{\boldsymbol{\nu}_3,\boldsymbol{\nu}_4}\left[\left\langle\Psi_1\left|\left\langle\boldsymbol{\nu}_1\left|D^\dagger\right|\boldsymbol{\nu}_2\right\rangle\right|\Psi_2\right\rangle + \left\langle\Psi_1\left|\left\langle\boldsymbol{\nu}_1\left|D\right|\boldsymbol{\nu}_2\right\rangle\right|\Psi_2\right\rangle\right] \\ \langle\Psi_1|\langle\boldsymbol{\nu}_1|D|\boldsymbol{\nu}_2\rangle|\Psi_2\rangle &= \sigma_{jj'}^{34}X_j^{13}X_{j'}^{43}\langle\Psi_1|\langle\boldsymbol{\nu}_4|c_j^\dagger c_{j'}\rho_\infty|\boldsymbol{\nu}_2\rangle|\Psi_2\rangle\left(1-f(E_k-\mu_\alpha)\right) \\ &\quad +\sigma_{jj'}^{34^*}X_j^{31}X_{j'}^{34}\langle\Psi_1|\langle\boldsymbol{\nu}_4|c_j c_{j'}^\dagger\rho_\infty|\boldsymbol{\nu}_2\rangle|\Psi_2\rangle f(E_k-\mu_\alpha) \\ &\quad -\sigma_{jj'}^{42}X_j^{13}X_{j'}^{24}\langle\Psi_1|\langle\boldsymbol{\nu}_3|c_j^\dagger\rho_\infty c_{j'}|\boldsymbol{\nu}_4\rangle|\Psi_2\rangle f(E_k-\mu_\alpha) \\ &\quad -\sigma_{jj'}^{42^*}X_j^{31}X_{j'}^{42}\langle\Psi_1|\langle\boldsymbol{\nu}_3|c_j\rho_\infty c_{j'}^\dagger|\boldsymbol{\nu}_4\rangle|\Psi_2\rangle\left(1-f(E_k-\mu_\alpha)\right)\,. \end{aligned}$$

This produces a homogeneous system of linear equations, $\mathbf{Cx} = \mathbf{0}$, where $\mathbf{C}$ is the coefficient matrix containing the transition rates and the vector $\mathbf{x}$ contains the density matrix elements, $\langle \Psi_j | \langle \boldsymbol{\nu}_l | \rho_\infty | \boldsymbol{\nu}_{l'} \rangle | \Psi_{j'} \rangle$, in a column. The system of equations is solved under the condition that $\mathrm{tr}\{\rho_\infty\} = 1$.

The integral over τ in Eq. (5.24)can be rewritten using the relation [74]

$$\int_0^\infty \mathrm{d}\tau e^{\pm i\epsilon\tau} = \pm i PV\left(\frac{1}{\epsilon}\right) + \pi\delta(\epsilon) \;, \tag{5.25}$$

where PV denotes the Cauchy Principal Value integral and δ is the Dirac-δ-function. In this form the similarity between the transition rates in the EOM and the exact definition of the matrix elements of the width function Γ and the level shift Δ is evident,

$$\begin{aligned} \Gamma(E)_{jj'} &= 2\pi \sum_k V_{jk} V_{kj'} \delta(E - E_k) \;, \\ \Delta(E)_{jj'} &= \frac{1}{2\pi} PV \int \mathrm{d}E' \frac{\Gamma(E')_{jj'}}{E - E'} \;. \end{aligned}$$

However, matters become more complicated by the appearance of the Fermi functions.

It should be noted that in the presence of vibronic coupling the EOM for the many-particle density operator ρ can no longer be expressed in terms of its single-particle pendant, which makes a compact notation of the transition rates difficult. An approximate reduction scheme is proposed in [75] but complicates matters by introducing nonlinearities in the system of equations. When choosing the number of orbitals included in the actual calculation, it should be noted that the number of electronic many-particle states N increases with the n^{th} power of 2, $N = 2^n$, where n is the number of single-particle states.

5.1.5 Expression for the Current

Starting from Eq. (5.12), we will derive an expression for the current through electrode α for the Hamiltonian derived in Sec. 5.1.3. First, we will expand the commutator in Eq. (5.12) and exploit the fact, that the two terms in the trace are the Hermitian conjugates of each other,

$$\begin{aligned} I_\alpha &= -i \int_0^\infty \mathrm{d}\tau \, \left[\mathrm{tr}_{B+S}\left\{ \tilde{V}(\tau) B_{eq} \rho_\infty \hat{I}_\alpha \right\} - \left(\mathrm{tr}_{B+S}\left\{ \tilde{V}(\tau) B_{eq} \rho_\infty \hat{I}_\alpha \right\} \right)^* \right] \\ &= -2\, i \Im \left[\int_0^\infty \mathrm{d}\tau \; \mathrm{tr}_{B+S}\left\{ \tilde{V}(\tau) B_{eq} \rho_\infty \hat{I}_\alpha \right\} \right] \;. \end{aligned} \tag{5.26}$$

Inserting the expressions for $\tilde{V}(\tau)$ and $\hat{I}_\alpha$ (Eqs. (5.18) and (5.19)) and taking the trace with respect to the electrode DOF we obtain,

$$\begin{aligned} I_\alpha &= 4\,\Re\Bigg[\int_0^\infty \mathrm{d}\tau \sum_{j,j'\in M}\sum_{k\in\alpha} \\ &\quad V_{jk}V_{kj'}e^{+i\left(\tilde{E}_{j'}-E_k\right)\tau}\mathrm{tr}_S\left\{X_j X_{j'}^\dagger(\tau)c_j^\dagger c_{j'}\rho_\infty\right\}\left(1-f(E_k-\mu_\alpha)\right) \\ &\quad -V_{j'k}V_{kj}e^{-i\left(\tilde{E}_{j'}-E_k\right)\tau}\mathrm{tr}_S\left\{X_j^\dagger X_{j'}(\tau)c_j c_{j'}^\dagger\rho_\infty\right\}f(E_k-\mu_\alpha)\Bigg]\,. \end{aligned} \tag{5.27}$$

Next, the trace with respect to the vibrational and electronic DOF of the molecule has to be taken. The completeness relation of the vibrational states is inserted twice. This gives

$$\begin{aligned} I_\alpha &= 4\,\Re\Bigg[\sum_{j,j',i\in M}\sum_{k\in\alpha}\sum_{\boldsymbol{\nu}_1,\boldsymbol{\nu}_2,\boldsymbol{\nu}_3} \\ &\quad \left(1-f(E_k-\mu_\alpha)\right)\sigma_{jj'}^{32}X_j^{12}X_{j'}^{23}\langle\Psi_i|\langle\boldsymbol{\nu}_3|c_j^\dagger c_{j'}\rho_\infty|\boldsymbol{\nu}_1\rangle|\Psi_i\rangle \\ &\quad -f(E_k-\mu_\alpha)\;\sigma_{jj'}^{23^*}X_j^{12}X_{j'}^{23}\langle\Psi_i|\langle\boldsymbol{\nu}_3|c_j c_{j'}^\dagger\rho_\infty|\boldsymbol{\nu}_1\rangle|\Psi_i\rangle\Bigg]\,, \end{aligned} \tag{5.28}$$

where the sum over i extends over all electronic many-particle states.

5.1.6 Electronic single level system without vibronic coupling

In this section, we will present the rate and current equations of a purely electronic single level system without vibronic coupling. This serves as a simple illustration of the rather complex equations derived in the previous sections and enables a formal comparison with scattering theory.

The purely electronic equation of motion is given by

$$\begin{aligned} 0 &= -i\left[H_S,\rho_\infty\right]-\int_0^\infty \mathrm{d}\tau\sum_{j,j'\in M}\sum_{k\in L,R}\Big[\\ &\quad V_{jk}V_{kj'}e^{+i\left(E_{j'}-E_k\right)\tau}c_j^\dagger c_{j'}\rho_\infty\left(1-f(E_k-\mu_\alpha)\right) \\ &\quad +V_{j'k}V_{kj}e^{-i\left(E_{j'}-E_k\right)\tau}c_j c_{j'}^\dagger\rho_\infty f(E_k-\mu_\alpha) \\ &\quad -V_{jk}V_{kj'}e^{+i\left(E_{j'}-E_k\right)\tau}c_j^\dagger\rho_\infty c_{j'}f(E_k-\mu_\alpha) \\ &\quad -V_{j'k}V_{kj}e^{-i\left(E_{j'}-E_k\right)\tau}c_j\rho_\infty c_{j'}^\dagger\left(1-f(E_k-\mu_\alpha)\right)\Big]\,. \end{aligned} \tag{5.29}$$

A single level system consists of an occupied, $|1\rangle$, and an empty state, $|0\rangle$. When multiplying Eq. (5.29) by $\langle 1|$ from the left and $|1\rangle$ from the right, the term due to the coherent part of the EOM vanishes and the dissipative part becomes

$$0 = -\int_0^\infty \mathrm{d}\tau \sum_{k\in L,R} \big[(1-f(E_k-\mu_\alpha))\,|V_{1k}|^2\, e^{+i(E_1-E_k)\tau}\langle 1|\rho_\infty|1\rangle \\ -f(E_k-\mu_\alpha)\,|V_{1k}|^2\, e^{+i(E_1-E_k)\tau}\langle 0|\rho_\infty|0\rangle + c.c.\big] \ . \quad (5.30)$$

Writing the complex conjugate expression explicitly and collecting terms, Eq. (5.30) becomes

$$\begin{aligned} 0 \ &= \ -\int_0^\infty \mathrm{d}\tau \sum_{k\in L,R} \qquad (5.31)\\ &\big[(1-f(E_k-\mu_\alpha))\,|V_{1k}|^2\left(e^{+i(E_1-E_k)\tau}+e^{-i(E_1-E_k)\tau}\right)\langle 1|\rho_\infty|1\rangle \\ &-f(E_k-\mu_\alpha)\,|V_{1k}|^2\left(e^{+i(E_1-E_k)\tau}+e^{-i(E_1-E_k)\tau}\right)(1-\langle 1|\rho_\infty|1\rangle)\big]\,, \end{aligned}$$

where it was used, that the occupation probabilities add to one, $\langle 1|\rho_\infty|1\rangle + \langle 0|\rho_\infty|0\rangle = 1$. Using Eq. (5.25), Eq. (5.31) can be rewritten as

$$\begin{aligned} 0 \ &= \ -\sum_{k\in L,R} \big[(1-f(E_k-\mu_\alpha))\,|V_{1k}|^2\, 2\pi\delta(E_1-E_k)\langle 1|\rho_\infty|1\rangle \\ &\quad -f(E_k-\mu_\alpha)\,|V_{1k}|^2\, 2\pi\delta(E_1-E_k)\,(1-\langle 1|\rho_\infty|1\rangle)\big]\,, \\ &= \ -\sum_{k\in L,R} \big[|V_{1k}|^2\, 2\pi\delta(E_1-E_k)\langle 1|\rho_\infty|1\rangle \\ &\quad -f(E_1-\mu_\alpha)\,|V_{1k}|^2\, 2\pi\delta(E_1-E_k)\big]\,, \\ &= \ -\left[\Gamma_L(E_1)+\Gamma_R(E_1)\right]\langle 1|\rho_\infty|1\rangle \\ &\quad -\left[f(E_1-\mu_L)\Gamma_L(E_1)+f(E_1-\mu_R)\Gamma_R(E_1)\right]\ . \qquad (5.32) \end{aligned}$$

Employing Eq. (5.32) the population of the singly occupied state can be expressed as

$$\langle 1|\rho_\infty|1\rangle = \frac{f(E_1-\mu_L)\Gamma_L(E_1)+f(E_1-\mu_R)\Gamma_R(E_1)}{\Gamma_L(E_1)+\Gamma_R(E_1)} \qquad (5.33)$$

The current of a purely electronic single level system can be derived in the same manner as the population. Rewriting Eq. (5.28) for a single electronic

level we obtain,

$$I_\alpha = 4\,\Re\left\{\int_0^\infty \mathrm{d}\tau \sum_{k\in\alpha}\Big[\,(1-f(E_k-\mu_\alpha))\,|V_{1k}|^2\,e^{+i(E_1-E_k)\tau}\langle 1|\rho_\infty|1\rangle \right.$$
$$\left. -f(E_k-\mu_\alpha)\,|V_{1k}|^2\,e^{-i(E_1-E_k)\tau}\langle 0|\rho_\infty|0\rangle\Big]\right\}\ . \quad (5.34)$$

Using Eq (5.25) and replacing $\langle 0|\rho_\infty|0\rangle$ by $1-\langle 1|\rho_\infty|1\rangle$, Eq. (5.34) becomes

$$\begin{aligned} I_\alpha &= 4\sum_{k\in\alpha}\Big[\,(1-f(E_k-\mu_\alpha))\,|V_{1k}|^2\,\pi\delta(E_1-E_k)\langle 1|\rho_\infty|1\rangle \\ &\quad -f(E_k-\mu_\alpha)\,|V_{1k}|^2\,\pi\delta(E_1-E_k)\,(1-\langle 1|\rho_\infty|1\rangle)\Big)\ , \\ &= 4\sum_{k\in\alpha}\left[|V_{1k}|^2\,\pi\delta(E_1-E_k)\langle 1|\rho_\infty|1\rangle - f(E_k-\mu_\alpha)\,|V_{1k}|^2\,\pi\delta(E_1-E_k)\right]\ , \\ &= 2\,\Gamma_\alpha(E_1)\langle 1|\rho_\infty|1\rangle - 2\,f(E_1-\mu_\alpha)\Gamma_\alpha(E_1)\ , \end{aligned} \quad (5.35)$$

Inserting Eq. (5.33) into Eq. (5.35) we obtain the final expression for the current through a purely electronic single level system (setting $\alpha = L$),

$$I_L = 2\,\frac{\Gamma_L(E_1)\cdot\Gamma_R(E_1)}{\Gamma_L(E_1)+\Gamma_R(E_1)}\,(f_R(E_1-\mu_R)-f_L(E_1-\mu_L))\ . \quad (5.36)$$

5.1.7 Comparison to Scattering Theory

The difference between the current obtained from the density-matrix and the scattering approach can be analyzed for the purely electronic case assuming a single electronic state only. In this case the current based on scattering theory is given by

$$I = \frac{1}{\pi}\int_{-\infty}^{+\infty}\mathrm{d}E\frac{\Gamma_L(E)\cdot\Gamma_R(E)\ (f_R(E-\mu_R)-f_L(E-\mu_L))}{(E-E_1-\Delta_L(E)-\Delta_R(E))^2+(\Gamma_L(E)+\Gamma_R(E))^2/4}\quad .$$

When neglecting the level-shift function Δ and taking the limit

$$\frac{1}{2}(\Gamma_L(E)+\Gamma_R(E))\to 0$$

we obtain

$$I = \int_{-\infty}^{+\infty}\mathrm{d}E\frac{\Gamma_L(E)\cdot\Gamma_R(E)\ (f_R(E-\mu_R)-f_L(E-\mu_L))}{\frac{1}{2}(\Gamma_L(E)+\Gamma_R(E))}\delta(E-E_1)\cdot \quad (5.37)$$

Solving the integral gives exactly Eq. (5.36).

This shows that quite severe approximations are necessary to get from the scattering current expression to the density matrix expression and differences in the I-V characteristic are to be expected when comparing both methods. Furthermore, we note that the operations above imply the wide-band approximation, which is characterized by a constant width Γ and zero level-shift Δ.

While the perturbational treatment constitutes a disadvantage of the density matrix approach, its advantage is that we need no longer assume relaxation of the vibration after each electronic scattering process. Instead, the approach allows to study the steady-state distribution of the vibrational degrees of freedom.

The assumption of zero relaxation is the other extreme as compared to the scattering treatment, where total vibrational relaxation was assumed after each transmission event. Therefore, effects due to absorption of vibrational quanta or, generally, due to transitions starting from a vibrationally excited state, are missed by the scattering treatment.

Within second order perturbation theory only sequential tunneling processes can be described. In sequential tunneling the charge carrier physically occupies the molecule and loses its phase memory, before it escapes into the other electrode by another tunneling process. Higher order processes, called cotunneling or superexchange, where a virtual intermediate state is formed, appear in fourth order of the interaction V [76]. The superexchange ($L \leftrightarrow R$) transition rates naturally contain the Pauli blocking factors (see e.g. Ref. [77]), that were discussed in Sec. 4.1. The sequential tunneling transition rates, of course, do not contain blocking factors in the electrodes, as only a single electrode is involved in this process and two consecutive processes are needed in order to transfer a hole from one electrode to the other. In Ref. [77] it was also found, that large vibronic coupling leads to a suppression of the cotunneling component relative to the sequential component of the current. Superexchange processes involve populations of the electrode states and coherences between electrode and molecular states [78], and can therefore not be described by the density matrix ρ, which was reduced to the molecular electronic and vibrational states. In scattering theory, on the other hand, the molecule-electrode interaction is included to infinite order, but it is not straightforwardly possible to differentiate between the sequential and superexchange transport mechanisms.

5.1.8 Technical Details of the Implementation

In this section, we discuss some of the technical details of the implementation of the density matrix formalism for the molecular junction considered in Sec. 5.2.

It would have been desirable to calculate the current via the density matrix formalism for the same electronic states and vibrational modes as via the scattering formalism. This could not be done, because of the sulfur states, which strongly couple to the electrodes and thus cannot be described within a perturbation treatment. In the I-V curve this becomes noticeable as large spikes which overlay the features of the benzene orbitals. Even state B in BDET (cf. Fig. 4.7) is coupled too strongly, which becomes noticeable as a density matrix calculation for this junction resulted in populations larger than 1 and lower than 0.

The violation of perturbation theory was analyzed for a purely electronic tight-binding model and can be summarized as follows: For a single electronic state, coupled equally to both electrodes, the coupling is merely a multiplicative factor (cf. Eq. (5.36)). The breakdown of perturbation theory in this case manifests itself in the fact that current-voltage steps do not broaden with increasing coupling strength. As soon as two electronic states are considered, the ratio between their coupling to the electrodes and their mutual level-spacing is decisive. If this ratio is too large, spikes appear in the I-V characteristic. Therefore, the density matrix treatment was restricted to the two benzene states A and B in BDBT coupled to a single mode (cf. Sec. 4.2.4).

Taking into account these two single-particle states, we have to consider four many-particle states (see scheme in Fig. 5.1): the neutral reference state, $|\Psi_g\rangle$, where both orbitals are occupied by electrons, a state with a hole in A, $|A\rangle = c_A|\Psi_g\rangle$, which, as A is lower in energy than B, corresponds to an electronic excitation, a state with a hole in B, $|B\rangle = c_B|\Psi_g\rangle$, and a state where both A and B are not occupied, $|0\rangle = c_A c_B|\Psi_g\rangle$.

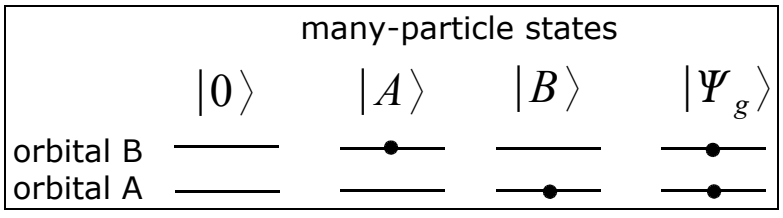

Figure 5.1: The relation between orbital occupancy and many-particle states. Black dots indicate electrons.

Only the electronic off-diagonal elements between single hole excitations, $\langle A|\rho_\infty|B\rangle$ and $\langle B|\rho_\infty|A\rangle$, are coupled to the electronic diagonal elements. This is in accord with Ref. [79] where it was shown that in second order perturbation theory only coherences between states of equal particle number contribute to transport. The coherent part of the EOM only gives a contribution to matrix elements that are off-diagonal in either the electronic or vibrational states or both. Furthermore, no direct transitions between states $|A\rangle$ and $|B\rangle$ exist.

It is sometimes claimed in the literature [80] that off-diagonal electronic matrix elements vanish under steady-state conditions except for the case of accidental degeneracies. We experienced that this is not a strict rule but that electronic off-diagonal density matrix elements become larger, the smaller the level-spacing.

If all vibrational and those two electronic off-diagonal elements are included in the EOM, the coefficient matrix of the linear system of equations has dimension $6 \cdot l^m \times 6 \cdot l^m$, where l is the size of the vibrational basis for a single mode, which is assumed to be the same for all m modes. If rather large vibrational basis sets are needed in order to achieve convergence, the amount of needed memory may easily exceed the amount that is offered by computers at the time this thesis was written. Therefore, the calculations presented below were restricted to a single vibrational normal mode.

For the electrode states $|\phi_k\rangle$ we use again the states calculated by DFT, which were broadened and shifted by the surface self-energy. Due to the broadening, the E_k's are complex and if we simply insert them into Eq. (5.23), the argument of the Fermi function would also become complex. Therefore, we have to devise some way to approximate these expressions. The terms including the δ- and the Fermi function can be exactly factorized into the Γ- and the Fermi function evaluated at energy

$$E = \tilde{E}_{j'} + \sum_l \omega_l \left(\nu_l^{(i)} - \nu_l^{(i')}\right) - \mu_\alpha \ , \tag{5.38}$$

while for the terms including the PV and the Fermi function this constitutes a local approximation. Another approximation would be to evaluate the Fermi function at the real part of the contact energies or to neglect the PV-term. Considering the term

$$\sum_k \left\{ i\,PV\left(\frac{1}{E-E_k}\right) f(E_k) + \pi\delta(E-E_k) f(E_k) \right\} \ ,$$

several approximations are possible:

1. The Fermi function in both the δ- and the PV-term is evaluated at the real part of the contact energies,

$$\sum_k \left\{ i\,PV\left(\frac{1}{E-E_k}\right) f(\Re(E_k)) + \pi\delta(E-E_k) f(\Re(E_k)) \right\} \ .$$

2. Both terms are factorized into Γ and Δ times the Fermi function evaluated at energy $E = \tilde{E}_{j'} + \sum_l \omega_l \left(\nu_l^{(i)} - \nu_l^{(i')}\right) - \mu_\alpha$.

$$\sum_k \left\{ i\,PV\left(\frac{1}{E-E_k}\right) f(E) + \pi\delta(E-E_k) f(E) \right\} \ .$$

3. The δ-function term is factorized and in the PV-term the Fermi function is evaluated at the real part of the contact energies,

$$\sum_k \left\{ i\,PV\left(\frac{1}{E-E_k}\right) f(\Re(E_k)) + \pi\delta(E-E_k) f(E) \right\} \ .$$

4. Terms containing the PV-term are neglected and the δ-function term is factorized

$$\sum_k \left\{ \pi\delta(E-E_k) f(E) \right\} \ .$$

For the weakly coupled model system investigated, most approximations, with the exception of approximation 1, gave nearly identical, reasonable results. Therefore the approximation with the least numerical effort (approximation 4) was used.

In the following, results that were obtained using the density matrix formalism are shown for the purely electronic case and when including either mode (a) or mode (d) (cf. Fig. 4.17). A comparison with the equivalent results obtained with scattering theory will be given. Convergence with respect to the vibrational basis set was achieved for a number of 25 vibrational states. The criterion for convergence was that the I-V curve did not change visibly when increasing the basis set further. This rather large vibrational basis set (25 functions) was necessary, because no mechanisms for vibrational relaxation were included and therefore all vibrational states connected by a not too small Franck-Condon factor had to be incorporated. The system coupled to two modes simultaneously could not be investigated because the employed vibrational basis set was too large. The density matrix calculations were solved at zero temperature and room temperature (RT), corresponding to $T = 293.15\,\mathrm{K}$.

In the data presented in the next section, the lower limit of the voltage range is given by the voltage at which the coefficient matrix of the system of linear equations becomes singular, because of the number of matrix elements equal zero. This takes place at higher voltages for the 0 K - calculation, than for the RT - data, because of the broadening of the Fermi function at room temperature, which decreases the number of non-zero coefficient matrix elements. The frequencies of both normal modes are too large to be excited thermally at RT, and vibrational excitation can only occur via electron transport. In our studies we do not include vibrational relaxation. Generally, however, vibrational relaxation could be included via the coupling to a thermal bath of secondary vibrational modes, via a simple, exponential phenomenological relaxation time (see Ref. [81] for a discussion of the difference between the two), and via intramolecular vibrational energy redistribution by anharmonic coupling between system modes.

5.2 Results and Discussion

In this section, we present data derived from purely electronic density matrix calculations of the BDBT molecular junction and compare with results from calculations that include vibronic coupling to two different modes. The I-V curves will be compared to the corresponding results from a scattering calculation.

5.2.1 Observables of Interest

Besides the current and conductivity, there is a variety of other observables of interest to characterize the electronic and vibrational non-equilibrium dynamics in molecular junctions. The average number of vibrational quanta in the stationary non-equilibrium state, is given by

$$\langle a^\dagger a \rangle = \sum_{l,\Psi} \nu_l \rho_{\Psi\Psi}^{\nu_l \nu_l}$$

with

$$\rho_{\Psi\Psi}^{\nu_l \nu_l} = \langle \nu_l | \langle \Psi | \rho | \Psi \rangle | \nu_l \rangle \ .$$

Here ν_l is the discrete vibrational quantum number and the sum is taken over all electronic states $|\Psi\rangle$. This quantity allows us to study the creation and destruction of vibrational quanta as a function of voltage.

The dynamics of the electronic states of the molecule is characterized by the occupation probabilities of the electronic many-particle states summed

over all diagonal vibrational elements,

$$\rho_{\Psi\Psi} = \sum_l \rho_{\Psi\Psi}^{\nu_l\nu_l} \ ,$$

as a function of voltage.

Finally, we will present the occupation probability of the vibrational states, which in equilibrium is given by the Boltzmann distribution

$$P_\nu^{eq} = \frac{e^{-\beta\omega\nu}}{\sum_{\nu'} e^{-\beta\omega\nu'}} \ .$$

At finite voltage the probability distribution of the vibrational states may deviate significantly from that at equilibrium. The non-equilibrium distribution is given by summing the diagonal elements of the reduced density matrix over the electronic states $|\Psi\rangle$

$$P_\nu^{neq} = \sum_\Psi \rho_{\Psi\Psi}^{\nu\nu} \ .$$

5.2.2 Purely Electronic Calculation

Fig. 5.2 shows the current through the benzene states A and B of BDBT, calculated via density matrix (solid black line) and scattering theory (red line). Steps, due to the two orbitals, appear at the same position in both curves. The step due to state B appears at 2.74 V, while that due to state A appears at 3.54 V. The step heights are not equal and the current features in the voltage range between the two steps and after the second step differ. The current obtained with scattering theory is lower before the second step and larger afterwards, and the edges are not as sharp as in the density matrix calculation. The sharp features in the density matrix data are due to the wide-band approximation (cf. Sec. 5.1.7). Below 2 V there is a vast range of zero current, which is not shown entirely. The features in between and after the last resonant step are due to the voltage-dependence of Γ.

Interestingly, the current obtained with the scattering approach is slightly larger for the calculation including only two states, than for the calculations of the previous chapter, where four additional sulfur states were included (cf. Fig. 4.19). The contact mediated interactions between benzene and sulfur states, obviously, lead to a reduction of the current.

Fig. 5.2 also shows the temperature dependence of the current using the reduced density matrix approach. The steps are noticeably broadened at RT (dashed curve), while the current features between the steps and after

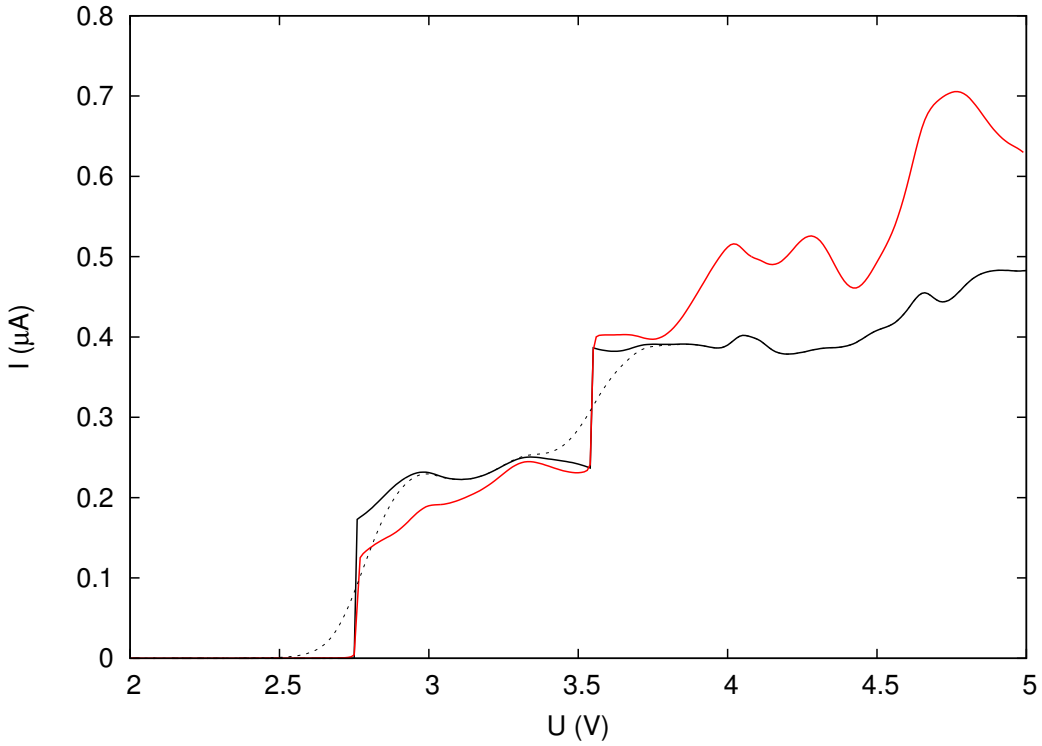

Figure 5.2: Comparison of the current based on a purely electronic calculation through states A and B of BDBT using density matrix theory at T=0 K (solid black line) and RT (dashed line), and using scattering theory (red line) at 0 K. The current below 2 V is zero and therefore not shown.

the second step are similar. This broadening of I-V features is due to the broadening of the Fermi distribution function.

Fig. 5.3 shows the occupation probabilities of the electronic many-particle states $|\Psi\rangle$ defined in Sec. 5.1.8, $\rho_{\Psi\Psi} = \langle\Psi|\rho_\infty|\Psi\rangle$. At low voltages both orbitals A and B are occupied and ρ_{gg} has probability unity. At 2.74 V the transition to state B comes into resonance, which causes the probability of ρ_{gg} (red curve) to drop sharply to 45%. At the same time the probability that orbital B is unoccupied while orbital A is still occupied, ρ_{BB} (blue curve), jumps abruptly to 55%. At 3.54 V hole transport through orbital A begins to contribute and the probabilities for the states ρ_{AA} (magenta curve) and ρ_{00} (black curve) increase, but remain rather small compared to the probabilities of the other two states.

The coherences of the system are rather small: for the real part of the

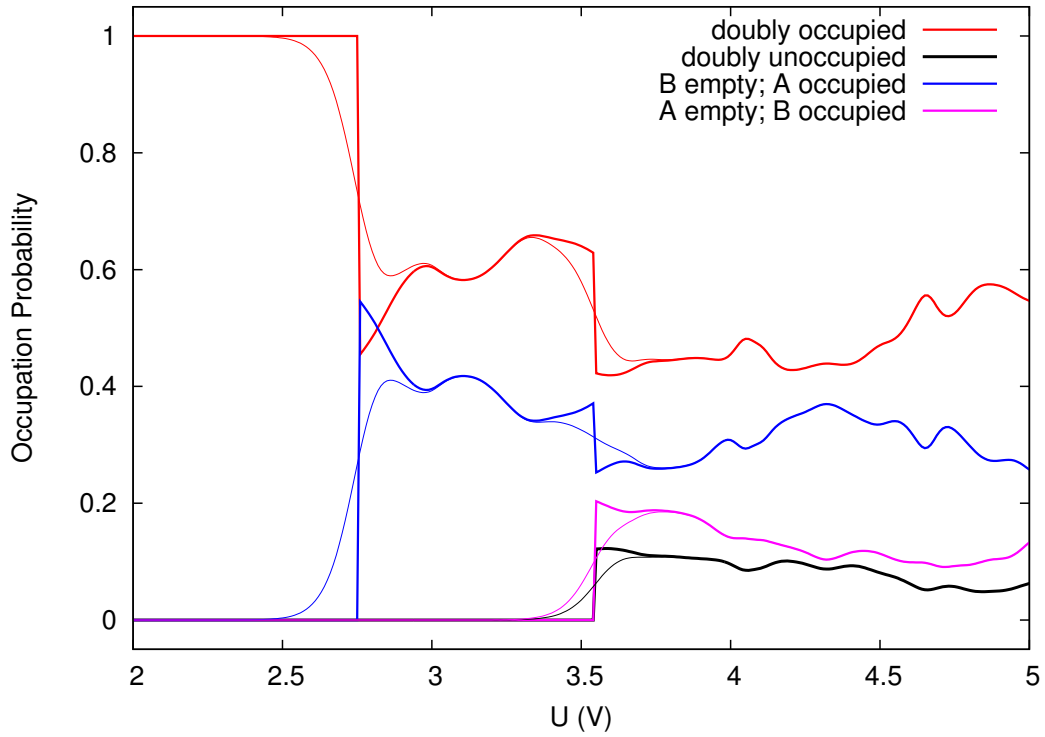

Figure 5.3: Occupation probability of the different electronic states (as indicated in the legend) as a function of voltage shown for T=0 K (bold lines) and room temperature (thin lines). The results are based on a purely electronic calculation.

coherences, $\Re(\rho_{AB}) = \Re(\rho_{BA}) < 1.3 \cdot 10^{-5}$, and for the imaginary part, $|\Im(\rho_{AB})| = |\Im(\rho_{BA})| < 1.7 \cdot 10^{-3}$.

5.2.3 Effect of the C-C-C bending mode

Next, we consider the influence of vibrational mode (a) (cf. Fig. 4.17) on the conductance of the electronic two level system. Fig. 5.4 shows the I-V characteristic when coupling to mode (a) is included in the calculation. At 2.74 V the transition to the vibrational ground state of orbital B comes into resonance and causes a large step. This takes place at the same voltage value as in the purely electronic calculation, indicating that the reorganization energy due to mode (a) for state B is rather small. Two smaller steps can be seen at 2.88 and 3.02 V, which correspond to transitions where one and two

additional vibrational quanta of this mode are excited, respectively. The step at 3.02 V is followed immediately by another step at 3.05 V, which is due to absorption of vibrational quanta by orbital A. Two more such steps occur at 3.19 and 3.33 V until at 3.47 V there is a comparably large step corresponding to the $\rho_{AA}^{\nu\nu} \leftarrow \rho_{gg}^{\nu\nu}$ - transitions for all already occupied vibrational states $|\nu\rangle$. This last step is shifted by an amount of -0.07 V with respect to the corresponding transitions in the purely electronic curve. There follow five clearly visible steps due to excitation of vibrational quanta at 3.61, 3.75, 3.89, 4.03, and 4.17 V. The step height becomes smaller with increasing voltage according to the respective Franck-Condon factors. The distance between these steps corresponds to twice the vibrational frequency, $2\hbar\omega/e = 0.14\,V$, as expected when applying a symmetric voltage window and in a harmonic potential (for studies of anharmonic potentials within a density matrix formalism see Ref. [82]). At room temperature (dashed line in Fig. 5.4) the steps are broadened. At 4.56 V the I-V characteristic at T=0 K and at room temperature can no longer be distinguished, indicating that transitions coupled by small Franck-Condon factors come into resonance.

The red curve in Fig. 5.4 shows the current for this 'two electronic levels-one mode' system obtained from a scattering theory calculation. The first step due to state B appears at 2.74 V. Its edges are again broadened compared to the density matrix curve. Another step can be seen at 2.88 V, which is due to excitation of vibrational quanta. At 3.47 V a step due to state A follows, and, compared to the density matrix calculation, the preceding steps, due to absorption of vibrational quanta, are absent. This was to be expected as in our scattering theory implementation the system is forced into its vibrational ground state after each scattering process. Only two more steps, due to excitation of vibrational quanta, follow at 3.61 and 3.75 V, while in the density matrix curve five steps can be seen. This might be due to the fact that in scattering theory a transition with a certain difference in the vibrational quantum number, Δn, is restricted to the transition starting in the vibrational ground state, $(m)_0^n$, while in the density matrix treatment all transitions starting from an occupied vibrational ground state, $(m)_{n'}^{n+n'}$, are included, which increases the intensity of each step.

The excitation and deexcitation of vibrational quanta, observed in the I-V curve, is reflected in the average number of vibrational quanta, $\langle a^\dagger a\rangle$, in the stationary non-equilibrium state, which is shown in Fig. 5.5. The curve obtained for zero temperature (solid line) shows that up to 2.74 V, which corresponds to the first step in the I-V curve, the system is in its vibrational ground state and the average number of vibrational quanta is zero. At 2.74 V $\langle a^\dagger a\rangle$ rises to a value of 0.3. With increasing voltage the average rises in two steps until it reaches a local maximum at 3.04 V. This corresponds to the

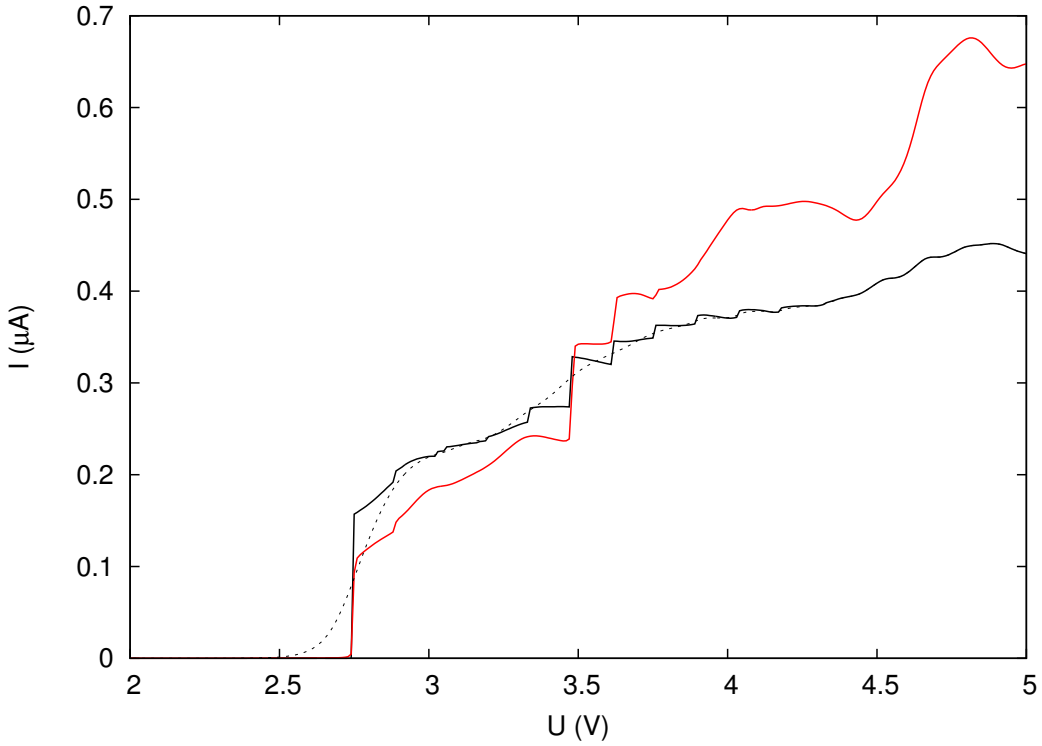

Figure 5.4: The current through states A and B of BDBT coupled to the mode with frequency $\omega = 566.12\,\mathrm{cm}^{-1}$ using the density matrix approach at 0 K (solid line) and at RT (dashed line), and using scattering theory at 0 K (red line).

last step in the I-V curve that is due to transport through orbital B. Just as this step is followed immediately by another step, the average vibrational quantum number decreases shortly after reaching the local maximum. This indicates absorption of vibrational quanta due to orbital A. The local maximum corresponds to almost 4 vibrational quanta. This means that also transitions from an excited vibrational ground state, e.g. $\rho_{AA}^{44} \leftarrow \rho_{gg}^{22}$, must have contributed, as the voltage is too low to excite four vibrational quanta at once. After two steps downwards at 3.47 V, the $\rho_{AA}^{\nu\nu} \leftarrow \rho_{gg}^{\nu\nu}$ transitions, for all vibrational states $|\nu\rangle$ that are occupied in the ground state, come into resonance and, in the following, the average vibrational quantum number rises due to vibrational excitations.

While at T=0 K the local maximum at 3.04 V reaches a value of 3.91, at room temperature the broadening leads to a situation where the step up at

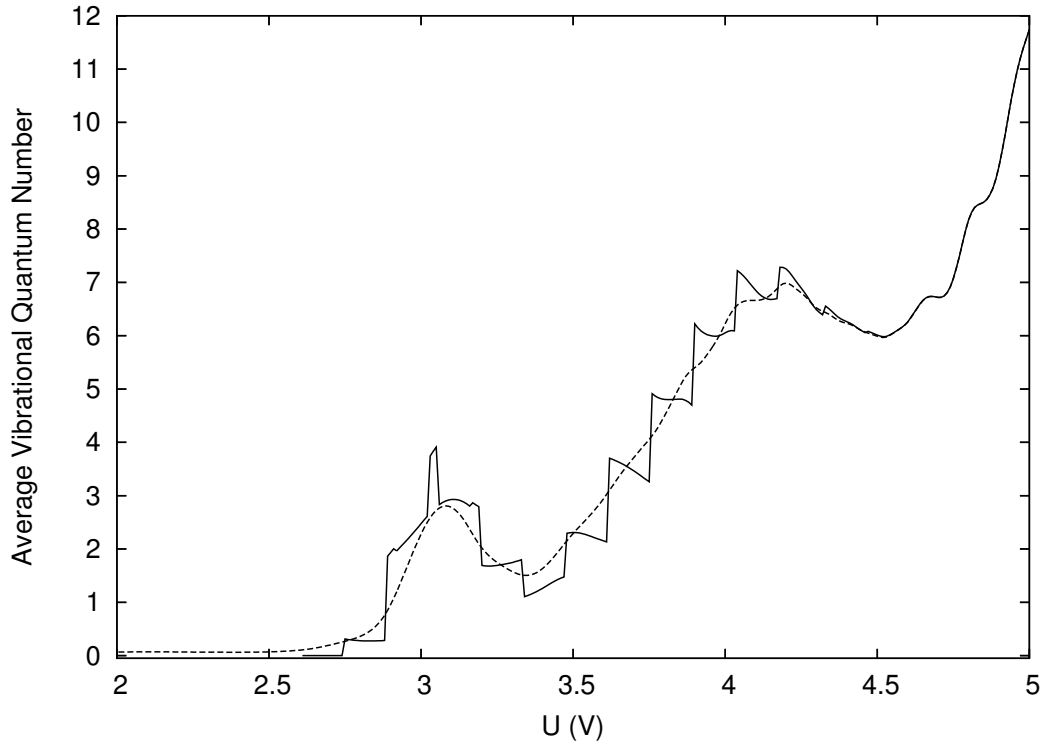

Figure 5.5: The average number of vibrational quanta as a function of voltage for T=0 K (solid line) and room temperature (dashed line) of the normal mode with frequency 566.12 cm^{-1}.

3.02 V and the step down at 3.05 V are no longer separated and the maximum shrinks to a value of 2.82. At 4.56 V the T=0 K and the room temperature - curve coincide and rise, indicating that there are further vibrational excitations, which no longer depend on temperature.

Fig. 5.6 shows the occupation probabilities of the electronic many-particle states, when normal mode (a) is included in the calculation. It is seen that up to 2.74 V both orbital A and B are occupied (red curve) and all other electronic states have probability zero. At 2.74 V the transition to state B comes into resonance and the probability of the doubly occupied state drops to 47%, while the occupation probability ρ_{BB} (blue curve) rises to 53%. The red and blue curve both exhibit steps at 2.88 and 3.02 V due to absorption of vibrational quanta. The probability ρ_{gg} decreases, while ρ_{BB} increases, which is to be expected, as the opening of a new vibrational channel connected to orbital B by hole transport, should increase the probability that

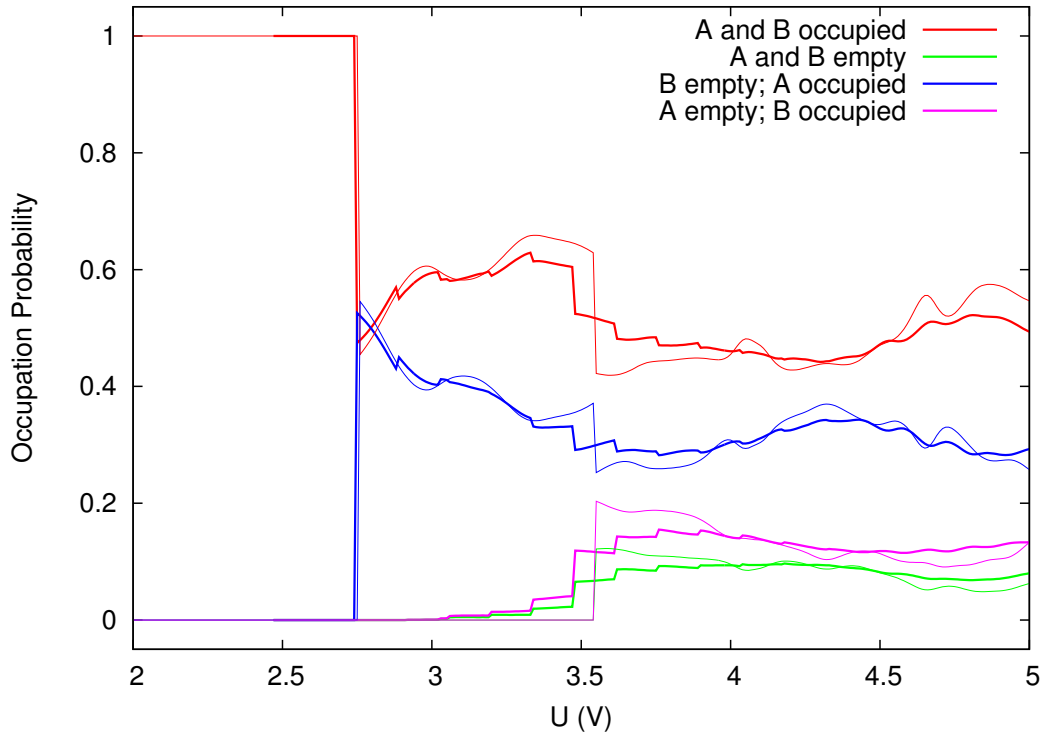

Figure 5.6: Occupation probability of the electronic states (as indicated in the legend) as a function of voltage shown for T=0 K. Results based on a vibronic calculation (bold lines) and a purely electronic calculation (thin lines) including mode (a).

this orbital is not occupied. At 3.05 V hole transport through orbital A begins to contribute and the probabilities ρ_{AA} (magenta curve) and ρ_{00} (green curve) rise in steps of $2\hbar\omega/e = 0.14\,V$, while the probabilities of the other two states decrease. At 3.47 V the transitions $\rho^{\nu\nu}_{AA} \leftarrow \rho^{\nu\nu}_{gg}$ come into resonance causing a somewhat larger step, and additional steps due to excitation of vibrational quanta follow. The electronic occupation probabilities for the vibronically interacting system closely follow that of the purely electronic system. The main difference is the second step at 3.47 V, which in the vibronic case occurs at slightly lower voltage, due to the reorganization energy. In the vibronic calculation this step is additionally divided into several sub-steps.

Fig. 5.7 shows the non-equilibrium vibrational distribution as a function of voltage and vibrational quantum number in a contour plot. At low voltages only the vibrational ground state is occupied, as expected at T=0 K. At

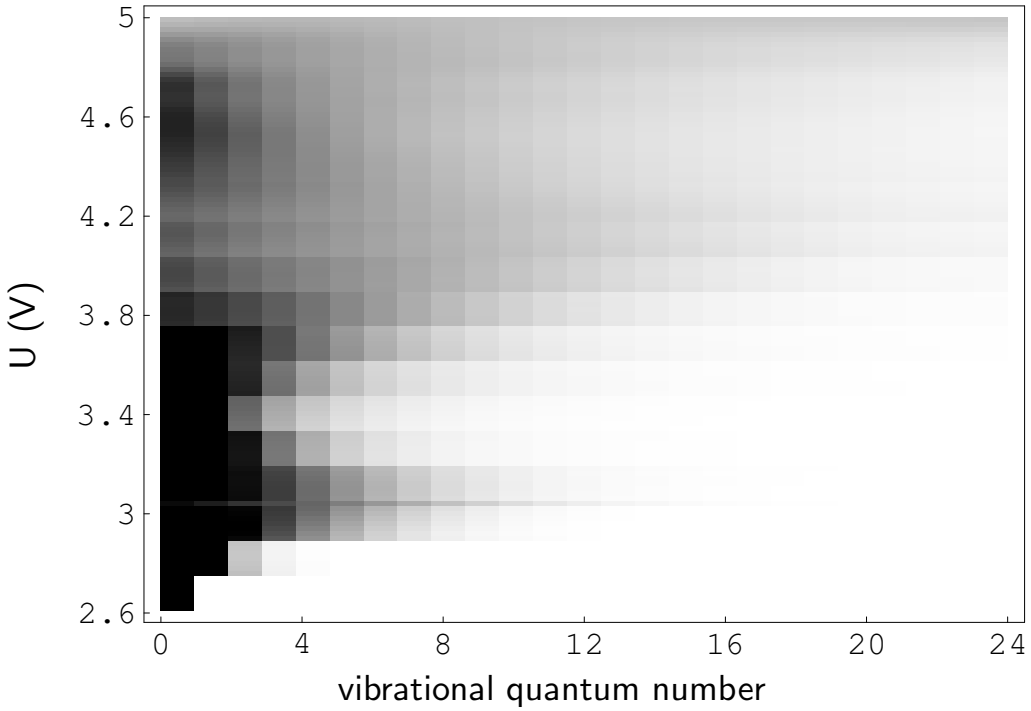

Figure 5.7: The vibrational populations of the normal mode with frequency 566.12 cm^{-1} at T=0 K. Large values are colored black while small values are colored white.

higher voltages the distribution becomes broader, but the vibrational ground state retains the maximum probability. Between 3.8 and 5.0 V also rather large quantum numbers have non-vanishing probability and the distribution strongly deviates from the equilibrium distribution. The distribution changes in steps corresponding to twice the vibrational frequency (0.14 V).

5.2.4 Effect of the C-C stretching mode

Next, we consider the influence of vibrational mode (d) (cf. Fig. 4.17) on the conductance of the electronic two level system. Fig. 5.8 shows the I-V characteristic for the system coupled to mode (d) (cf. Tab. 4.4). Due to the larger reorganization energy, with respect to the reorganization energy due to mode (a), the transition to the vibrational ground state of orbital B already comes into resonance at 2.61 V and is followed by single and double vibrational excitations causing steps at 3.03 and 3.44 V. This last step is followed immediately by the $\rho^{\nu\nu}_{AA} \leftarrow \rho^{\nu\nu}_{gg}$ transitions at 3.46 V, which are

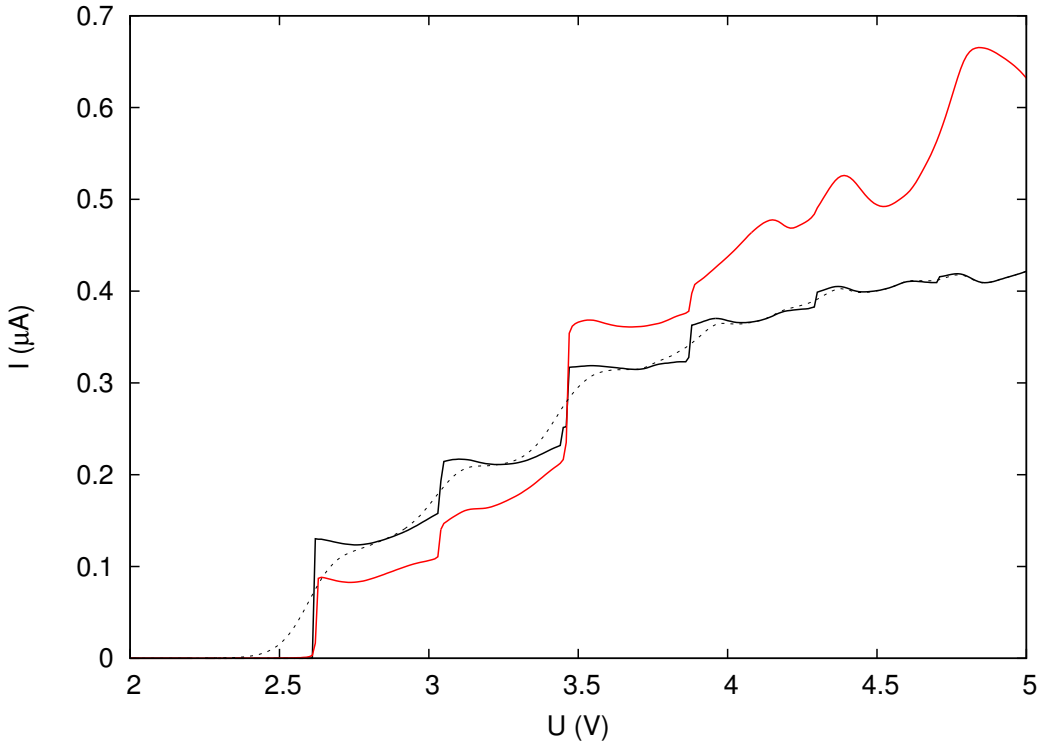

Figure 5.8: Current through states A and B of BDBT coupled to the mode with frequency $\omega = 1676.10\,\mathrm{cm}^{-1}$ using the density matrix approach at T=0 K (solid line) and at room temperature (dashed line), and using scattering theory at T=0 K.

shifted by an amount of -0.08 V with respect to the corresponding transitions in the purely electronic curve. Steps causing vibrational excitation occur at 3.87, 4.29, and 4.70 V, and the step distance corresponds to twice the vibrational frequency, $2\hbar\omega/e = 0.42\,V$.

The red curve in Fig. 5.8 shows the current based on a scattering calculation, which exhibits a step at 2.61 V due to the resonance with state B and another step at 3.03 V due to excitation of vibrational quanta. The current from the scattering calculation is smaller than that from density matrix theory up to the step at 3.46 V, which is due to state A, and becomes larger afterwards. At 3.87 V there is another step due to excitation of vibrational quanta, and unlike in the density matrix curve, no further steps are seen.

We next consider the average vibrational quantum number, $\langle a^\dagger a \rangle$, shown in Fig. 5.9. The steps in this curve closely follow those in the I-V character-

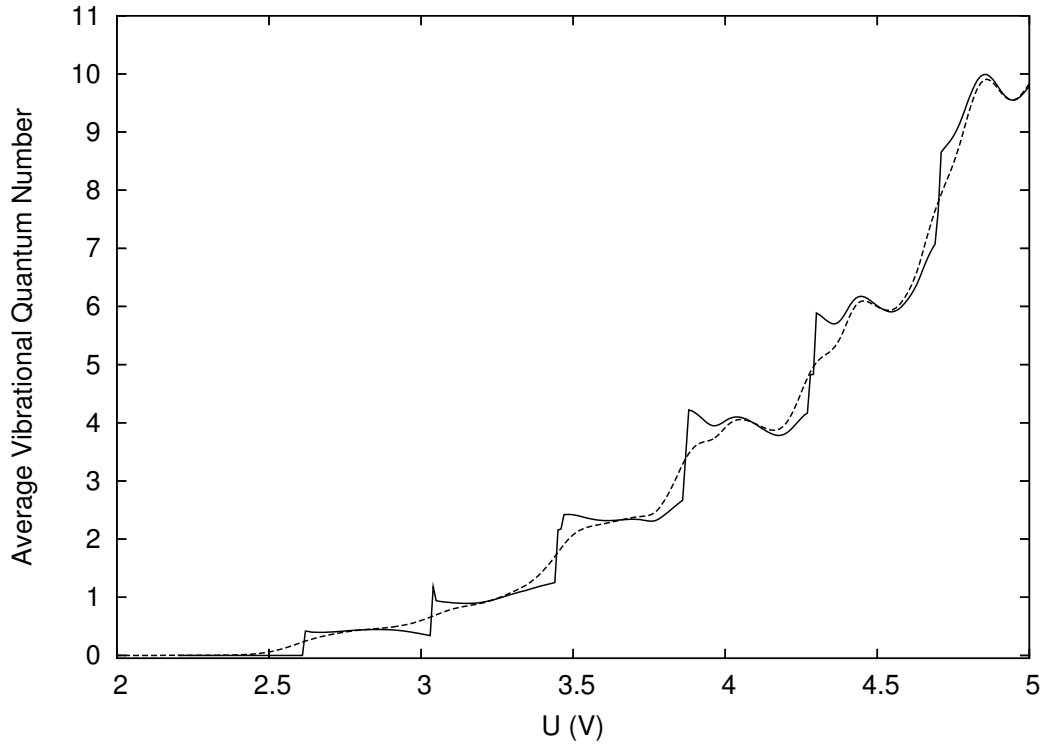

Figure 5.9: The average number of vibrational quanta as a function of voltage for T=0 K (solid line) and room temperature (dashed line) of the normal mode with frequency 1676.10 cm^{-1}.

istics. The first three steps at 2.61, 3.03, and 3.44 V are due to orbital B. The step at 3.44 V is immediately followed by the first step due to orbital A at 3.46 V, which is rather large as it is connected to the $\rho^{\nu\nu}_{AA} \leftarrow \rho^{\nu\nu}_{gg}$ transitions. Three further steps follow at 3.87, 4.29, and 4.70 V until a global maximum of 10 is reached after the last step. As the distance between individual vibrational states for this mode is much larger than for mode (a) (cf. Fig. 5.5) transitions coupled by small Franck-Condon factors occur at much higher voltages and the region where those transitions are rather small are not reached in the shown voltage window. Unlike the average vibrational quantum number for mode (a), that of mode (d) shows no decrease due to absorption of vibrational quanta. This is due to the fact that the ratio between the orbital energy difference and the vibrational frequency is much smaller for mode (d).

Fig. 5.10 shows the occupation probabilities of the electronic many-particle

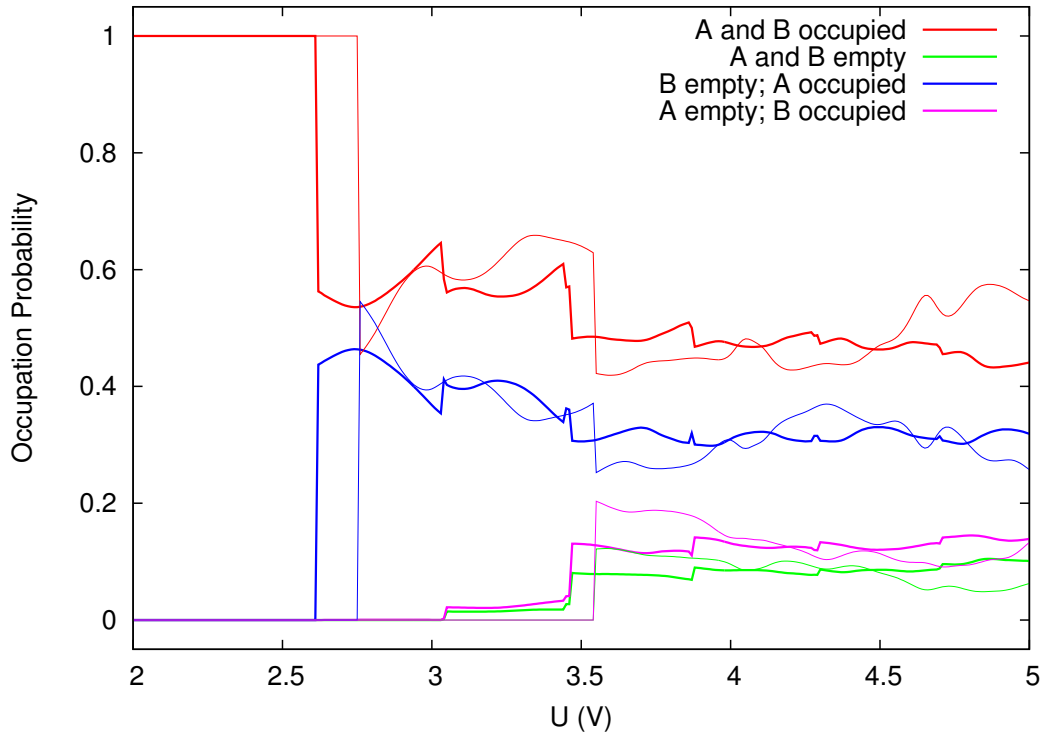

Figure 5.10: Occupation probability of the electronic states (as indicated in the legend) as a function of voltage shown for T=0 K. Results based on a vibronic calculation (bold lines) and a purely electronic calculation (thin lines) including mode (d).

states summed over diagonal vibrational elements, $\rho_{\Psi\Psi}$, when normal mode (d) is included in the calculation. We see that up to the step at 2.61 V both orbital A and B are occupied (red curve) and all other electronic states have probability zero. The occupation probability ρ_{gg} then drops to 56%, while the probability of state ρ_{AA} jumps up to 46%. Both probabilities display steps at 3.03 and 3.44 V. Interestingly, at 3.04 V the probabilities ρ_{BB} and ρ_{00} begin to rise, which must be due to absorption of vibrational quanta that could not be seen in the I-V characteristic or the average vibrational quantum number, but may explain the sharp tip in the solid curve of Fig. 5.9 at 3.04 V. The double step structure at 3.44 and 3.46 V, which describes transport through orbital B including vibrational excitation immediately followed by transport through orbital A without vibrational excitation, exists in all four solid curves. The blue curve shows this behavior also at larger voltages,

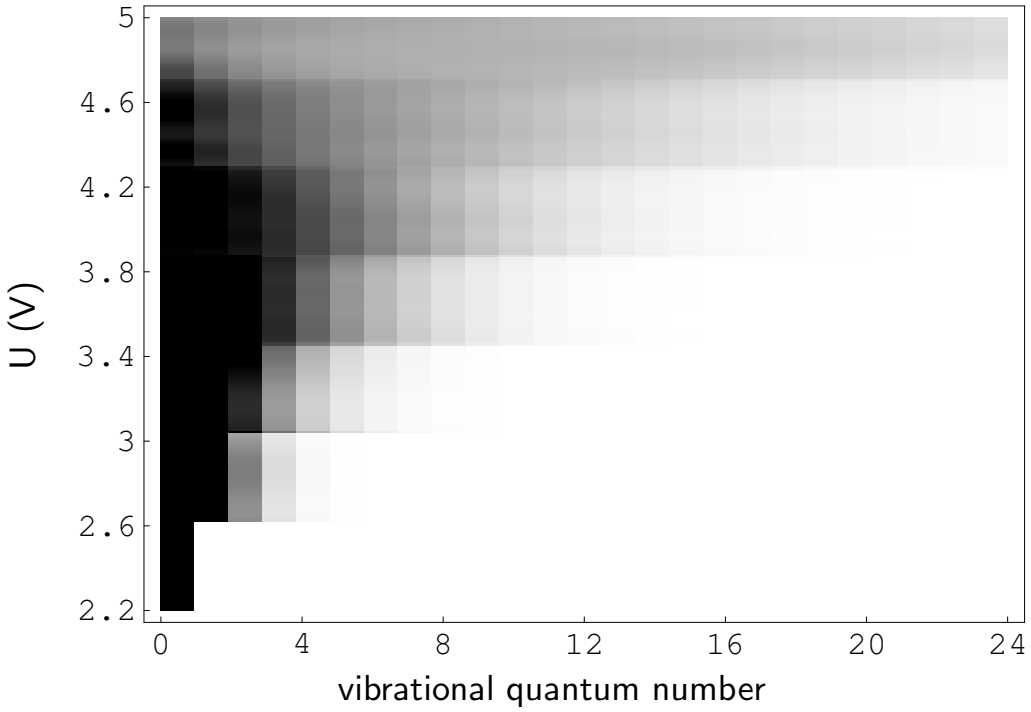

Figure 5.11: The voltage-dependent probabilities of the vibrational populations of the normal mode with frequency 1676.10 cm^{-1} at T=0 K. Large values are colored black while small values are colored white.

i.e. at 3.87, 4.29, and 4.70 V, where a step up due to the opening of a new vibrational channel in orbital B is immediately followed by the opening of a new channel in orbital A, which decreases the probability ρ_{BB} and results in tip-like features. The probability of state ρ_{AA} (magenta line) shows inverted tips at the same positions, while the probability of the doubly unoccupied state shows simple steps as both new channels in orbital A and B increase its probability. Compared to the purely electronic calculation, the shifts due to the reorganization energy are clearly seen for both orbitals. The first step is noticeably smaller in the vibronic calculation, than without vibrations, and the second step is subdivided into several steps.

In Fig. 5.11 the probability distribution of the individual vibrational states with quantum number ν_l are shown as a function of voltage. The steps at a distance of $2\hbar\omega/e = 0.42\,V$ are clearly visible. Between 2.2 and 2.6 V only the vibrational ground state is occupied. As expected, the non-equilibrium distribution becomes broader with increasing voltage.

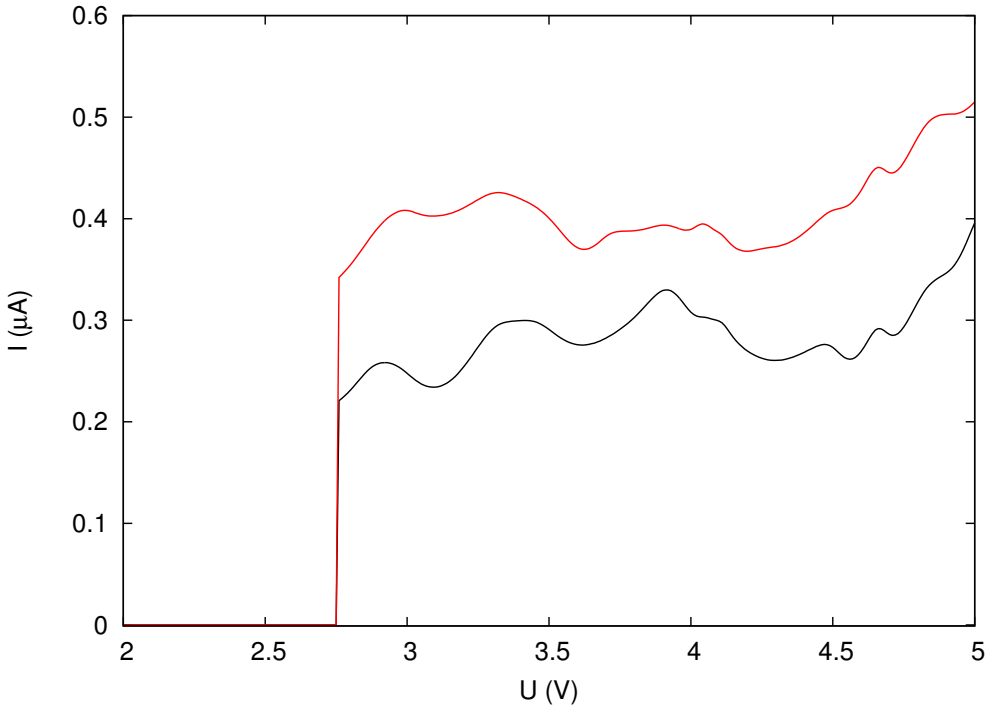

Figure 5.12: The purely electronic current for the two orbitals A and B, whose level-spacing was reduced to 0.001 eV. The current including electronic coherences (black line) and excluding them (red line) is shown.

5.2.5 Coherences

In the computation of the curves in the last sections all vibrational and electronic coherences were taken into consideration. The results show, however, that for this system electronic and vibrational coherences are so small that a calculation neglecting all off-diagonal components of the density matrix yields a similar result. This is due to the significant difference of the electronic energies E_j.

The role of electronic coherences can be artificially enhanced by decreasing the electronic level spacing. Fig. 5.12 shows the purely electronic current-voltage curve for the two level system, where the actual level spacing of 0.396 eV was reduced to 0.001 eV. It can be seen that the two steps visible in Fig. 5.2 merged into one step and that the current that was calculated including electronic coherences is significantly smaller, than the current without coherences.

On the other side, the effect of vibrational coherences in our studies could not be increased by tuning the electronic level-spacing to an integer multiple

of the vibrational frequency. The vibrational coherences are of size $\sim 10^{-5}$ and below.

5.3 Summary

In this chapter, the transport characteristics of a molecular junction were investigated based on the solution of the equation of motion of the density operator. The equation of motion was derived for the density operator reduced onto the molecular part of the system, the Markov approximation was invoked, and the steady-state limit was taken.

There are two major differences between the density matrix and scattering theory formalisms as they were used in this work. First, the density matrix treatment involves perturbation theory in the electronic coupling between electrode and molecule, while scattering theory includes this interaction to infinite order. Secondly, using the density matrix, vibrational non-equilibrium effects are included, while in the scattering formalism we assume that after each scattering process the vibrational equilibrium distribution is established.

We presented results for charge transport through a molecular junction modeled by an electronic two level system that was coupled to two different vibrational modes. In the data based on purely electronic calculations two steps, due to the two included molecular orbitals, could be seen. When including vibrational coupling these features were subdivided into several steps, the height of which was determined by the respective Franck-Condon factors and whose level spacing corresponded to twice the vibrational frequency.

For the mode with the lower frequency, absorption of vibrational quanta was visible, as the electronic level spacing was much larger than the vibrational frequency. Thus, a vibrational population could be created by vibronic excitations due to the first electronic state, which in turn was depopulated by vibronic transitions of the second electronic state. Features due to absorption of vibrational quanta were pronounced at zero Kelvin and smoothened out at room temperature.

Overall, the density matrix and scattering treatment yielded similar results. This means, that for the studied model system the electronic states were coupled weakly enough for perturbation theory to hold and the electronic resonances were far enough from the Fermi level for the multi-channel scattering formalism to work. The resonance steps in the results obtained with a density matrix calculation display sharp edges, while those obtained with scattering theory are broadened. Also the step heights differ slightly, while the step positions are equal.

In the employed model systems, vibronic transitions in which the vibrational quantum number does not change, posses the largest probabilities and effects like Franck-Condon blockade [83, 84] do not play a role.

To conclude this chapter, we discuss related work. Using rate-equations it was found that the non-equilibrium vibrational distribution becomes broader with decreasing electron-phonon coupling [80, 85]. Transport studies employing density matrices need not necessarily be done considering only the density matrix reduced to the molecular DOF. In the literature schemes were presented, where the populations of the total MMM system were considered [86, 87], which led to a nonlinear system of rate-equations. Furthermore, the density matrix formalism is often employed in the study of Coulomb interactions between several electrons on the molecule, and it was seen that the cotunneling transition rates depend on the sequential processes via the charge that can by located on the molecule by the latter [86]. In Ref. [88] the authors studied a system where the potential energy surface of the charged state was not only shifted with respect to that of the neutral state, but also distorted. This means that different frequencies were assumed in the neutral and the ionized states, and it was found that non-equilibrium vibrational effects, like NDR, are enhanced in this case. Density matrix approaches are also used in the study of laser driven molecular junctions [75, 89].

Chapter 6

Optical Switches

In this chapter, we will consider the possibility to optically switch molecular junctions between different conductance states. In contrast to the other parts of this thesis, this aspect of molecular junctions is not directly related to vibronic coupling and therefore all results presented will be based on purely electronic transport calculations.

A molecular junction can be used as an electronic switch, if the molecule exists in two or more differently conducting states that can be reversibly transferred into each other. Possible switching mechanisms are based on charge transfer reactions or optical excitations, which cause an intramolecular reaction or a conformational change of the molecule.

A photochemical switch was investigated experimentally using a self-assembled monolayer in a break-junction [90]. In solution, the studied molecule switched from the highly conducting to the non-conducting form by irradiation with light in the visible range, while it switched into the other direction by irradiation with UV-light. In the junction only the switching from high to low conductance could be observed and the absence of the reverse switching process was attributed to the strong electronic interactions of the molecules with the gold electrodes.

Stochastic switching and switching induced by the application of pulses of large voltage were observed experimentally [91] for phenylene ethynylene oligomers incorporated in alkanethiolate monolayers in STM. It was found that the different conducting states correspond to different conformations of the molecule. Application of large voltages again switched the molecules from the high to the low conducting state, but not in the other direction.

Theoretically, switching behavior was demonstrated in molecular junctions including dithienylethene molecules [92]. Here, the switching mechanism is due to photon absorption, which triggers an intramolecular ring closing or opening reaction. Upon this reaction the energetic positions of the

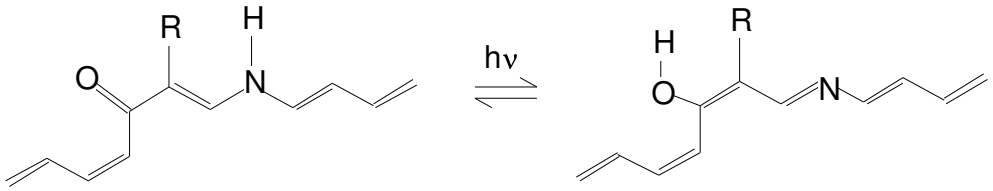

Figure 6.1: Scheme of the optically induced hydrogen transfer reaction between a hydroxy-imine and a keto-amine. R stands either for H in the pure molecules, or for some hydrogen-carrier group.

HOMO and the LUMO are exchanged. Using scattering theory it could be demonstrated, that the conductance of the 'closed' isomer is up to 100 times larger than the conductance of the 'open' isomer. A photochemical molecular switch based on an azobenzene molecule between two carbon nanotubes was investigated in Ref. [93]. In this system the switching mechanism relies on a cis/trans isomerization.

In the example presented in this chapter, the switching mechanism is due to an optically induced hydrogen transfer reaction. The structural formula of the system under study is depicted in Fig. 6.1. Two planar tautomers, 3-hydroxy-2,4,6-heptatrien-7-thiolate - butadien-4-thiolate - imine and 3-oxo-1,4,7-heptatrien-7-thiolate - butadien-4-thiolate - amine (for R=H), are connected via a photochemically induced hydrogen transfer reaction. For similar systems, this reaction was predicted to be reversible [94] and can be tuned in either direction by irradiating the sample with light of different frequencies. As the nitrogen and oxygen atoms are quite far apart, it is expected, that hydrogen transfer cannot take place for the pure molecule (R=H), but that a flexible hydrogen-carrier group is needed.

As can be seen in Fig. 6.1, the hydroxy-imine form possess one more double-bond in the carbon-nitrogen chain than does the keto-amine form. This difference in π-electron density on the chain could lead to different transport properties when clamping the molecule between two electrodes and applying a voltage. In the following, the transport characteristics of the pure molecules and with two different carrier groups bonded to a gold cluster of 38 gold atoms on each side will be shown and discussed. Fig. 6.2 shows a cartoon of the pure (R=H) hydroxy-imine and keto-amine molecules between two gold clusters.

A geometry optimization was done for the molecules bonded to two gold atoms at the B3-LYP-SV(P) level using symmetry group C_s. The remaining gold atoms were added referring to distances and angles known from earlier calculations and a single point calculation was done for the whole system.

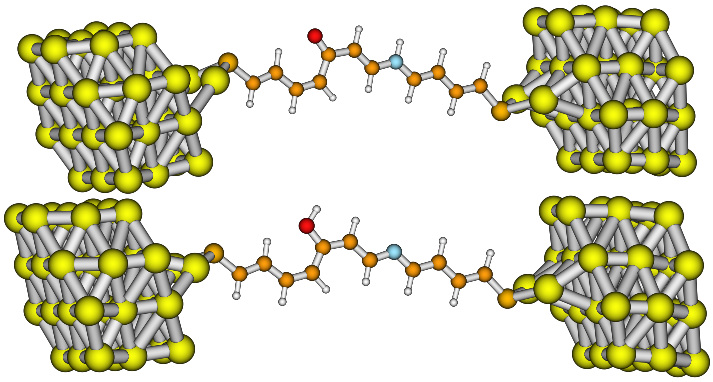

Figure 6.2: Partially optimized structures of 3-hydroxy-2,4,6-heptatrien-7-thiolate - butadien-4-thiolate - imine (bottom) and 3-oxo-1,4,7-heptatrien-7-thiolate - butadien-4-thiolate - amine (top) bonded to gold clusters containing 38 atoms.

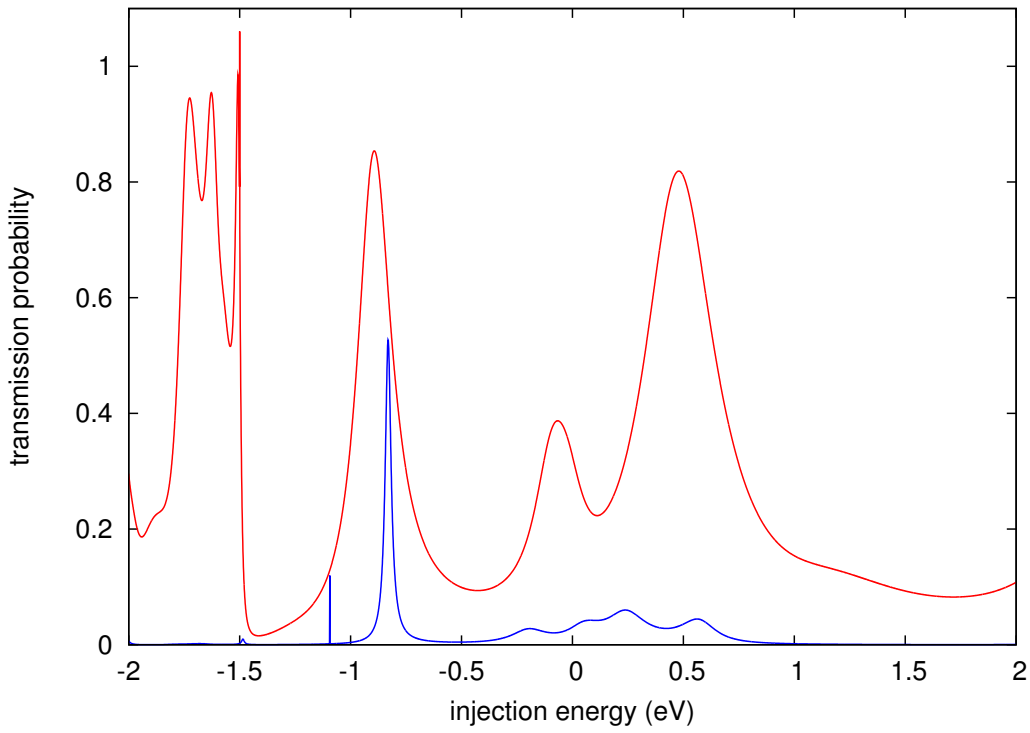

Figure 6.3: Zero-voltage transmission probability through the hydroxy-imine (red curve) and the keto-amine form (blue curve) of the pure molecules (Fig. 6.2).

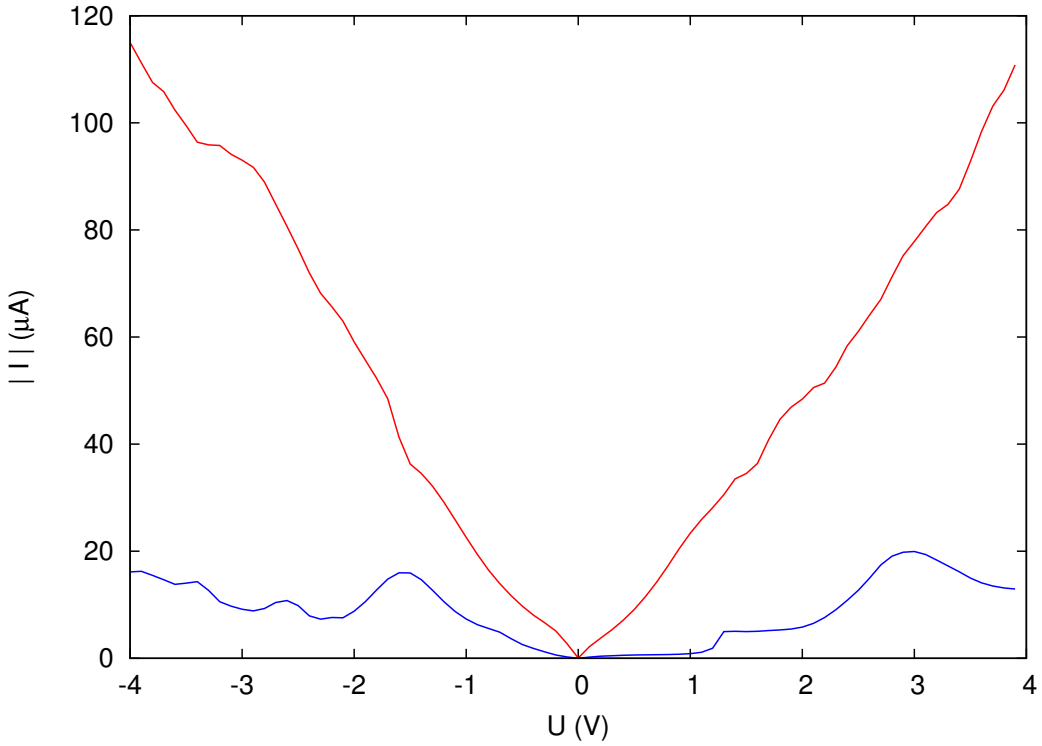

Figure 6.4: The modulus of the current through the hydroxy-imine (red curve) and the keto-amine form (blue curve) of the pure molecules.

The value of the Fermi energy was taken from the literature as that of bulk gold (ϵ_f = -5.53 eV). All electronic states of the molecular space were included in the transmission and current calculations.

The transmission probabilities of the pure molecules are shown in Fig. 6.3. The hydroxy-imine form (red curve) has a much larger transmission probability at the Fermi energy and throughout the whole studied energy range and shows large, broad peaks at 0.48, -0.07, -0.89, -1.63, and -1.73 eV and a small peak at -1.50 eV, while in the corresponding curve for the keto-amine form (blue curve) there are small broad peaks in the region between -0.5 and +1.0 eV with a maximum probability of 6 % and two narrow peaks at -0.83 and -1.09 eV, respectively.

As the molecules are not symmetric with respect to the left and right contact, the current in Fig. 6.4 is shown in the positive as well as in the negative voltage range, where the current in the latter was mirrored at the abscissa for compactness. Although the coupling to the left and right lead is

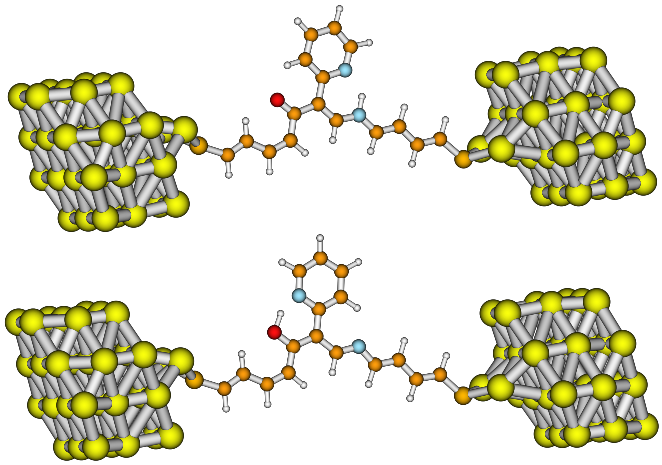

Figure 6.5: Partially optimized structures of the keto-amine (top) and hydroxy-imine (bottom) forms, when including a pyridine-ring as the hydrogen-transferring unit, bonded to gold clusters containing 38 atoms.

no longer symmetric it is expected to be of comparable size and therefore the voltage division factor of 0.5 is retained. It is clearly seen, that the current for the hydroxy-imine form (red curve) is much larger than the current for the keto-amine form (blue curve) over the whole voltage range. Taking the values at $\pm 1\,\mathrm{V}$, a value that can realistically be reached by experiments, the ratio of the two current values in the negative voltage range is approx. 3:1, while that in the positive voltage range is even larger, approx. 26:1. Thus, for the pure molecules our theoretical treatment predicts switching behavior. Additionally we note that the keto-amine form has a rectification coefficient of $I(-1\,V)/I(+1\,V) \approx 8$.

In the next step, a pyridine-ring was added to the pure molecules (R=C_5H_4N) (Fig. 6.5). This ring is supposed to act as a hydrogen transferring unit by binding the hydrogen atom of the amine-group to the nitrogen in the pyridine-ring, performing a 180°-rotation around the C-C-bond that connects the pyridine to the molecular chain, and releasing the hydrogen-atom to the oxygen.

The geometry was optimized for the molecules with the sulfur still bonded to hydrogen. After this, the hydrogen was removed, the gold cluster was added, and a single point DFT calculation was done.

The transmission functions, shown in Fig. 6.6, for the hydroxy-imine (red curve) and keto-amine forms (blue curve), with the additional pyridine group, differ significantly from those of the pure molecules. The transmission of the hydroxy-imine form shows several broad and large overlapping peaks with

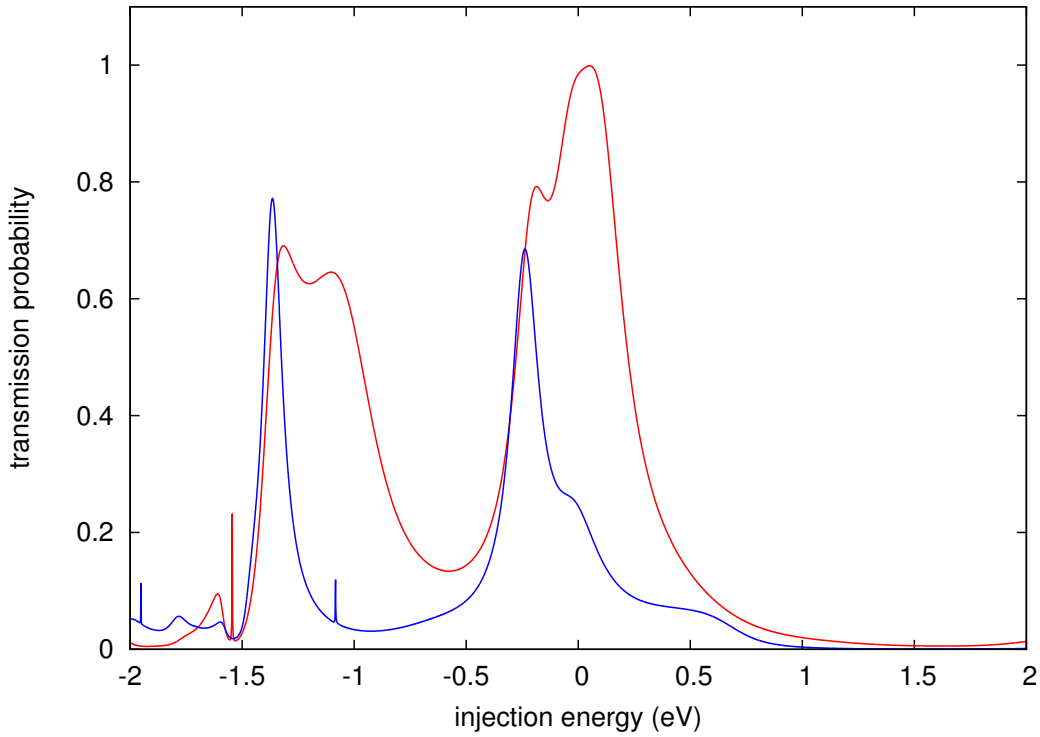

Figure 6.6: The zero-voltage transmission probability through the hydroxy-imine (red curve) and the keto-amine form (blue curve), with a pyridine - hydrogen-carrying group.

maxima at 0.05, -0.19, -1.10, and -1.31 eV, and some smaller features at -1.54 (narrow line) and -1.61 eV. In the transmission function of the keto-amine form, on the other hand, there is a peak of probability 0.69 at -0.24 eV which has two shoulders at -0.02 and 0.57 eV. The small narrow peak at -1.08 eV, that could already be seen in the pure molecule, also appears in this system. There is another large peak at -1.36 eV. Overall, the transmission probability for the hydroxy-imine system is still larger than for the keto-amine system, but the difference is not as pronounced as in the pure molecules.

The I-V characteristic of the molecules with the pyridine-carrier-group depicted in Fig. 6.7 shows that the current of the hydroxy-imine system (red curve) is larger than that of the keto-amine form (blue curve) in the whole voltage range. However, when analyzing the ratios between the currents of the two forms at ± 1 V, we find that in the positive voltage range this ratio is approx. 1.6:1 and that in the negative voltage range it is approx. 2:1. These

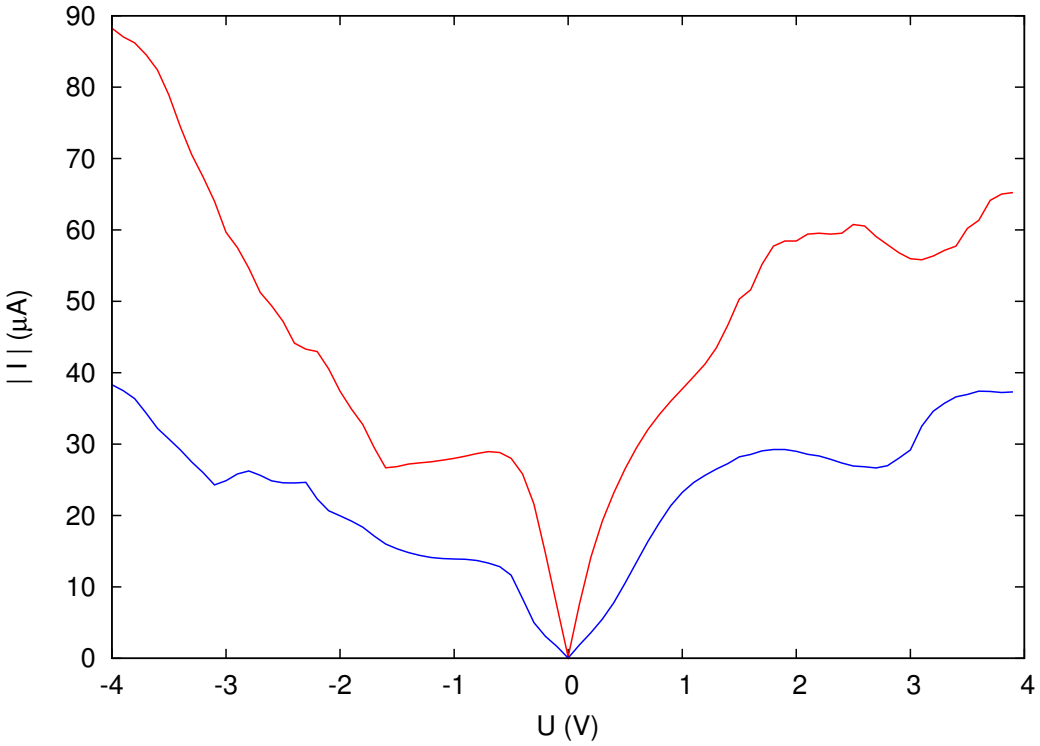

Figure 6.7: The modulus of the current through the hydroxy-imine (red curve) and the keto-amine form (blue curve) with a pyridine-ring as hydrogen-transferring unit.

ratios are significantly smaller than that of the pure molecules. The absolute current values at $\pm 1\,\mathrm{V}$, however, are larger than before, even if the current at large voltages, $\pm 4\,\mathrm{V}$, is smaller.

A more efficient hydrogen transferring unit, in the sense that the activation barrier for the photo-chemical hydrogen transfer reaction is lowered considerably, is the imino-lactone-ring, R=$C_4H_2NO_2$, shown in Fig. 6.8. To characterize the electronic structure, the geometry was optimized for the molecules with the sulfur still bonded to hydrogen. After this, the hydrogen atoms were removed, the gold cluster was added, and a single point DFT calculation was done.

The transmission function of the molecules with the imino-lactone group, depicted in Fig. 6.9, only shows single peaks. The peak is of medium size and broad for the keto-amine form (blue curve), where it is positioned at 0.66 eV, has probability 0.46 and FWHM 0.14 eV, while it is narrow and large for

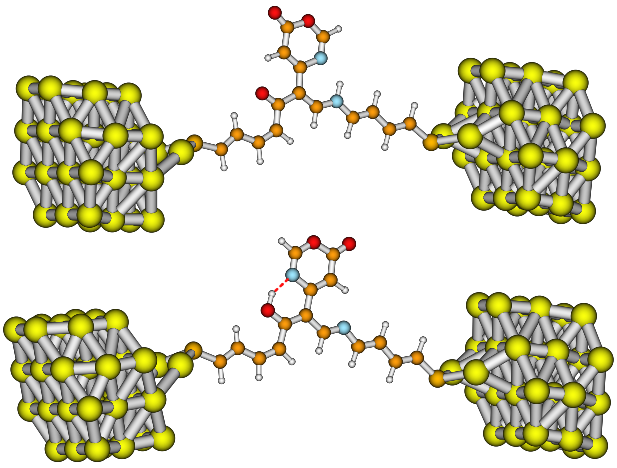

Figure 6.8: Partially optimized structures of the keto-amine (top) and hydroxy-imine (bottom) forms, when including an imino-lactone-ring as the hydrogen-transferring unit, bonded to gold clusters containing 38 atoms.

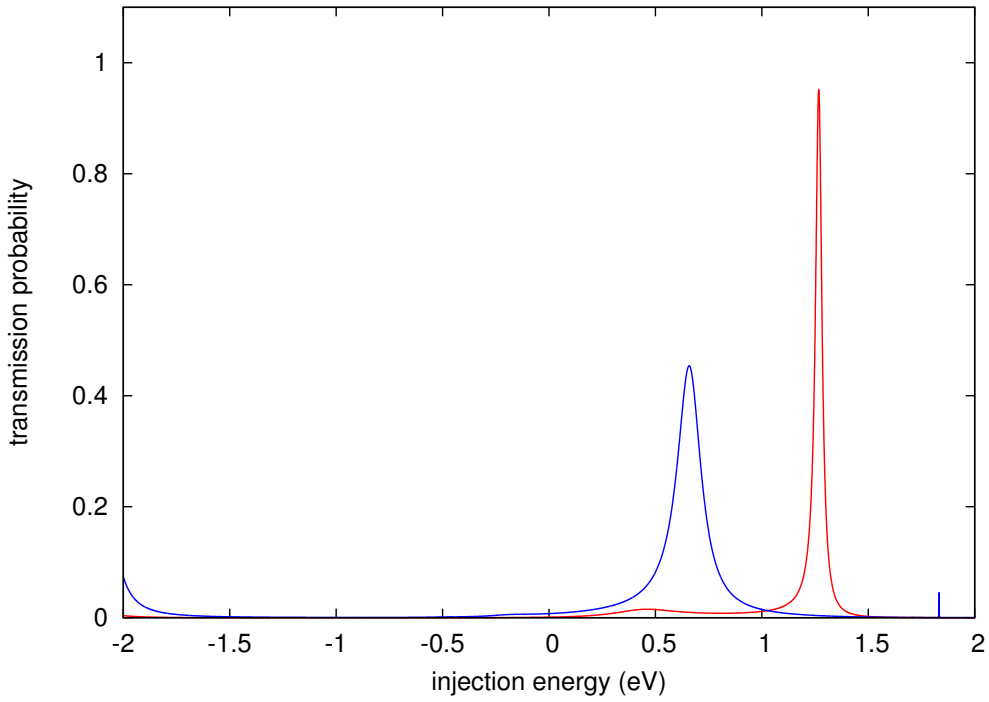

Figure 6.9: The zero-voltage transmission probability through the hydroxy-imine (red curve) and the keto-amine form (blue curve), with an imino-lactone - hydrogen-carrying group.

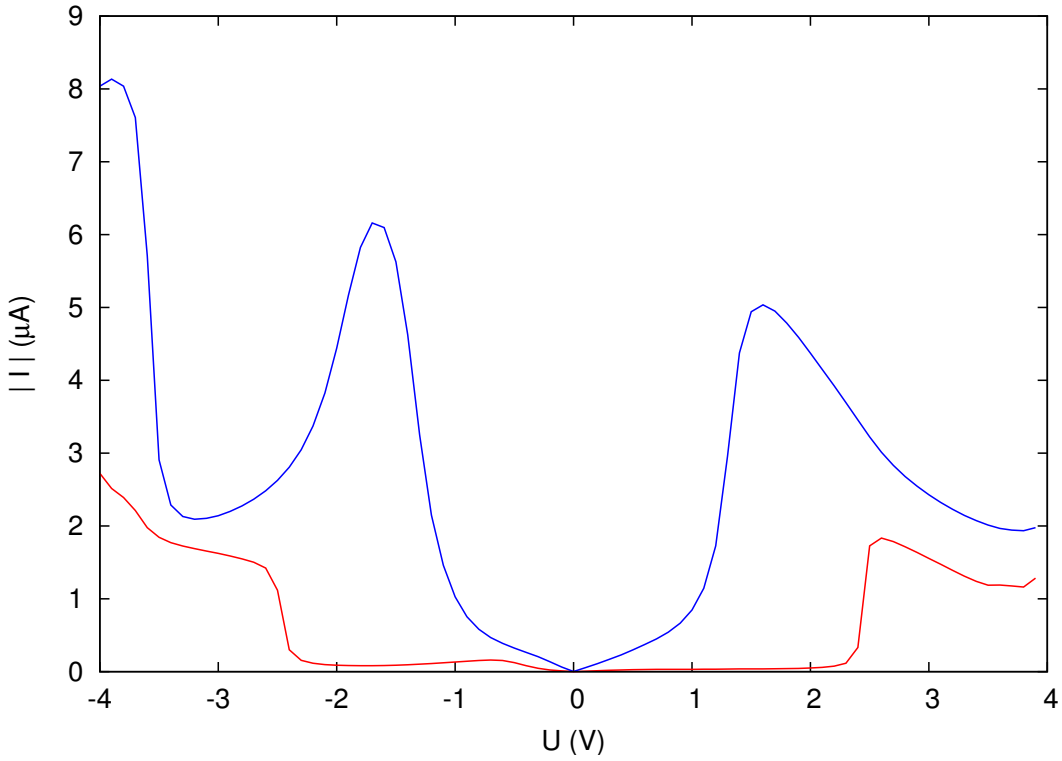

Figure 6.10: The modulus of the current through the hydroxy-imine (red curve) and the keto-amine form (blue curve) with an imino-lactone as hydrogen-transferring unit.

the hydroxy-imine form (red curve), where it is located at 1.27 eV, has a probability of 95% and FWHM 0.04 eV. This means that, if the transmission function is not altered fundamentally at larger voltages, the peak due to the keto-amine form would enter the voltage window long before that due to the other form.

The current curve, shown in Fig. 6.10, confirms what could be expected from the transmission probability. The situation is reversed with respect to the pure molecules and the molecules containing the pyridine-ring in such a way that now the current for the keto-amine system is larger in the whole voltage range. The ratio at ± 1 V in the positive range is 1:26, while that in the negative range is 1:8. This means, that the molecule could still be used as a switch, but in the other direction than we assumed initially. The overall current, however, is smaller by about a factor of ten. Furthermore, the current for the keto-amine system (blue curve) shows much more pronounced

NDR features, than in the systems described above. These NDR effects are again due to the voltage-dependence of the electrode self-energy.

To summarize, the hydrogen-transferring unit significantly influences possible switching behavior by changing the molecular electronic structure of the orbitals around the Fermi level. The current decreases when going from the pure molecules via the pyridine to the imino-lactone carrier group. The reason is, that molecular orbitals around the Fermi energy become less delocalized over the whole molecular backbone, the more electronegative the transferring unit. This mechanism influences the keto-amine and the hydroxy-imine form differently.

Chapter 7

Summary

In this thesis we have investigated the conductance of molecular junctions, in which a single molecule is bound to two metallic electrodes. We focused on the consequences of nuclear motion of the molecule on the transport characteristics of the junction and investigated the switching behavior of tautomeric molecules.

To study vibrationally coupled electron transport in single molecule junctions, we used a model Hamiltonian, whose parameters were determined by ab initio electronic structure calculations. Based on Koopmans' theorem, the Hamiltonian describes the two cases that only molecular orbitals sufficiently above (electron transport) or below (hole transport) the Fermi level contribute to conductance. To determine the parameters of the Hamiltonian, the overall molecular junction was separated into three parts, a part comprising the molecule and parts of the electrodes and the remaining part of the left and right electrode. The former was described by density functional theory while the latter was accounted for by a single parameter or a tight-binding model self-energy. The quantum-chemically described part was further divided into the molecule and the left and right contacts, respectively, using projection operator techniques.

We used two different theoretical methods to calculate transport properties through molecular junctions. The first theoretical transport method employed in this work is inelastic scattering theory, the central quantity of which is the multi-channel transmission probability. The current in scattering theory is given by the energy integral of this transmission probability weighted by occupation factors. The second theoretical method that was discussed in this thesis is density matrix theory. The current in density matrix theory is given in terms of the populations and coherences of the vibrational and electronic molecular states, which are obtained by the solution of a linear system of rate equations.

There are several differences between the scattering and the density matrix approach: At first, while scattering theory considers the electronic coupling between molecular orbitals and electrode states up to infinite order, in the density matrix calculations this interaction was only included in second order. This restricts the applicability of density matrix theory to weak molecule-electrode coupling. Secondly, in scattering theory we assume that after each scattering process the system relaxes to the vibrational equilibrium, whereas we do not include any vibrational relaxation in the density matrix formalism. In the latter formalism the non-equilibrium distributions caused by vibronic excitations is computed directly, which enables the absorption of vibrational quanta. In scattering theory at zero temperature, only the excitation of vibrational quanta can be observed. Thirdly, while the current expression in the density matrix treatment was derived from the general definition of the current, the current expression involving the multi-channel scattering probability was derived following probabilistic arguments and has not been derived strictly, so far. Fourthly, in the density matrix approach we have to deal with electronic many-particle states, whereas we can reduce our treatment to single particle states in the scattering formalism. This allows to include significantly more molecular orbitals in the computation.

Scattering theory was applied to two classes of molecules. The first class consists of a benzene ring that was separated from the gold contacts by different thiolate-linker groups, the second class consisted of pairs of tautomers, that acted as photochemical switches. In the benzene-thiolate systems we demonstrated the importance of respective time/energy scales, comprising the lifetime of the hole on the molecule, the size of the vibronic coupling, and the vibrational frequency, which determine the influence of vibrational effects. In all systems we observed negative differential resistance effects, which we could attribute to the voltage dependence of the eigenenergies of the gold contacts. In the tautomeric molecules, on the other hand, we studied the different transport characteristics of the two tautomers and thus possible switching behavior. The results depended significantly on the chemical nature of the hydrogen carrying unit.

Density matrix theory was used to compute the current-voltage curve of a 'two electronic states'-'one mode' system, which we compared to similar results obtained from scattering theory. Qualitatively, the results from both theories agreed very well except for features due to absorption of vibrational quanta which could only be obtained by the density matrix formalism.

Finally it is noted that although the field of molecular electronics has developed rapidly in the last decades, it is difficult to predict whether it is ever going to be of technological relevance. Nevertheless, it is a fascinating topic that involves interesting research and yields valuable insights into quantum mechanical transport processes on the molecular scale.

Appendix A

Surface Self-energy

The infinite, periodic part of the molecular junction is accounted for by a surface self-energy (Σ^{sf}), which is supposed to describe the effect on the contacts due to their coupling to a semi-infinite metal solid.

The Green's function of the whole molecular junction is defined as

$$G(E) = \lim_{\eta \to 0^+} \left[(E + i\,\eta)\mathbf{1} - H \right]^{-1} = \left[E^+ - H \right]^{-1} \ ,$$

where $\mathbf{1}$ is the unit-operator, H is the Hamiltonian of the total system, and η is a positive infinitesimal.

As the transport characteristics will mainly be determined by the extended molecule, we are interested in the Green's function projected onto the Hilbert space spanned by the extended molecule,

$$G^{\mathrm{ext}} = P_\chi G P_\chi \ ,$$

where $P_\chi = \sum_i |\chi_i\rangle\langle\chi_i|$, with $|\chi_i\rangle$ being orthogonal states in the extended molecular space.

Using the Lippmann-Schwinger equation [50]

$$G = G_0 + G_0 V G \quad ,$$

where G_0 is the Green's function related to the Hamiltonian without molecule-lead coupling, we obtain

$$G^{\mathrm{ext}} = P_\chi G P_\chi = P_\chi G_0 P_\chi + P_\chi G_0 V G P_\chi \quad .$$

The sum of projection operators, $P_\chi + Q_L^{\mathrm{sf}} + Q_R^{\mathrm{sf}} = 1$, is inserted on both sides of the operator V, where Q_L^{sf} and Q_R^{sf} are the projection operators onto the

left and right semi-infinite solid spaces, respectively. It can be shown that only three terms remain

$$G^{\text{ext}} = P_\chi G P_\chi = P_\chi G_0 P_\chi + P_\chi G_0 P_\chi V Q_L^{\text{sf}} G P_\chi + P_\chi G_0 P_\chi V Q_R^{\text{sf}} G P_\chi \quad . \text{(A.1)}$$

The terms $Q_L^{\text{sf}} G P_\chi$ and $Q_R^{\text{sf}} G P_\chi$ can again be evaluated using the Lippmann-Schwinger equation, and inserting $1 = P_\chi + Q_L^{\text{sf}} + Q_R^{\text{sf}}$. This leads to

$$Q_L^{\text{sf}} G P_\chi = Q_L^{\text{sf}} G_0 Q_L^{\text{sf}} V P_\chi G P_\chi \quad ,$$

and a similar expression for $Q_R^{\text{sf}} G P_\chi$. Inserting this equation into Eq. (A.1) gives

$$\begin{aligned} G^{\text{ext}} &= P_\chi G_0 P_\chi + P_\chi G_0 P_\chi V Q_L^{\text{sf}} G_0 Q_L^{\text{sf}} V P_\chi G P_\chi + P_\chi G_0 P_\chi V Q_R^{\text{sf}} G_0 Q_R^{\text{sf}} V P_\chi G P_\chi \\ &= P_\chi G_0 P_\chi + P_\chi G_0 P_\chi \Sigma_L^{\text{sf}} P_\chi G P_\chi + P_\chi G_0 P_\chi \Sigma_R^{\text{sf}} P_\chi G P_\chi \\ &= P_\chi G_0 P_\chi + P_\chi G_0 P_\chi \Sigma_L^{\text{sf}} G^{\text{ext}} + P_\chi G_0 P_\chi \Sigma_R^{\text{sf}} G^{\text{ext}} \end{aligned} \quad \text{(A.2)}$$

where the idempotency of P_χ and the definition of the retarded self-energy $\Sigma_L^{\text{sf}} = P_\chi V Q_L^{\text{sf}} G_0 Q_L^{\text{sf}} V P_\chi$, and similarly of Σ_R^{sf}, was used.

Eq. (A.2) can be rearranged,

$$G^{\text{ext}} = \left[E^+ - P_\chi G_0 P_\chi \Sigma_L^{\text{sf}} - P_\chi G_0 P_\chi \Sigma_R^{\text{sf}}\right]^{-1} P_\chi G_0 P_\chi \quad .$$

Using the operator relation $A^{-1}B = [B^{-1}A]^{-1}$ we obtain

$$\begin{aligned} G^{\text{ext}} &= \left[(P_\chi G_0 P_\chi)^{-1} \left(E^+ - P_\chi G_0 P_\chi \Sigma_L^{\text{sf}} - P_\chi G_0 P_\chi \Sigma_R^{\text{sf}}\right)\right]^{-1} \\ &= \left[(P_\chi G_0 P_\chi)^{-1} - \Sigma_L^{\text{sf}} - \Sigma_R^{\text{sf}}\right]^{-1} \\ &= \left[E^+ - P_\chi H P_\chi - \Sigma_L^{\text{sf}} - \Sigma_R^{\text{sf}}\right]^{-1} \quad . \end{aligned}$$

The Green's function projected onto the extended molecular space thus contains the Hamiltonian of the extended molecule $P_\chi H P_\chi = \tilde{h}$ and the self-energy of the left and right metal surfaces $\Sigma^{\text{sf}} = \Sigma_L^{\text{sf}} + \Sigma_R^{\text{sf}}$,

$$G^{\text{ext}} = \left[E^+ - \left(\tilde{h} + \Sigma^{\text{sf}}\right)\right]^{-1} \quad .$$

This explains the usage of $h^{\text{sf}} = \tilde{h} + \Sigma^{\text{sf}}$ in Eq. (3.11).

The Hamiltonian matrix h^{sf} can be arranged in block structure,

$$h^{\text{sf}} = \begin{pmatrix} h_L^{\text{sf}} & h_{LM}^{\text{sf}} & h_{LR}^{\text{sf}} \\ h_{ML}^{\text{sf}} & h_M^{\text{sf}} & h_{MR}^{\text{sf}} \\ h_{RL}^{\text{sf}} & h_{RM}^{\text{sf}} & h_R^{\text{sf}} \end{pmatrix} \quad .$$

While $h_M^{\rm sf}$ is a real symmetric matrix, $h_L^{\rm sf}$ and $h_R^{\rm sf}$ are complex symmetric matrices.

Next, $h^{\rm sf}$ is block diagonalized,

$$h^{\rm u} = U^T h^{\rm sf} U = \begin{pmatrix} E^L & V^{LM} & V^{LR} \\ V^{ML} & E^M & V^{MR} \\ V^{RL} & V^{RM} & E^R \end{pmatrix}, \; U = \begin{pmatrix} U_L & 0 & 0 \\ 0 & U_M & 0 \\ 0 & 0 & U_R \end{pmatrix}.$$

The eigenvectors of the blocks belonging to L and R form a bi-orthogonal basis in the left and right lead space, respectively. This means that the column vectors of U_L constitute the right eigenvectors of $h_L^{\rm sf}$, $\mathbf{u}_k$, while the row vector of U_L^T constitute the left eigenvectors of $h_L^{\rm sf}$, $\mathbf{u}_{k'}^T$. The left eigenvectors are the transposed (not the Hermitian conjugate) of the right eigenvectors and vice versa. The inner product of left and right eigenvectors is given by $\mathbf{u}_{k'}^T \cdot \mathbf{u}_k = \delta_{kk'} S_k^{\rm u}$, where $S_k^{\rm u}$ is an overlap element, that, in general, is complex and not equal to unity. The eigenvalues, $\mathbf{u}_{k'}^T h_L^{\rm sf} \mathbf{u}_k = \delta_{kk'} E_k$, of a non-Hermitian matrix are complex as well.

In order to avoid complications that would arise if bi-orthogonality was considered in the derivation of the transport equations in sections 4.1 and 5.1, we will derive these transport equations assuming a general, orthogonal basis of continuum states in the leads and approximate these states by the bi-orthogonal ones of the finite contact space, $|\phi_k\rangle \rightarrow \mathbf{u}_k$, in the final transport equations.

The projection operator $\sum_k |\phi_k\rangle\langle\phi_k|$ in Eq. (4.19) acts on an arbitrary state $|\phi_l\rangle$ like

$$\sum_k |\phi_k\rangle\langle\phi_k|\phi_l\rangle = |\phi_k\rangle\delta_{kl} \; .$$

In the orthogonal basis set, a projection operator that gives an equivalent result is given by

$$\sum_k \frac{\mathbf{u}_k \cdot \mathbf{u}_k^T}{S_k^{\rm u}} \mathbf{u}_l = \sum_k \frac{\mathbf{u}_k \cdot S_k^{\rm u}}{S_k^{\rm u}} \delta_{kl} = \mathbf{u}_k \tag{A.3}$$

This gives the following expression for the lead self-energy.

$$\begin{aligned}
\Sigma_L^{\rm lead}(E)_{ij} &= \sum_{k,k'\in L} \langle\phi_i|V|\phi_k\rangle\langle\phi_k|\frac{1}{(E^+ - H_L)}|\phi_{k'}\rangle\langle\phi_{k'}|V|\phi_j\rangle \ , \\
&\Rightarrow \sum_{k,k'\in L} \langle\phi_i|V\frac{\mathbf{u}_k\cdot\mathbf{u}_k^T}{S_k^{\rm u}}\frac{1}{(E^+ - H_L)}\frac{\mathbf{u}_{k'}\cdot\mathbf{u}_{k'}^T}{S_{k'}^{\rm u}}V|\phi_j\rangle \ , \\
&= \sum_{k,k'\in L} V_{ik'}\frac{1}{S_k^{\rm u}}\frac{S_k^{\rm u}\delta_{kk'}}{(E^+ - E_{k'})}\frac{1}{S_{k'}^{\rm u}}V_{k'j} \ , \\
&= \sum_{k\in L} V_{ik}\frac{1}{S_k^{\rm u}(E^+ - E_{k'})}V_{kj} \ .
\end{aligned}$$

Note that in a complex symmetric matrix, in general, $V_{ik} \neq V_{ki}^*$ but $V_{ik} = V_{ki}$.

Bibliography

[1] A. Aviram, M. A. Ratner, *Chem. Phys. Lett.* **29**, 277 (1974).

[2] A. Nitzan, *Annu. Rev. Phys. Chem.* **52**, 681 (2001).

[3] M. A. Reed, C. Zhou, C. J. Muller, T. P. Burgin, J. B. Tour, *Science* **278**, 252 (1997).

[4] J. Jortner, M. Bixon, *Electron Transfer: From Isolated Molecules to Biomolecules, Dynamics and Spectroscopy Adv. Chem. Phys. Vols. 106-107*, (Wiley, New York, 1999).

[5] F. Chen, J. Hihath, Z. Huang, X. Li, N. Tao, *Annu. Rev. Phys. Chem.* **58**, 535 (2007).

[6] B. Xu, H. He, N. J. Tao, *J. Am. Chem. Soc.* **124**, 13568 (2002).

[7] R. Landauer, *IBM J. Res. Dev.* **1**, 223 (1957).

[8] J. van Ruitenbeek, E. Scheer, H. B. Weber. in *Introducing Molecular Electronics*, G. Cuniberti, G. Fagas and and K. Richter, Eds. Springer, (2006).

[9] W. H. A. Thijssen, D. Djukic, A. F. Otte, R. H. Bremmer, J. M. van Ruitenbeek, *Phys. Rev. Lett.* **97**, 226806 (2006).

[10] D. Djukic, K. S. Thygesen, C. Untiedt, R. H. M. Smit, K. W. Jacobsen, J. M. van Ruitenbeek, *Phys. Rev. B* **71**, 161402 (2005).

[11] K. S. Thygesen, K. W. Jacobsen, *Phys. Rev. Lett.* **94**, 036807 (2005).

[12] M. Reed, C. Zhou, C. Muller, T. Burgin, J. Tour, *Science* **278**, 252 (1997).

[13] H. B. Weber, J. Reichert, F. Weigend, R. Ochs, D. Beckmann, M. Mayor, R. Ahlrichs, H. v.Löhneysen, *Chem. Phys.* **281**, 113 (2002).

[14] X. H. Qiu, G. V. Nazin, W. Ho, *Phys. Rev. Lett.* **92**, 206102 (2004).

[15] N. Ogawa, G. Mikaelian, W. Ho, *Phys. Rev. Lett.* **98**, 166103 (2007).

[16] T. Ishida, W. Mizutani, N. Choi, U. Akiba, M. Fujihira, H. Tokumoto, *J. Phys. Chem. B* **102**, 11680 (2000).

[17] G. Rubio, N. Agrait, S. Vieira, *Phys. Rev. Lett.* **76**, 2302 (1996).

[18] J. Park, A. Pasupathy, J. Goldsmith, C. Chang, Y. Yaish, J. Petta, M. Rinkoski, J. Sethna, H. Abruna, P. McEuen, D. Ralph, *Nature (London)* **417**, 722 (2002).

[19] T. Dadosh, Y. Gordin, R. Krahne, I. Khivrich, D. Mahalu, V. Frydman, J. Sperling, A. Yacobi, I. Bar-Joseph, *Nature (London)* **436**, 677 (2005).

[20] L. Yu, Z. Keane, J. Ciszek, L. Cheng, M. Stewart, J. Tour, D. Natelson, *Phys. Rev. Lett.* **93**, 266802 (2004).

[21] A. N. Pasupathy, J. Park, C. Chang, A. V. Soldatov, S. Lebedkin, R. C. Bialczak, J. E. Grose, L. A. K. Donev, J. P. Sethna, D. C. Ralph, P. L. McEuen, *Nano Lett.* **5**, 203 (2005).

[22] N. J. Tao, *Nature Nano.* **1**, 173 (2006).

[23] S. W. Wu, N. Ogawa, W. Ho, *Science* **312**, 1362 (2006).

[24] M. Galperin, M. A. Ratner, A. Nitzan, *J. Phys.: Condens. Matter* **19**, 103201 (2007).

[25] S. Datta, *Electric Transport in Mesoscopic Systems*, (Cambridge University Press, UK, 1997).

[26] M. Galperin, M. A. Ratner, A. Nitzan, *J. Chem. Phys.* **121**, 11965 (2004).

[27] M. Galperin, M. Ratner, A. Nitzan, *Phys. Rev. B* **73**, 045314 (2006).

[28] A. Pecchia, A. D. Carlo, *Nano Lett.* **4**, 2109 (2004).

[29] T. Yamamoto, K. Watanabe, S. Watanabe, *Phys. Rev. Lett.* **95**, 65501 (2005).

[30] Y. Asai, *Phys. Rev. Lett.* **93**, 246102 (2004).

[31] M. Paulsson, T. Frederiksen, M. Brandbyge, *Nano Lett.* **6**, 258 (2006).

[32] J. G. Kushmerick, J. Lazorcik, C. H. Patterson, R. Shashidhar, D. S. Seferos, G. C. Bazan, *Nano Lett.* **4**, 639 (2004).

[33] T. Frederiksen, M. Paulsson, M. Brandbyge, A. Jauho, *Phys. Rev. B* **75**, 205413 (2007).

[34] L. Mühlbacher, E. Rabani, *cond-mat.mes-hall* **arXiv:0707.0956v1** (2007).

[35] P. S. Cornaglia, H. Ness, D. R. Grempel, *Phys. Rev. Lett.* **93**, 147201 (2004).

[36] L. Cederbaum, W. Domcke, *J. Chem. Phys.* **60**, 2878 (1974).

[37] I. Kondov, M. Cizek, C. Benesch, H. Wang, M. Thoss, *J. Phys. Chem. C* **111**, 11970 (2007).

[38] P.-O. Löwdin, *Adv. Quantum Chem.* **5**, 185 (1970).

[39] T. Pacher, L. S. Cederbaum, H. Köppel. Adiabatic and quasidiabatic states in a gauge theoretical framework. in *Advances in Chemical Physics*, I. Prigogine and S. A. Rice, Eds., vol. LXXXIV. John Wiley & Sons, Inc., (1993).

[40] F. Jensen, *Introduction to Computational Chemistry*, (John Wiley & Sons, Chichester, 1999).

[41] I. N. Levine, *Quantum Chemistry*, (Prentice Hall, New Jersey 07458, 2000).

[42] P. Delaney, J. C. Greer, *Phys. Rev. Lett.* **93**, 36805 (2004).

[43] F. Evers, F. Weigend, M. Koentopp, *Phys. Rev. B* **69**, 235411 (2004).

[44] R. Ahlrichs, M. Bär, M. Häser, H. Horn, C. Kölmel, *Chem. Phys. Lett.* **162**, 165 (1989).

[45] K. Eichkorn, O. Treutler, H. Öhm, M. Häser, R. Ahlrichs, *Chem. Phys. Lett.* **240**, 283 (1995).

[46] H. Basch, M. A. Ratner, *J. Chem. Phys.* **119**, 11926 (2003).

[47] C. Herrmann, M. Reiher, *Surface Science* **600**, 1891 (2006).

[48] K. Stokbro, J. Taylor, M. Brandbyge, H. Guo. in *Introducing Molecular Electronics*, G. Cuniberti, G. Fagas and and K. Richter, Eds. Springer, (2006).

[49] M. Caspary-Toroker, U. Peskin, *J. Chem. Phys.* **127**, 154706 (2007).

[50] J. Taylor, *Scattering Theory*, (John Wiley & Sons, N.Y., 1972).

[51] X. Xiao, B. Xu, N. J. Tao, *Nano Lett.* **4**, 167 (2004).

[52] P. Derosa, J. Seminario, *J. Phys. Chem. B* **105**, 471 (2001).

[53] M. D. Ventra, S. T. Pantelides, N. D. Lang, *Phys. Rev. Lett.* **84**, 979 (2000).

[54] Y. Xue, M. Ratner, *Phys. Rev. B* **68**, 115406 (2003).

[55] Y. Xue, M. Ratner, *Phys. Rev. B* **68**, 115407 (2003).

[56] W. Tian, S. Datta, S. Hong, R. Reifenberger, J. I. Henderson, C. P. Kubiak, *J. Chem. Phys.* **109**, 2874 (1998).

[57] A. Kopf, P. Saalfrank, *Chem. Phys. Lett.* **386**, 17 (2004).

[58] A. Pecchia, A. D. Carlo, A. Gagliardi, T. A. Niehaus, T. Frauenheim, *J. Comp. Electr.* **4**, 79 (2005).

[59] J. Jiang, M. Kula, Y. Luo, *J. Chem. Phys.* **124**, 34708 (2006).

[60] Y. Chen, M. Zwolak, M. D. Ventra, *Nano Lett.* **5**, 813 (2005).

[61] R. Guitierrez, G. Fagas, K. Richter, F. Grossmann, R. Schmidt, *Europhys. Lett.* **62**, 90 (2003).

[62] A. V. de Parga, O. Hernan, R. Miranda, A. L. Yeyati, N. Mingo, A. Martin-Rodero, F. Flores, *Phys. Rev. Lett.* **80**, 357 (1998).

[63] M. Cizek, M. Thoss, W. Domcke, *Phys. Rev. B* **70**, 125406 (2004).

[64] J. Koch, F. von Oppen, *Phys. Rev. Lett.* **94**, 206804 (2005).

[65] C. Benesch, M. Cizek, M. Thoss, W. Domcke, *Chem. Phys. Lett.* **430**, 355 (2006).

[66] X. Xiao, B. Xu, N. Tao, *Nano Lett.* **4**, 267 (2004).

[67] A. Troisi, M. A. Ratner, A. Nitzan, *J. Chem. Phys.* **118**, 6072 (2003).

[68] A. Troisi, M. A. Ratner, *Phys. Rev. B* **72**, 033408 (2005).

[69] Y. Chen, M. Zwolak, M. D. Ventra, *Nano Lett.* **3(12)**, 1691 (2003).

[70] Y. Chen, M. Zwolak, M. D. Ventra, *Nano Lett.* **4(9)**, 1709 (2004).

[71] T. Seideman, *J. Phys.: Cond. Matt.* **15**, R521 (2003).

[72] R. P. Feynman, *Statistical Mechanics*, (Addison Wesley Publishing Company, U.S.A., 1972).

[73] V. May, O. Kühn, *Charge and Energy Transfer Dynamics in Molecular Systems*, (Wiley-VCH, Berlin, 2000).

[74] E. Fick, *Einführung in die Grundlagen der Quantentheorie*, (Akad. Verlagsgesell., Wiesbaden, 1979).

[75] J. Lehmann, S. Kohler, V. May, P. Hänggi, *J. Chem. Phys.* **121**, 2278 (2004).

[76] G. Schön, (Wiley-VCH, 1997), ch. Single-Electron Tunneling.

[77] E. Petrov, *Chem. Phys.* **326**, 151 (2006).

[78] V. May, *Phys. Rev. B* **66**, 245411 (2002).

[79] U. Harbola, M. Esposito, S. Mukamel, *Phys. Rev. B* **74**, 235309 (2006).

[80] A. Mitra, I. Aleiner, A. J. Millis, *Phys. Rev. B* **69**, 245302 (2004).

[81] V. May, O. Kühn, *Chem. Phys. Lett.* **420**, 192 (2006).

[82] J. Koch, F. von Oppen, *Phys. Rev. B* **72**, 113308 (2005).

[83] J. Koch, F. von Oppen, *Phys. Rev. Lett.* **94**, 206804 (2005).

[84] J. Koch, F. von Oppen, A. V. Andreev, *Phys. Rev. B* **74**, 205438 (2006).

[85] J. Koch, M. Semmelhack, F. v. Oppen, A. Nitzan, *Phys. Rev. B* **73**, 155306 (2005).

[86] E. G. Petrov, V. May, P. Hänggi, *Chem. Phys.* **319**, 380 (2005).

[87] E. G. Petrov, V. May, P. Hänggi, *Phys. Rev. B* **73**, 045408 (2006).

[88] M. Wegewijs, K. Nowack, *New J. Phys.* **7**, 239 (2005).

[89] P. Hänggi, S. Kohler, J. Lehmann, M. Strass. in *Introducing Molecular Electronics*, G. Cuniberti, G. Fagas and and K. Richter, Eds. Springer, (2006).

[90] D. Dulic, S. van der Molen, T. Kudernac, H. Jonkman, J. de Jong, T. Bowden, J. van Esch, B. Feringa, B. van Wees, *Phys. Rev. Lett.* **91**, 207402 (2003).

[91] Z. Donhauser, B. Mantooth, K. Kelly, L. Bumm, J. Monnell, J. Stapleton, D. Price, A. Rawlett, D. Allara, J. Tour, P. Weiss, *Science* **292**, 2303 (2001).

[92] J. Li, G. Speyer, O. Sankey, *Phys. Rev. Lett.* **93**, 248302 (2004).

[93] V. M. del R. Gutierrez, C. Tejedor, G. Cuniberti, *Nature Nanotech.* **2**, 176 (2007).

[94] A. Sobolewski, submitted.